8-17-2017

Dielectric and Electrothermal Properties of Ferroelectric Multilayers and Superlattice Heterostructures

Mehmet Kesim
University of Connecticut - Storrs, mehmet.kesim@uconn.edu

Dielectric and Electrothermal Properties of Ferroelectric Multilayers and Superlattice Heterostructures

Mehmet Tumerkan Kesim

University of Connecticut, 2017

Artificial ferroelectric (FE) heterostructures show unique electrical properties compared to bulk and single-crystal and thin film FEs. The internal built-in electrical fields due to heterogenoeuos nature of the structure gives rise to unique electrical properties. Dielectric and electrothermal (pyroelectric and electrocaloric) properties of such multilayers and superlattice (SL) heterostructures are investigated using a non-linear thermodynamic model. The underlying reasons for the enhancement of electrical properties of FE heterostructures are analyzed based on the strain and built-in electrostatic fields that could be used as design parameters under realistic processing conditions of such materials. It is shown that the choice of multilayer/substrate pair, processing/growth temperature, and relative layer fraction of ferroelectric could be tailored to enhance dielectric and electrothermal properties of FE multilayers. For instance, large tunabilities (90% at 400 kV/cm) are possible in carefully designed barium strontium titanate-strontium titanate (STO) and lead zirconate titanate (PZT)-STO even on silicon for which there exist substantially large in-plane strains. It is also possible to obtain enhanced electrocaloric response from multilayers. 0.75·barium titanate-0.25·PZT and 0.35·STO-0.65·PZT bilayers show ~120% and 65% increase in electrocaloric response, respectively, compared to PZT films on Si for ΔE=500 kV cm^{-1}. It is possible to obtain enhanced dielectric and pyroelectric response from PZT-STO SLs, especially with increased number of repeating unit for a fixed thickness. It is possible to avoid domain splitting in the FE and obtain enhanced properties with reduced overall transition temperature. For example, small bias pyroelectric coefficient of 8-unit symmetrical SLs is ~55% higher than that of a zero bias PZT monolayer reaching 0.045 μC cm^{-2} K^{-1}.

Dielectric and Electrothermal Properties of Ferroelectric Multilayers and Superlattice Heterostructures

Mehmet Tumerkan Kesim

M.Sc., Middle East Technical University, 2012

B.Sc., Anadolu University, 2009

A Dissertation

Submitted in Partial Fulfillment of the

Requirements for the Degree of

Doctor of Philosophy

at the

University of Connecticut

2017

APPROVAL PAGE

Doctor of Philosophy Dissertation

Dielectric and Electrothermal Properties of Ferroelectric Multilayers and Superlattice Heterostructures

Presented by

Mehmet Tumerkan Kesim, M.Sc.

Major Advisor_____

Dr. S. Pamir Alpay

Associate Advisor_____

Dr. Avinash M. Dongare

Associate Advisor_____

Dr. Serge M. Nakhmanson

Associate Advisor_____

Dr. Mark Aindow

Associate Advisor_____

Dr. Seok–Woo Lee

University of Connecticut

2017

ACKNOWLEDGEMENTS

First and foremost, I would like to thank Dr. S. Pamir Alpay for his support and guidance throughout my thesis project. I also would like to thank Dr. Mark Aindow for his supervision in our industrial project with GE. I would appreciate the help and efforts of the advisory committee members Dr. Serge M. Nakhmanson, Dr. Avinash M. Dongareö Dr. Puxian Gao and Seok–Woo Lee. I also would like to thank to the members of our lab and office and people I worked with; Dr. Jialan Zhang, Haibo Yu, Dr. Yu Sun, Yomery Espinal, John Mangeri, Dr. Sanjeev K. Nayak, Dr. Hamidreza Khassaf, Tulsi Patel, Dr. Fu–Chang Sun, Dr. Sanjubala Sahoo, Nasser Khakpash, Thomas Reid, Denis Trujillo, Kevin Co, Dr. Liang Dong, Dr. Ching–Chang Chung, and Dr. Richard Perez–Moyet, for their help and kindness Finally, I would like to thank my parents and my girlfriend for their patience and support during my whole life.

TABLE OF CONTENTS

LIST OF FIGURES

LIST OF TABLES

LIST OF ABBREVIATIONS

Abbreviation	***Full Form***
DE	Dielectric
FE	Ferroelectric
PE	Paraelectric
IC	Integrated circuit
TEC	Thermal expansion coefficient
EC	Electrocaloric effect
STO	Strontium titanate, $SrTiO_3$
BTO	Barium titanate, $BaTiO_3$
PZT	Lead zirconate, $PbZrTiO_3$
IR	Infrared
CTE	Coefficient of thermal expansion
T_C	Phase transition (Curie) temperature
T_G	Growth or processing temperature
p	Pyroelectric coefficient
ε_R	Relative dielectric permittivity
P_S	Spontaneous polarization
$<P>$	Average polarization
RT	Room temperature
α_C	Critical layer fraction
ECM	Electrocaloric materials
ΔT	Adiabatic temperature change
FPA	Focal plane array
BST	Barium strontium titanate, $Ba_xSr_{1-x}TiO_3$
MOSD	Metal-organic solution deposition
MOCVD	Metal-organic chemical vapor deposition
IC	Integrated circuitry

CHAPTER I: INTRODUCTION

1.1 Phase Transitions

A substance can be in a solid, liquid, vapor or plasma state for a given condition. There can be critical points in such states and/or passing through such states where the physical properties of the system changes abruptly. The critical point is a region determined by control field variables such as temperature, pressure, magnetic and electrical field. A phase transition is said to occur when these variables triggers a change in a physical property; for instance, density, volume and composition.[1] The emergence of new properties that are absent in the parent phase such as ferroelectricity and superconductivity is also possible. The underlying reason for the phase transition is the change in structural (atomic, molecular, etc.) and electronic (electrons, spins, phonons, etc.) states of the system by the control field variables.[2] We can describe the physical changes occurring during a phase transition with an order parameter. From a practical standpoint, order parameters can be experimentally measured and allow us to track down the phase transition.[3–5] It should be emphasized that a phase transition can have more than one order parameter that can be coupled.[6] Some examples of phase transitions and associated order parameters are shown in Table 1. Molecular tilts, magnetic moment, changes in density and composition can be identified as order parameters. An order parameter, as the name implies, represent the order of the phase and it is, in most cases, zero and one, respectively in the parent and child phase. From a structural symmetry perspective, the parent phase undergoes a transition associated with a loss of symmetry and appearance of a physical quantity.

Table 1. Examples of order parameters and corresponding type of phase transitions.[2,7]

Phase(s)	Phase Transition	Order Parameter
Liquid-gas	Condensation/Evaporation	Density
Binary mixture	Unmixing	Composition/Concentration
Nematic liquid	Orientational ordering	Q-tensor
Solids	Ferromagnetic	Magnetization
	Antiferromagnetic	Sublattice magnetization
	Ferroelectric	Polarization
	Antiferroelectric	Sublattice polarization
Solids/liquids	Superconductivity	Electron pair amplitude

1.2 Thermodynamic Properties and Property Coupling

Thermodynamic properties of materials can be defined using proper thermodynamic potentials. Some interesting physical properties arise when material properties are coupled together. The cross-coupling of material properties are quite useful in technological applications and can be visualized using a Heckmann Diagram. One example of such diagrams from ferroelectrics (FEs) point of view is shown in Figure 1. The coupling of material properties can be shown thermodynamically starting with the differential form of Gibbs Energy:

$$dG = -SdT - \varepsilon_{ij} d\sigma_{ij} - D_i dE_i \tag{1}$$

From here, the relations after taking the first derivatives are given via:

$$S = -\left(\frac{\partial G}{\partial T}\right)_{\sigma,E}, \qquad D_i = -\left(\frac{\partial G}{\partial E_i}\right)_{T,\sigma}, \qquad \varepsilon_{ij} = -\left(\frac{\partial G}{\partial \sigma_{ij}}\right)_{T,E} \tag{2}$$

Second derivatives of the Gibbs Energy yield physical constants. By changing the order of differentiation, it is possible to obtain reverse mechanical, thermal and electrical effects through:

$$\frac{C^{\sigma,E}}{T} = -\left(\frac{\partial^2 G}{\partial T^2}\right)_{\sigma,E} = \left(\frac{\partial S}{\partial T}\right)_{\sigma,E}, \tag{3}$$

$$\varepsilon_{n,m}^{\sigma,T} = -\left(\frac{\partial^2 G}{\partial E_n E_m}\right)_{\sigma,T} = \left(\frac{\partial D_n}{\partial E_m}\right)_{\sigma,T}, \tag{4}$$

$$s_{ijkl}^{E,T} = -\left(\frac{\partial^2 G}{\partial \sigma_{ij}\sigma_{kl}}\right)_{E,T} = \left(\frac{\partial \varepsilon_{ij}}{\partial \sigma_{kl}}\right)_{E,T}, \tag{5}$$

$$d_{nij}^{T} = -\left(\frac{\partial^2 G}{\partial \sigma_{ij}\partial E_n}\right)_{T} = \left(\frac{\partial D_n}{\partial \sigma_{ij}}\right)_{E,T} = \left(\frac{\partial \varepsilon_{ij}}{\partial E_n}\right)_{\sigma,T}, \tag{6}$$

$$p_n^{\sigma} = -\left(\frac{\partial^2 G}{\partial T \partial E_n}\right)_{\sigma} = \left(\frac{\partial D_n}{\partial T}\right)_{\sigma,E} = \left(\frac{\partial S}{\partial E_n}\right)_{\sigma,T} \tag{7}$$

C=heat capacity, ε_{nm}=dielectric permittivity, s_{ijkl}=elastic compliance, d_{nij}=direct and inverse piezoelectric effect, p_n=pyroelectric and electrocaloric (EC) effect.

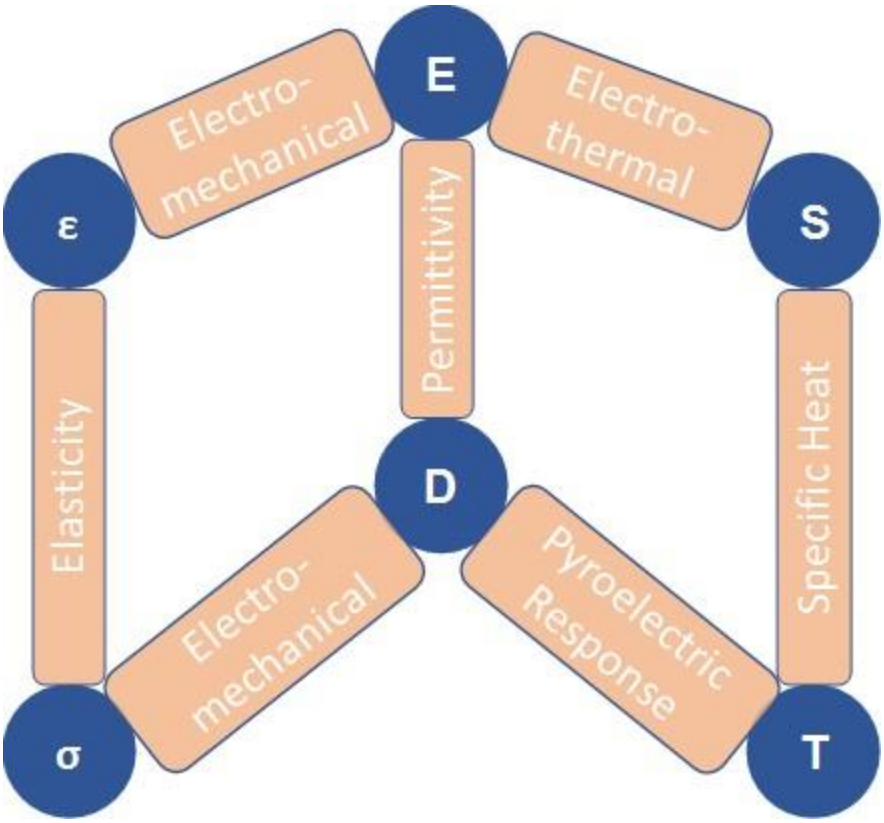

Figure 1. Coupling of material properties relevant to FEs.

1.3 Ferroelectricity

1.3.1 Ferroelectric Phenomena

FEs possess a spontaneous electrical polarization which can be reversed via an external electric field. Relative displacements of ions in a FE lattice results in a net dipole moment even without an applied field. Unlike ordinary dielectrics (DEs), polarization response of FEs under an applied electric field is non-linear and show hysteretic behavior. Domain switching and kinetics during application of a reverse bias field are responsible for the hysteresis. FEs exhibit either first or a second order phase transition.[8,9] Free energy profiles at various temperature ranges and polarization as a function of temperature for both types of phase transitions are shown in Figure 2. For a second order transition shown in Figure 2(a), polarization decreases smoothly when the

temperature is increased in the FE state until the phase transition temperature where transition takes place continuously. From the free energy profile given in Figure 2(a), two equivalent stable polarization states disappear and FE transforms into PE state above the transition temperature. On the other hand, for a first order phase transition, polarization disappears abruptly/discontinuously at the critical point which is different than the phase transition temperature.[10] The critical temperature depends whether the material is cooled or heated. Unlike second order transitions, metastable states exist with the FE phase between transition temperature and critical point. This can also be seen from the energy profile [Figure 2(c)] of a first order phase transition where local minima appears at temperatures equal or higher than the Curie temperature (T_C).[11]

Non-linear behavior of FEs and their switchable polarization has been widely exploited in capacitors, phase shifters, and filters where they are used as non-volatile memories and voltage-controlled frequency-agile elements.[12–14] What makes FEs even more attractive is they also exhibit pyroelectric and piezoelectric properties. Owing to these additional functionalities, they can also be employed as components in actuators, resonators, oscillators, intrusion and smoldering fire detectors, uncooled thermal imagers, radiometers, gas/laser analyzers, solid state cooling devices, and energy harvesting units.[15–18] Thin film FEs offer significant advantages in terms of mass-producibility, integration with other microelectronic devices, and lower processing costs compared to bulk or single crystal FEs. It has been shown that the phase transition characteristics of FE films, and thus the accompanying electrical properties, could be influenced and tailored by thermal[19] and misfit[20] strains, lateral clamping of the film to the substrate[21], domain structure[22], film/substrate texture[23], and thickness[24], and defects.[25]

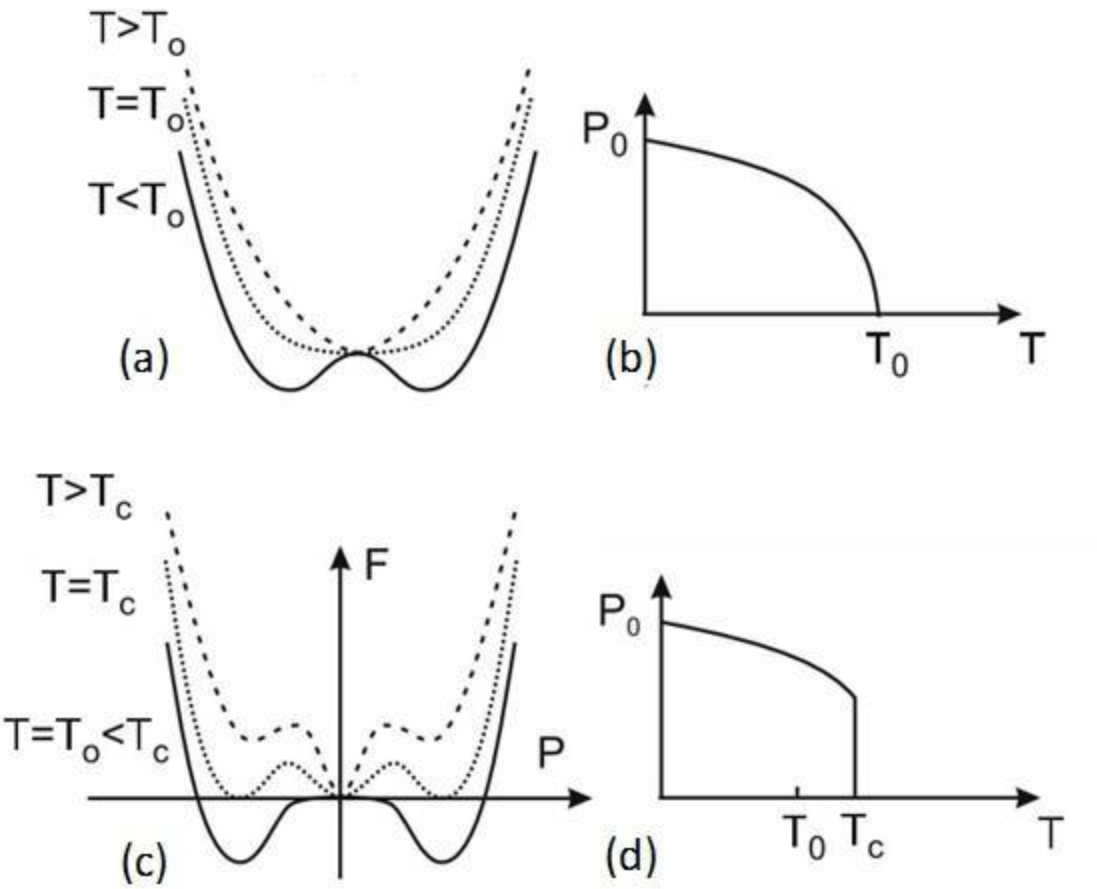

Figure 2. (a) Energy profile at various temperature ranges and (b) polarization vs. temperature for a second order phase transition. (c) Energy profile at various temperature ranges and (d) polarization vs. temperature for a first order phase transition.[11]

1.3.2 Ferroelectric Materials

Neumann's principle states that the symmetry of a crystal has an influence on the observed physical quantities from that crystal. If a crystal remains invariant for certain symmetry operations, then its physical properties must also be invariant. This is important for classifying crystal point groups based on the physical phenomena they exhibit. Each group has certain non-zero and independent elements in their property tensor that are determined by the symmetry operations and indicative of the (an)isotropy in the physical properties for a given crystal. Out of 32 point groups,

20 non-centrosymmetric crystals show piezoelectricity but only 10 of them which has a unique polar axis is pyroelectric. All FEs belong to the remaining 10 classes; however, not all pyroelectrics are ferroelectric because of the inability to switch the direction of the polar axis with external field.[26–30] Point group classification of electrical properties are shown in Figure 29.

FEs can be divided into four distinct classes based on the crystal structure they possess: (i) oxygen octahedral, (ii) tungsten-bronze, (iii) pyrochlore and (iv) bismuth layer-structured. Among these, the first group includes ABO_3-type perovskite structures which have been studied extensively and utilized mostly in technological applications. Lead titanate (PTO), barium titanate (BTO), PZT [$Pb(Zr_xTi_{1-x}O_3)$, (PZT x/1-x)], barium strontium titanate ($Ba_xSr_{1-x}TiO_3$, BST), potassium niobate ($KNbO_3$, KNO) and lithium tantalite ($LiNbO_3$, LTO) are some examples of the materials with perovskite structure.[27,31] The atomic positions in the unit cell above and below the phase transition temperature for ABO_3 crystals corresponding to PE and FE states, respectively, are shown in Figure 3. A-type atoms are located at the corners whereas the B-type ones are sitting at the body centered locations. Oxygen atoms are positioned on face centered cites. The loss of the symmetry of the crystal due to relative displacement of ions below the phase transition temperature [Figure 3(b)] give rise to a net dipole moment. Note that only one polar direction is shown in the ferroelectric state among all equivalent six directions for illustration purposes. The number of equivalent energy states in three-dimensional case is increased to six compared to the two equivalent states for a one-dimensional description [Figure 2(a) and (c)].

The antiferroelectric (AFE) materials differ from FEs in a way that adjacent dipoles are aligned opposite to each other giving a macroscopic net zero polarization. However, it is possible to align these dipoles in the same direction via applying a moderate electrical field since AFE and FE states are close in energy. A net macroscopic polarization is obtained at a field corresponding

to AFE-FE phase transition. This means the FE loop opens up when sufficient electrostatic energy is provided to the system, therefore the P-E curves of AFE have double hysteresis loops as seen in Figure 31(d) in Appendix. More detailed information on physics of AFEs, materials and applications are given in Refs.[32–37] Another group of materials with peculiar properties are relaxor FEs. These materials are in a cubic PE state at high temperatures. When they are cooled down to a critical temperature, a compositional order-disorder phase transition occurs. This critical temperature is called the Burns temperature. Unlike displacive phase transitions such as those observed in PTO, there is no structural displacement in relaxors and the cubic symmetry is maintained. There are mobile nanometer polar regions close to Burns temperature. Further cooling the material down immobilize such nano regions. The structure goes into a non-ergodic state with the freezing of dipole dynamics. This point is where interesting dielectric properties are realized. The relaxors have diffuse dielectric response and high dielectric constants unlike FEs where there is a maximum in the dielectric permittivity right at the phase transition [See Figure 31(d) in Appendix for a typical hysteresis loop]. Moreover, the dielectric constants are highly responsive to changes in the frequency of the field. Relaxors are attractive in electromechanical devices such as transducers, sensors and actuators. More detailed information about relaxors can be found in Refs.[27,38–43]

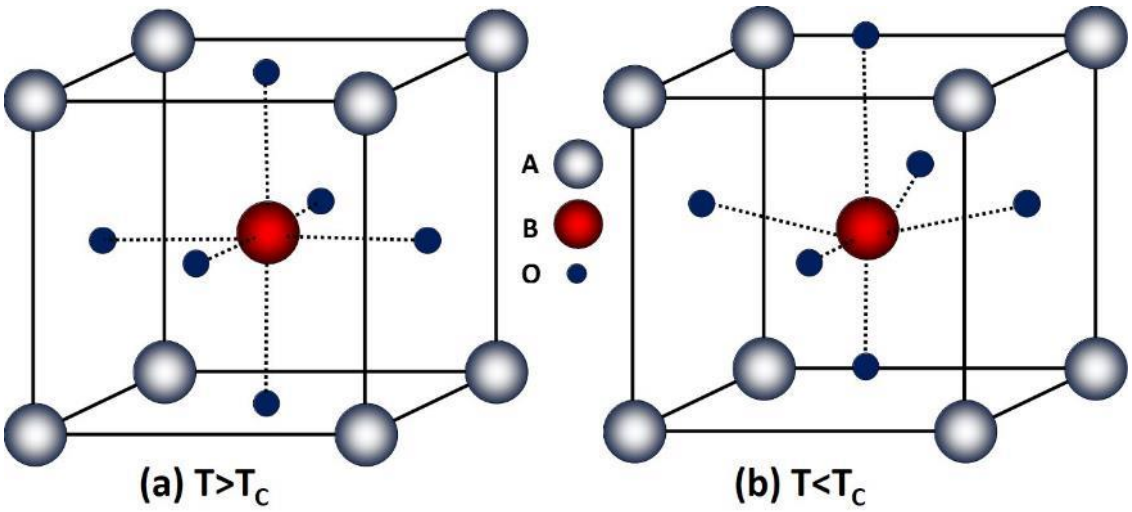

Figure 3. Schematic of ABO_3 type perovskite structure in the (a) paraelectric and (b) ferroelectric state.

1.3.3 Domains in Ferroelectrics

Domains are regions of uniform polarization in a FE crystal and can be formed due to strain, electrical and mechanical defects, thermal and electrical history of the crystal. Although the polarization within a domain is constant, there must be spatial changes in polarization when going through one domain to another. The regions where the polarization inhomogeneity observed are domain walls which have interesting properties and affect the electrical properties of a FE crystal such as their contribution to the external dielectric, pyroelectric and piezoelectric response.[44–47] A uniform polarization (monodomain) in a FE crystal is usually not the most stable state especially in FEs without electrodes at the surfaces. Monodomain configuration necessitates that the positive and negative charges are separated at opposite surfaces of the FE [Figure 4(a)]. This is not a stable state for electrostatic considerations since the charges of electrical dipoles are not compensated by any means. As a consequence, there are electric/depolarizing/stray fields towards the opposite of polarization direction which try to reduce the polarization. The strength of the depolarizing fields is proportional to magnitude of polarization and can be much larger than the coercive field of FE.

For instance, a FE with a 0.1 C m^{-2} polarization would face against a field of 10^3-10^5 kV m^{-1}. Instead of terminating the ferroelectricity, the crystal can split into domains to counteract this field if the domain formation is feasible for a given condition.[48–50] Commonly observed domain structures in a FE undergoing a cubic to tetragonal phase transition are 90° and 180° domains and their combinations.[51,52] A simple 180° domain configuration is illustrated in Figure 4(b). The stray field is eliminated by the FE in a periodic polarization up and down configuration which ensures that each negative charge is compensated by the neighboring positive charges and vice versa.[53] The domain walls may have different structure for a given condition. Polarization goes to zero gradually without changing its direction (no rotation) and grow in the opposite direction after switching back within the width of a domain wall. Such a domain wall type is called Ising wall [Figure 30(a)]. On the other hand, within Néel and Bloch type walls, polarization vector also needs to rotate in x- and x-, y-directions, respectively, in cartesian coordinates in addition to decreasing its magnitude. Various types of domain walls observed in FEs can be found in Figure 30 in Appendix. Rotation of the polarization vector from the polar axis in domain walls comes with an energy penalty to stabilize the crystal in this configuration. Mixtures of these wall types are also observed in FEs. Depending on the electromechanical and electrostatic conditions, various types of domains and domain walls can be stabilized in FEs.[54]

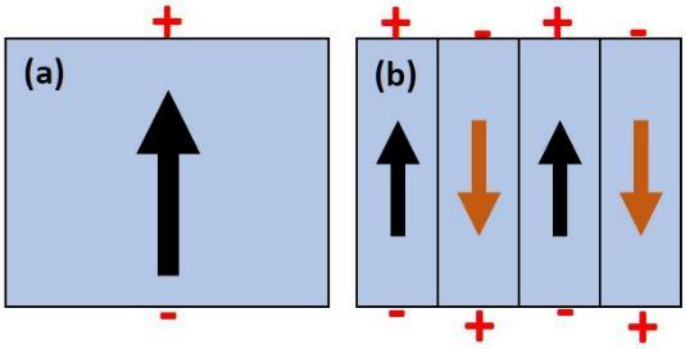

Figure 4. Schematic representation of a (a) monodomain and (b) 180° domain configuration of a FE crystal.

Electrodes are deposited on the FE surface to compensate for the bound surface charges; however, there is no electrode that can perfectly compensate these charges in reality.[55,56] The incomplete compensation of electrical dipoles at the surface of the crystal by the electrode generates depolarizing fields. Such fields can destroy the stability of a single domain state and may cause domain splitting in the FE. However, crystal can be electrically poled to force the monodomain state in a FE. Monodomain state in a FE can also be induced by depositing ultrathin films.[57,58] The domain formation energy for an ultrathin film is so high that monodomain state can be stabilized in the FE through reduction of polarization. There is also a chance that ferroelectricity may completely disappear since the surface and size effects become overwhelming.[59–61] FE has to cope with these effects but it cannot split into domains. In this case, FE crystal kills the polarization. FE polarization is strongly coupled to lattice and unlike their magnetic counterparts, polarization rotations cannot take place along longer distances due to high anisotropy associated with polarization-strain coupling.[8,54] This is why more exotic and unique domain variants are more common in ferromagnets compared to FEs. The multi-to-single domain transition is highly dependent on electrical and mechanical boundary conditions, therefore different domain structures

and their mixtures can be observed in FEs. Here, the emphasis is focused on the competition between depolarizing fields and the domain formation energy.

More recently, the observation of unique domain patterns has been reported both theoretically and experimentally in superlattices (SLs), ultrathin films and low-dimensional structures such as nanopillars, nanoislands, nanodisks and nanowires. These exotic domain structures include flux closure domains, vortices and skyrmions.[62–72] Aguado-Puente and Junquera[73] reported stabilization of closure domains in BTO thin films with $SrRuO_3$ electrodes that are similar to the ones observed in ferromagnets from first principles simulations. They argued that the electrode plays a critical role in the stabilization of such a closure structure. The in-plane displacements of Sr and O atom at the first layer of the electrode was thought to be the origin of closure domain formation. It was also discussed that there remains the question of the FE nature of the thin film since the polarization needs to be switchable. Flux-closure domain structures have been observed in nano FEs such as nanodots and lamella at the mesoscale.[64,67,74] Chang et al.[68] observed formation of nested flux-closure domain structure on the edges of a FE $[Pb(Zn_{1/3}Nb_{2/3})O3]_{0.88}[PbTiO_3]_{0.12}$ sheet. This material has a morphotrophic phase boundary (MPB) and it was thought that the observation of exotic domain structures are more likely than a simple tetragonal. At/near the MPB, polarization can be oriented in different directions easily and new phases/phase mixtures can appear.

It was found that the resulting domain patterns is highly sensitive to the choice of the substrate that FE is mounted. Flux-closure structures have also been spotted in PTO and BTO thin films and SLs.[72,75] The stabilization of a flux-closure necessitates the generation of huge amount of disclination strains because of the strong polarization-strain coupling in the FE. It was reported that strain gradient up to 10^9 m^{-1} ruptures the FE lattice very close to the core of the flux closure

pattern because that amount of strain exceeds the shear strength of the FE. Estimated strain gradients larger than 10^7 m^{-1} was also reported for BTO-STO SLs.[72] Vortex structures have also been observed in FE SL, nanodot and nanoplatelets.[22,63,76–78] Yadav et al.[63] showed stable vortex structures in BTO-STO SLs. It was found that there is asymmetry in the observed domain structures so that the centers of the cores are not aligned perfectly. It was argued that such an asymmetry may be responsible for the source of chirality and possible tunable optical properties. Phase field studies have shown the existence and stability of vortex structures.[63,79] The stability of vortex structures depends on the interplay between long range electrostatic, short range polarization gradient and long range elastic energies and it was found that there is a critical upper and lower bound for SL thickness that these vortices are stable which is related to width of the domains.[79] Chiral skyrmionics structures have been observed in magnetic materials; however, such states are not stable in bulk FEs. More recently, stable skyrmionic states was observed in BTO nanowires that are embedded in a STO matrix using firsts principles. It was shown that skyrmionic state can be induced due to interaction between confined geometry and dipolar interactions. The structure of the skyrmion revealed that topological charge density split into fractions that are pinned at the domain wall junctions.[65] It was shown via phase field simulations that vortex domain structure can be induced by mechanical load.[76] The authors demonstrated that the magnitude and direction of toroidal moment can be changed by applying stress which give rise to different domain structures including vortices. The research on the exotic domain patterns is in its infancy since the difficulties in processing such structures. Moreover, the resulting domain patterns should be reproducible, stable and tunable with an external stimulus such as stress and electrical field before even considered for practical applications. Nevertheless, FE nanoelectronics are attractive in sensor, transducer and memory applications.[76]

1.3.4 Size Effects in Ferroelectrics

There have been numerous studies since the mid-20th century to investigate the size effects in FEs in bulk, powder and thin film forms (e.g. grain and particle size, film thickness).[57,80–93] Earlier studies revealed that the phase transition temperature of tetragonal PTO and BTO is reduced with decreasing particle size, eventually transforming into a PE state at RT.[80–83,86,94,95] The reduction in T_C and the FE-PE phase transition at a critical particle size was observed using variety of characterization techniques including XRD[80,82], DSC[94], Raman Spectroscopy[81,95] and P-E measurements.[96] Both in-plane (a) and out-of-plane (c) lattice constants can be obtained from XRD measurements. With the reduction of c/a ratio, i.e. reduced tetragonality of the FE phase, T_C decreases and at a critical grain/particle size, tetragonality goes to unity where FE-PE transition occurs. Other possible ways to capture FE-PE transition is to track down the frequency of the active phonon in the FE mode via Raman Spectroscopy or analyzing the transition peaks from a DSC spectrum at different grain/particle sizes.

It is intuitive at first that as the particle size of a FE is continuously reduced, ferroelectricity would vanish at some point due to collective nature of the FE polar crystal with long range dipole interactions. This is the intrinsic size limit of the FE; below which ferroelectric state cannot be stable. Finding this limit experimentally is extremely complicated because of extrinsic contributions such as domain structure, electrical, mechanical and chemical defects, external and internal stresses, electrode-FE interactions, and grain boundaries. Moreover, form and shape of FE, processing method and conditions also play a huge role in determining an intrinsic size for the vanishing of ferroelectricity for a given FE material.[86,88,89] Surface tension was considered to be a contributing external factor for the reduction of T_C in nanograined ceramics and powders.[80] The internal hydrostatic pressure generated from the surface effect was thought to be analogous to

reductions in T_C upon the application of an external hydrostatic pressure as studied both theoretically[97,98] and experimentally.[99,100] However, it should be noted that the geometry of the FE crystal and direction of the applied pressure influence whether T_C is shifted to or away from RT. Mechanical stresses that favor tetragonal structure (higher c/a ratios) increases the stability of the FE phase and thus increases the T_C.[101,102]

It was argued that the surface tension effect by itself cannot be responsible for the reduced T_C since several GPa of pressure is required to stabilize the PE state.[103,104] In fact, other external factors and surface tension listed in this section and the electrostatic interactions are responsible for the loss of stability of the FE state.[93] It was shown theoretically using Landau-based approaches that a critical size effect from ferroelectric nanostructures can be captured by considering surface tension and depolarizing affects.[61,105–107] The correlation radius/volume of ferroelectricity, below which FE state is not stable due to polarization fluctuations, was suggested to be around the unit cell scale to few nanometers.[108] However, the exact number is still not clear due to complications in the external factors at the nanoscale as mentioned before. An exact correlation length has not been demonstrated yet and the findings for SL and ultrathin film structures clearly show ferroelectricity at such small length scales.[89,93,109]

Fong et al.[110] showed ferroelectricity in 3-unit cell-thick PTO ultrathin films with tiny stripe domains. It was also shown that polarization of a PZT film is significantly reduced below 4 nm thickness; however, polarization values approximately 0.22 C m^{-2} can be obtained from a 2-unit cell-thick film which was attributed to strong covalent Pb-O bonds. Using a first principle based approach, Lichtensteiger and Triscone[57] demonstrated that PTO films lower than 5 nm display significantly reduced polarization values at 0K than thicker films due to depolarizing fields while maintaining FE state. XRD analysis of 2.4 nm-thick films revealed that c/a ratio is still higher

than unity. In a different DFT study[111], the monodomain FE state in PTO was shown for 1-unit cell-thick films considering electrode screening (realistic electrodes) and depolarizing fields. On the other hand, ferroelectricity disappeared even for 4-unit cell-thick films of BTO. The difference was explained in terms of different work functions of PTO and BTO leading to different screening of bound charges by the electrodes. Overall, FE state can be stable in films with a few unit cells thickness.

1.3.5 Ferroelectric and Ferroelectric-based Heterostructures

Another way to manipulate the functional properties of FEs is by constructing artificial multilayer heterostructures. FE/PE or FE/DE multilayers, SLs, and compositionally graded stacks demonstrate peculiar electrical properties as compared to their bulk and single-crystal equivalents due to electrostatic and electromechanical interlayer interactions.[112,113] Such interactions alter the electrical potential and strain field in the heterostructure and may lead to, for instance, observation of unique domain patters, Curie temperature shifts, and entire suppression of spontaneous polarization.[57,77,114] Theoretical studies show that there exists a dielectric anomaly in coupled FE-PE bilayers at a critical PE layer fraction (α_C) associated with the disappearance of the ferroelectric response.[115] This phenomenon is similar to the dielectric maxima observed near T_C in monolithic FEs and can be used to enhance second-order property coefficients, namely dielectric constant and pyroelectric coefficient, near α_C. The theoretical results obtained from Landau-based analyses have shown to be in good agreement with the experimental values of dielectric permittivity values for STO-PTO epitaxial SLs[116] and polycrystalline bilayers.[117]

Artificial SL structures have some interesting electrical properties due to electrostatic and electromechanical interaction between layers. The presence of interfaces in artificial SL structures alter the average electrical response of the heterostructure. It has been shown experimentally that

a SL configuration offers enhanced electrical properties compared to that of monolayer counterparts that made up the structure and the monolithic alloy of the same SL composition.[116,118–120] Moreover, the electrical properties of SLs can be fine-tuned by designing the layer configuration and geometry, total thickness, layer periodicity and the choice of film/substrate combination. This way, it is even possible to maximize the electrical properties in a SL configuration as shown both experimentally[118–129] and theoretically.[130–137] The enhanced properties of SLs originate from different sources including electrostatic and elastic interactions between layers and reduced size effect. Moreover, the resulting domain structure due to interaction of such physical effects can also influence the electrical properties of SLs. In an earlier study, Nakagawara et al.[119] showed that the dielectric permittivity of BTO-STO SLs increase when the thickness of each layer is decreased (number of repeating units are increased) for a fixed total thickness of 100 nm with permittivity values going as high as 600 and exceeding the value of a BST-STO solid solution film. It was argued that the in-plane pressure between individual layers in the SLs can be responsible for the enhancement in dielectric properties. Similar trends in relative permittivity *vs.* layer periodicity were also observed from BTO-STO[118,122] and $PbZrO_3$/PTO[120] SLs. It was shown that SLs with thinner individual units have a reduced T_C compared to the ones with thicker layers. Not only the size effects become important for thinner layers but also the interactions between FE layers was suggested to alter the phase transition characteristics of FE-PE SLs. Two separate experimental[138] and theoretical[131] analysis showed that the T_C decreases in KNO_3/$KTaO_3$ when the repeating unit periodicity is decreased gradually. As the layer periodicity is reduced, the FE layers interact with each other and the domain structure of the FEs couple strongly with each other as determined by the global depoling field in the SL which tends to decrease T_C. On the other hand,

depoling fields are concentrated at the FE-PE interfaces for SLs with larger periods, thus the interaction between FE layers are rather weak.[138]

In addition to interesting dielectric and electrothermal properties, thin film heterogeneous FEs also exhibit unique interfacial phenomena. The formation of a two-dimensional electron gas in dielectric (e.g. $LaAlO_3/SrTiO_3$) and wide-bandgap polar heterostructures such as GaN- and ZnO-based systems have attracted interest in electronics applications.[139,140] Magnetoresistance effects have been observed in ferromagnetic and antiferromagnetic based multilayer constructs that can be used in sensing and memory applications.[141,142] Switchable polarization of a FE opens up the opportunity to control the charge transport characteristics at the FE/metal and FE/SC heterointerfaces. Carrier manipulation near such regions can be used in high density memories, switchable diodes, and photovoltaic devices. The origin of the switchable diode effect from bismuth ferrite ($BiFeO_3$, BFO)-SC heterostructures has been a subject of debate for some time. It was argued whether the diode effect is due to interfacial or bulk in origin. The interfacial effect was suggested to arise from the oxygen defects that are pinned at the FE-electrode interface and inducing rectifying diode characteristics.[143,144] On the other hand, the bulk effect was thought to originate from the FE polarization and its direction.[145] It should be noted that these two phenomena are actually more or less similar/related physically. It is well known that oxygen defects and cation deficiency makes an insulating FE a SC. When a SC is in touch with a metal (electrode), Schottky-like junctions form at the interface and carrier accumulation/depletion result in formation of potential barriers that gives the directional anisotropy in current density responsible for the diode effect. The diode effect in the reverse direction can be achieved by changing the polarization state (direction) of the FE. An example schematic is shown in Figure 5(a) for a BFO-SRO heterostructure. The positively charged oxygen defects pole the FE film to align the polarization

vector downwards so that the negative charges are accumulated at the top electrode-FE interface giving rise to anisotropic current transport along the heterostructure thickness that is responsible for the diode effect.[145]

Voora et al.[146] attributed the diode-like behavior of a BTO/ZnO heterostructure to the polarization in the BTO layer but did not rule out the effects of interfacial defects and charges. The *I-V* curves *vs*. temperature revealed that above the phase transition (PE state), the diode-like behavior still persisted. Similarly, the diode behavior of a BFO-ZnO structure accompanying a hysteresis in the *I-V* curves was also shown in Ref.[147] The band bending at the BFO-ZnO interface was proposed to arise because of the formation of a p-n junction at the interface. BFO films were p-type SCs, whereas the ZnO was a n-type SC. It should be emphasized that the thermionic emission at heterointerfaces obviously depends on the temperature; therefore, not only the polarization state of a FE is important in setting the energy barrier at such interfaces but also any changes in temperature contribute to changes in the potential. The current ON/OFF ratios are fairly important when designing a memory. In other words, the two states need to be distinct and distinguishable. What is probably more important is that the current retention characteristics of the memory should be very good that the ON/OFF currents need to be stable over time and number of switching operations (retention characteristics). The latter is probably the reason why memory devices that utilize FE up and down switching have not been used extensively in applications because of ferroelectric fatigue and imprint. Jiang et al.[143] showed that the ON/OFF currents in a $BiFeO_3$-$SrRuO_3$-STO system can be stable over 10^6 s. On the other hand, the appearance of fatigue in the heterostructure after some switching operations significantly changed the polarization values and the current density. This finding also supports the other studies that the polarization state affects the diode behavior of the heterostructure.

Ferroelectric tunnel junctions (FTJs) have recently been considered as promising heterostructures for their potential application in non-volatile memory devices making use of resistive switching phenomenon. With the advancements in thin film deposition technology, high quality few nm-thick FE films can now be synthesized. FTJs make use of the quantum electron tunneling phenomena where electrons can be transported across a potential barrier that is classically forbidden.[148,149] It has been theoretically shown that FE polarization switching can induce tunneling electro resistance (TER) effect. TER effect is much more significant in heterostructures with asymmetric electrodes and/or asymmetric layer structures. The potential barrier between the film and electrodes are altered in such systems, thereby changing the electron transport characteristics.[148,150–155] A schematic of a typical FTJ with a representative band diagram is presented in Figure 5(b). Hole accumulation in the correlated oxide layer due to upward polarization (red arrows) activates more carriers to flow through the direction of FE polarization, thus increasing current density. When the polarization is switched, the potential barrier increases and this results in low current density transport across the heterostructure. The conductance difference/ratio is responsible for the TER effect.[156] It has been shown experimentally that high conductance ratios can be achieved using FTJs.[149,156]

FEs can also be utilized as gate oxides in a metal oxide field-effect transistor configuration for non-volatile memory applications. It has been shown both theoretically and experimentally that distinct memory states in the SC channel can be induced by changing the carrier concentration/distribution at the SC-FE interface through polarization in the FE gate layer.[157–167] A schematic of a PZT-ZnO field-effect transistor is shown schematically in Figure 5(c). A single domain configuration in the FE where polarization points downward depletes the SC channel in the OFF state. On the other hand, full carrier accumulation can be realized when the FE

polarization is reversed by applying an electric field. It is worth mentioning that polydomain structure obtained at the intermediate steps during switching can also increase the carrier concentration at the channel which is also dependent on the width of the domains as well. Misirlioglu et al.[166] showed that it is possible to induce ON/OFF states in the channel at low voltages using a Landau-Ginzburg-Devonshire (LGD) approach without the need for FE switching. This is useful for low voltage operation and limiting possible ferroelectric fatigue. Although FFETs offer potential to be utilized as non-volatile memory devices, there are some practical limitations that prevent realizing the full potential of such heterostructures. The most serious problem is the short retention time of this devices due to leakage in FE, the presence of depolarizing fields and interface quality of FE-electrode interface. Apart from increasing the quality of films through process control, the use of a buffer layer was suggested to improve the FE-electrode interface. The deposition of an insulating buffer layer between the FE and electrode; however, requires higher voltage operation due to voltage drop across the FE in this configuration. Moreover, the depolarizing fields generated through introduction of buffer layer deteriorate the retention performance of the structure.[158–161] Nevertheless, FFETs are still promising and attractive for use in memory applications if the above-mentioned problems can be limited.

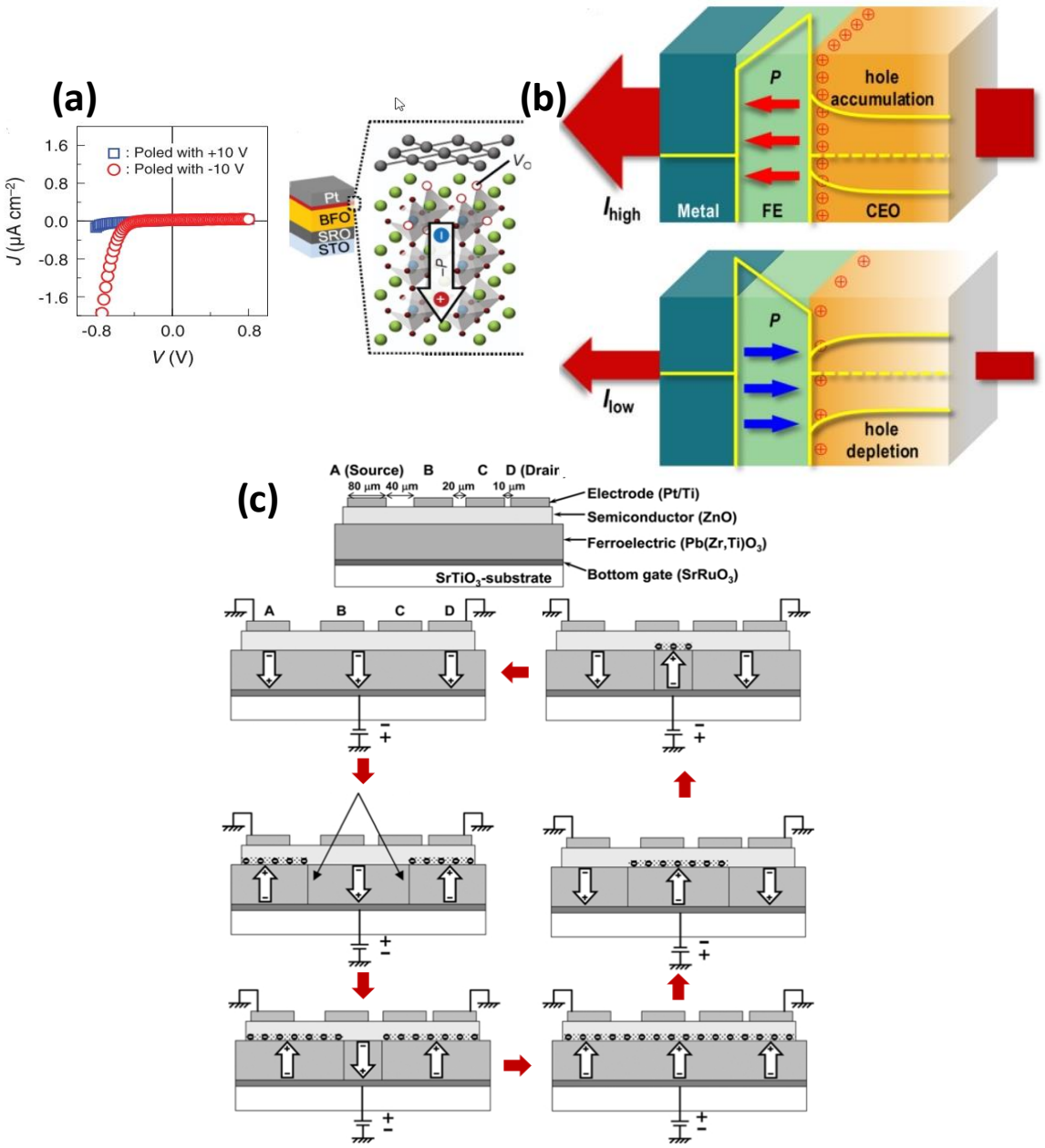

Figure 5. (a) Schematic and I-V characteristics of BFO-SRO heterostructures with a zoomed in picture showing oxygen defects at the Pt-BFO interface.[145] (b) Schematic of a FE-correlated metal oxide heterostructure tunnel junction showing how the direction of the polarization induces the high and low resistance memory states by flooding or depleting the charge carriers at the FE-oxide interface.[156] (c) Schematic of a ferroelectric field effect transistor showing the dynamic control of channel (ZnO) conductance through ferroelectric switching.[160]

1.4 Rationale of the Thesis

Integration of FEs with microelectronic devices necessitates that these materials are deposited in thin film form with reduced dimensions. The processing conditions for FE thin films and the thin film configuration itself generate strain fields that couple with polarization and may alter the electrical properties drastically (negatively, in many cases) compared to bulk. Moreover, the heterostructure configuration changes the electrostatics of the system. The main motivation of this thesis is to be able to guide the experimental work by looking at how certain processing parameters can affect dielectric, pyroelectric, and EC properties of FE heterostructures on IC compatible substrates. The goal is to identify specific set of (physical) parameters for experimental design that can yield enhanced electrical properties.

Here, a non-linear thermodynamic model that takes into account the thermal stresses that develop during cooling from the (growth temperature) T_G and electrostatic coupling between the layers that make up the multilayer construct is utilized. The quantitative results from such multilayers will be compared to that of monolayer films and in some cases bulk counterparts. The dielectric and pyroelectric properties and phase transition characteristics of heteroepitaxial SL stacks are also presented and the role of a SL configuration on the electrostatics of the system and the resulting domain structure is discussed.

The specific objectives of the current work can be summarized as follows:

- To understand the effect of $SrTiO_3$ (STO) layer fraction in a FE/STO multilayer on the dielectric properties. This may help in designing the overall composition of the multilayer system to get the highest possible dielectric permittivity.

- To explain the change in dielectric properties of a FE/STO multilayer thin films as a function of growth/annealing temperature and the choice of multilayer substrate pair. This may provide information on how to choose a growth temperature to obtain the maximum dielectric response for each multilayer-substrate system (if a change in growth temperature is feasible for the experimental setup).
- The impact of electrostatic coupling strength on the electrothermal properties will be analyzed via comparing the pyroelectric coefficients and adiabatic temperature changes of $BaTiO_3$ (BTO)-$Pb_{0.8}Zr_{0.2}TiO_3$ (PZT 20/80 or PZT) and STO-PZT 20/80 systems. This may give insight which material pair performs better for a given electrical field and temperature.
- To understand how the phase transition characteristics of PZT-STO epitaxial heterostructures are affected by the layer periodicity, layer thickness and number of repeating units and to compare the resulting dielectric and pyroelectric properties. This may give further flexibility in designing novel SLs by changing simple experimental conditions using same material and deposition systems.

CHAPTER II: Theory of Phase Transitions and Theoretical Methodology

2.1 Overview of the Commonly Used Methods to Model Ferroelectric Phase Transitions

The most commonly utilized methods to model ferroelectrics are thermodynamic, phase field, and first principles approaches. The former includes well-known Landau expansion of free energy density with polarization as the order parameter. Although it assumes averaging of local polarization fluctuations, surface and size effects can still be modeled via introducing boundary conditions and gradient terms, therefore making these methods attractive and versatile to study thin/ultrathin FE films.[9,11] One needs to resort to phase field models when analysis of domain dynamics during transition and switching in detail is of interest.[168,169] On the other hand, first principle based approaches provide information at the unit cell level and do not require phenomenological constants to predict the ferroelectric properties. Phase diagrams, phonon frequencies, and elastic constants can be obtained using such methods.[170]

2.2 Bulk Landau Energy

The physical picture of a structural phase transition can be explained using the soft mode concept from an atomistic perspective. The instability of a certain lattice vibration (phonon) mode at the critical point is responsible for the FE phase transition. It was shown that the total energy of the system can be approximated by a series expansion of the amplitude of such a vibration mode since the contribution of other modes becomes much less significant.[171,172] Landau-based approaches, on the other hand, assumes averaging of physical quantities in the lattice and hence, are continuum based in nature. Within this framework, the polarization need not necessarily

correlate with the amplitude of the phonon mode responsible for the phase transition: it is rather a macroscopic quantity that describes the phase transition. Landau and later Devonshire formed the basis of the theory and it was shown that dielectric properties of BTO can be calculated with a polynomial and very good agreement with the experimental values can be obtained within a broad temperature range far from the critical point.[172–175] Landau Theory of Phase Transitions is a symmetry based analysis to model ferroelectric phenomena and it is valid above and below the critical point. The most important rule in constructing a free energy expression in Landau-based approaches is that the energy has to be invariant under operations of the parent phase's symmetry group. This means if one wants to include additional terms (e.g. elastic, electrostatic) to the total energy, the symmetry requirements/constraints has to be preserved. For instance, the elastic strain during a phase transition has its own vibration mode which is not proportional to the amplitude of the mode that is responsible for the ferroelectric transition. However, the elastic energy, for instance, can still be included as long as the symmetry constraints are preserved.[172] The bulk Landau energy with polarization as the order parameter has the following form for a FE undergoing a transition from the high symmetry PE cubic phase to a tetragonal FE state:

$$G_L(P_i,T) = G_{0,i} + \alpha_1 P_i^2 + \alpha_{11} P_i^4 + \alpha_{111} P_i^6 - EP_i \qquad (8)$$

The energy is simply a Tylor expansion right near the critical point. The odd terms are omitted when the electric field E is zero so that the mirror symmetry is maintained.[10] This way the energy equivalent FE states, $+P$ and $-P$ can be captured. The last term in Equation 8, $-EP_i$, is the electrostatic energy. P_i are the polarization components and E is the externally applied electric field. α_{ij} is the dielectric stiffness coefficients. The electric field is linearly coupled to polarization in Equation 8. As a consequence, depending on the field direction, i.e. sign of the field, the symmetry of the polynomial is broken favoring one polarization value over the other that has a

different sign. It should be noted that the bulk energy shown in Equation 8 is for a general uniaxial problem and the complete energy expression with all the dielectric stiffness coefficients and polarization components are given in the proceeding section. The quadratic coefficient α_1 is given by the Curie-Weiss Law, $\alpha_1=(T-T_{C,i})/2\varepsilon_0 C$, where ε_0 is the permittivity of free space, C is the Curie-Weiss constant, and T_C is the Curie temperature. The other stiffness coefficients are known to slightly depend on temperature which is usually neglected in the analysis. The Landau Theory breaks down very close to the critical point since the fluctuations in the order parameter become significant. This is because the correlation length which defines the length scale of polarization diverges very close to critical point and hence cannot be described by the polynomial in Equation 8. The correlation length can also be described as the maximum distance between two points in space where the polarization is "*felt*" in between. If it diverges in the limit of T $\rightarrow$ T_C then that means the polarization fluctuations become significant in the entire FE. It should be emphasized that the form of the energy expression is different for systems with different symmetries.

The condition for thermodynamic equilibrium is derived from the dielectric equation of state:

$$\frac{\partial G_L}{\partial P} = 2\alpha_1 P + 4\alpha_{11} P^3 + 6\alpha_{111} P^5 = E \tag{9}$$

To find the equilibrium polarization value, one has to set the derivative to zero in the above equation: the polarization value that minimizes the energy is the equilibrium polarization of the system. Once the equilibrium polarization is known; relative dielectric permittivity (ε_R) or dielectric constant, pyroelectric coefficient (p) and adiabatic temperature change (ΔT) can be calculated from the following equations:

$$\varepsilon_R = \frac{1}{\varepsilon_0}\frac{dP}{dE} \tag{10}$$

$$p = \frac{dP}{dT} = \frac{dP_S}{dT} + \int_0^E \left(\frac{\partial \varepsilon_R}{\partial T}\right)_E dE \tag{11}$$

$$\Delta T = -\int_{E_a}^{E_b} \frac{T}{C_E}\left(\frac{\partial P}{\partial T}\right)_E dE \tag{12}$$

where C_E is the total heat capacity of the FE consisting of the excess heat capacity and lattice contributions fitted from experimental data. The second term in Equation 11 is the dielectric contribution to the pyroelectric coefficient. The value is negligible in the FE state since the spontaneous polarization term dominates.

2.3 General Free Energy Expression for Cubic-Tetragonal Ferroelectric Phase Transition

The total free energy for a FE that undergoes a cubic to tetragonal phase transition reads:

$$G_{FE} = G_0 + G_L + G_{ES} + G_{EL} + G_G \tag{13}$$

where the energy terms from left to right are the total energy of the reference PE state (G_0), landau bulk energy (G_L), electrostatic energy (G_{ES}), elastic energy (G_{EL}) and the gradient energy (G_G), respectively. G_0 is taken as zero in order to obtain excess free energy change $\Delta G = G_{FE} - G_0$ from the phase transition itself. $G_0 = U_0 - TS_0$ where enthalpic contributions to total energy of the system due to interatomic bonding is included in U_0 and the entropic contributions such as configurational and vibrational entropy are included in the second term. It is important to repeat here again that Landau theory describes the energy change due to phase transition not the total energy of the entire system. The bulk Landau energy follows from:

$$G_{FE} = \alpha_1(P_1^2 + P_2^2 + P_3^2) + \alpha_{11}(P_1^4 + P_2^4 + P_3^4) + \alpha_{12}(P_1^2P_2^2 + P_1^2P_3^2 + P_2^2P_3^2) + \alpha_{111}(P_1^6 + P_2^6 + P_3^6) + \alpha_{112}[P_1^4(P_2^2 + P_3^2) + P_2^4(P_1^2 + P_3^2) + P_3^4(P_1^2 + P_2^2)] + \alpha_{123}P_1^2P_2^2P_3^2 \quad (14)$$

where Equation 14 is the general expression for the bulk Landau energy including all polarization components, their cross-coupling and all the dielectric stiffness coefficients. Note that this equation is basically an expanded version of Equation 8 which is given for a uniaxial bulk FE. The electrostatic energy is given as $-EP_i$. The elastic energy along all cartesian coordinates is given via:

$$G_{EL} = -\frac{1}{2}S_{11}\left(\sigma_1^2 + \sigma_2^2 + \sigma_3^2\right) - S_{12}\left(\sigma_1\sigma_2 + \sigma_1\sigma_3 + \sigma_2\sigma_3\right) - \frac{1}{2}S_{44}\left(\sigma_4^2 + \sigma_5^2 + \sigma_6^2\right) - Q_{11}\left(\sigma_1P_1^2 + \sigma_2P_2^2 + \sigma_3P_3^2\right) - Q_{12}\left[\sigma_1\left(P_2^2 + P_3^2\right) + \sigma_2\left(P_1^2 + P_3^2\right) + \sigma_3\left(P_1^2 + P_2^2\right)\right] \quad (15)$$

Here, the stress tensor in Voigt notation is indicated as σ_i (i=1,2,…,6). S_{ij} and Q_{ij} are the elastic compliances and electrostrictive coefficients, respectively. Electrostriction is a property of any DE where an applied field causes a change in the crystal's shape. This is neglected in the bulk analysis since whole crystal is allowed to expand/contract along any direction in space. Elastic energy of a FE system can be modified with external stress or the configuration/geometry of the system. For instance, internal elastic energy due to the mechanical boundary conditions in a thin film configuration requires σ_1=σ_2 and σ_3=σ_4=σ_5=σ_6=0, since the FE film is allowed to expand along the out of plane direction and there are no shear forces acting on the film. This sets the equi-biaxial strain in the thin film. The thin film is said to be "clamped" in such a configuration. The stress components can be eliminated through $d\tilde{G}/d\sigma_i = u_i$ (i = 1, 2). The source of strain in a FE film can be thermal or misfit. Thermal strains (u_T) are generated when FE films are cooled

down from the growth/processing temperature to room temperature because of the thermal expansion mismatch of the film to the substrate. On the other hand, epitaxial strains (u_m) are formed if the film and the substrate are coherent and hence there is lattice constant mismatch.

Equation 13 can be rewritten as:

$$\begin{aligned}\tilde{G} = {} & \tilde{\alpha}_1(P_1^2+P_2^2)+\tilde{\alpha}_3P_3^2+\tilde{\alpha}_{11}(P_1^4+P_2^4)+\tilde{\alpha}_{33}P_3^4+\tilde{\alpha}_{13}(P_1^2P_3^2+P_2^2P_3^2)+\tilde{\alpha}_{12}P_1^2P_2^2 \\ & +\alpha_{111}(P_1^6+P_2^6+P_3^6)+\alpha_{112}[P_1^4(P_2^2+P_3^2)+P_2^4(P_1^2+P_3^2)+P_3^4(P_1^2+P_2^2)] \\ & +\alpha_{123}P_1^2P_2^2P_3^2+u_{T,m}^2/(S_{11}+S_{12})-EP_i+G_G\end{aligned} \tag{16}$$

with modified stiffness coefficients are given via:

$$\tilde{\alpha}_1 = \alpha_1 - u\frac{2(Q_{11}+Q_{12})}{s_{11}+s_{12}}, \quad \tilde{\alpha}_3 = \alpha_1 - u\frac{4Q_{12}}{s_{11}+s_{12}}, \tag{17}$$

$$\tilde{\alpha}_{11} = \alpha_{11} + \frac{2}{s_{11}^2-s_{12}^2}\left[\left(Q_{11}^2+Q_{12}^2\right)s_{11}-2Q_{11}Q_{12}s_{12}\right], \quad \tilde{\alpha}_{33} = \alpha_{11} + \frac{4Q_{12}^2}{s_{11}+s_{12}}, \tag{18}$$

$$\begin{aligned}\tilde{\alpha}_{12} &= \alpha_{12} - \frac{2}{s_{11}^2-s_{12}^2}\left[\left(Q_{11}^2+Q_{12}^2\right)s_{12}-2Q_{11}Q_{12}s_{11}\right]+\frac{Q_{44}^2}{s_{44}}, \\ \tilde{\alpha}_{13} &= \alpha_{12} + \frac{2Q_{12}(Q_{11}+Q_{12})}{s_{11}+s_{12}}\end{aligned} \tag{19}$$

It is worth mentioning that the elastic energy here is assumed to be homogeneous in the FE whether the strain is thermal or misfit. In order to consider inhomogeneous strain in the system, one needs to resort to phase field calculations. The elastic equations of state have to be solved along with the dielectric ones to calculate the domain structure and electrical properties of FEs. An additional assumption in this model is that no elastic effects in the electrodes are considered in this study. In other words, only the electrodes contribute to the electrostatic problem by providing short-circuit conditions, perfect charge compensation and providing voltage under bias. The thin films are

assumed to be much thinner than the substrate and the electrode so that the homogeneous strain is confined in the FE layer(s). Additionally, any elastic interaction between individual layers is neglected.

The electrodes are assumed to be ideal with perfect compensation of bound charges. This means the screening length of electrode is infinitely thin that no electric field penetrates into the electrode. If an electric field penetrates into the electrode over a certain thickness that is determined by the screening quality of the electrode, then there would be a voltage drop at the surface creating depolarizing fields. The screening effects can be included in Landau-based approaches as shown in the literature.[176–178] Alternatively, it was also shown that such effects can be modeled by considering a very thin "dead" layer between the film and the electrode to mimic voltage drop due to imperfect screening.[179]

The last term in Equation 16 is the gradient energy due to domain formation and given by:

$$G_G = G_{33}\left(\frac{dP_3}{dz}\right)^2 + G_{31}\left(\frac{dP_3}{dx}\right)^2 + G_{13}\left(\frac{dP_1}{dz}\right)^2 + G_{11}\left(\frac{dP_1}{dx}\right)^2 + G_{23}\left(\frac{dP_2}{dz}\right)^2 + G_{21}\left(\frac{dP_2}{dx}\right)^2 + G_{32}\left(\frac{dP_3}{dy}\right)^2 + G_{22}\left(\frac{dP_2}{dy}\right)^2 + G_{12}\left(\frac{dP_1}{dy}\right)^2 \quad (20)$$

G_{ij} are the gradient energy coefficients. Gradient energy is the energy penalty due to domain formation. The polarization is assumed to be constant at every point in space (in FE) if this term is neglected. In unpoled real crystals, a constant polarization in the FE is usually not feasible due to formation of electrical domains. Equation 20 is introduced to the free energy expression in order to capture local polarization differences/changes in the FE system. The single domain/single domain-like state in the FE can be induced easily by poling the FE crystal (applying electrical field) either at low or elevated temperatures especially for thicker polycrystalline films.[180]

2.3.1 Monodomain Polycrystalline Single Layer and Multilayer Films

FE films usually rapidly cooled from the T_G to the ambient temperature to prevent formation of additional phases and prevent the loss of volatile species from the FE phase such as lead. This may lead to generation of thermal strains in polycrystalline films because of the differences in coefficients of thermal expansion (CTE) of the film and the substrate. This is analogous to lattice constant mismatch in epitaxial thin films. Equi-biaxial in-plane thermal strains that develop in the film due to the differences in CTEs between FE film and substrate upon cooling from T_G can be expressed as:

$$u = u_T = \int_{RT}^{T_G} \alpha_{film} dT - \int_{RT}^{T_G} \alpha_{substrate} dT \tag{21}$$

where $\alpha_{F,i}$ and α_S are the in-plane CTE of the layer *i* and the substrate, respectively. It is assumed that thermal strains are not relaxed through formation of domains and/or cracks.

As mentioned in Section 1.3, the internal fields generated through polarization mismatch between different layers can alter the average polarization of the heterostructure. This effect can be captured by including an additional electrostatic term, $E_{D,i}$ in the energy expression for a bilayer system and is given by:

$$\tilde{G}_\Sigma = (1-\alpha)\cdot(\tilde{G}_1 - \frac{1}{2}E_{D,1}) + \alpha\cdot(\tilde{G}_2 - \frac{1}{2}E_{D,1}P_2) \tag{22}$$

Here, $\alpha=\alpha_2=h_2/(h_1+h_2)$ is the relative thickness (layer fraction) of the second layer where h_1 and h_2 are the thicknesses of first and second layers, respectively, and $h=h_1+h_2$ is the total thickness of the multilayer. $\tilde{G}_i$ is the strain modified energy that also includes the external electrostatic energy (See, Equations 8 or 17). The internal depolarization energy $E_{D,i}$ reads:

$$E_{D,1} = -\frac{1}{\varepsilon_0}[P_1 - < P >] = \frac{(1-\alpha)}{\varepsilon_0}(P_1 - P_2), \tag{23}$$

$$E_{D,2} = -\frac{1}{\varepsilon_0}[P_2 - < P >] = \frac{\alpha}{\varepsilon_0}(P_2 - P_1) \tag{24}$$

The average polarization,. $< P >= \alpha P_1 + (1-\alpha)P_2$. Combining Equations 22-24, the energy expression for the multilayer becomes:

$$\tilde{G}_{\Sigma} = (1-\alpha)\cdot\tilde{G}_1 + \alpha\cdot\tilde{G}_2 + \frac{1}{2}\alpha(1-\alpha)\frac{1}{\varepsilon_0}(P_1 - P_2)^2 \tag{25}$$

The dielectric and electrothermal properties can then be calculated for FE-based multilayers following the procedure in Equations 10-12 by only replacing single layer polarization value with that of the multilayer construct. Depending on the nature of the layers whether they are PE, DE or FE and/or the choice of the layer combinations, the strength of coupling will be different and thus the resulting electrical properties of multilayers.

2.3.2 Polydomain Epitaxial Multilayer Films

The polydomain films considered in this thesis is assumed to be infinite in one of the in-plane dimensions (P_2). Dielectric equations of state follow from combining Equations 16 and 20 and minimizing the total energy with respect to polarization components ($\partial\tilde{G}/\partial P_1 = 0$, $\partial\tilde{G}/\partial P_3 = 0$):

$$\begin{aligned} &2\tilde{\alpha}_3 P_3 + 4\tilde{\alpha}_{13} P_3 P_1^2 + 4\tilde{\alpha}_{33} P_3^3 + 6\alpha_{111} P_3^5 \\ &+ \alpha_{112}(4P_3 P_1^4 + 8P_3^3 P_1^2) + 2\alpha_{123} P_3 P_1^4 - G\left(\frac{\partial^2 P_3}{\partial z^2} + \frac{\partial^2 P_3}{\partial x^2}\right) = E_3, \end{aligned} \tag{26}$$

$$2\tilde{\alpha}_1 P_1 + 2(2\tilde{\alpha}_{11} + \tilde{\alpha}_{12})P_1^3 + 2\tilde{\alpha}_{13}P_1P_3^2 + 6\alpha_{111}P_1^5 + 2\alpha_{112}[3P_1^5 + 3P_1^3P_3^2 + P_1P_3^4] + 2\alpha_{123}P_1^3P_3^2 - G\left(\frac{\partial^2 P_1}{\partial z^2} + \frac{\partial^2 P_1}{\partial x^2}\right) = E_1 \quad (27)$$

Maxwell relation needs to be satisfied in the thin film:

$$\nabla \cdot \mathbf{D} = \nabla \cdot (D_x \vec{i} + D_y \vec{j} + D_z \vec{k}) = 0 \quad (28)$$

where **D** is the dielectric displacement, $D_x = \varepsilon_b \varepsilon_0 E_x + P_x$, $D_z = \varepsilon_b \varepsilon_0 E_z + P_z$. The electric field components are obtained from the electrostatic potential (ϕ) such that $E_x = -\partial\phi/\partial x$ and $E_z = -\partial\phi/\partial z$. Also note that P_1, P_2 and P_3 is also denoted as P_x, P_y and P_z, respectively throughout the thesis. Moreover, all the bulk thermodynamic, elastic, thermal and electromechanical coefficients for the studied systems are shown in Tables 2 and 3.

Table 2. Bulk thermodynamic, elastic, thermal and electromechanical coefficients of the materials used in this thesis. Data compiled from Refs. [181–185]

	PZT 40/60	PZT 30/70	PZT 20/80	PZT 10/90	PZT 0/100 (PTO)	BTO	STO
$T_C(^\circ C)$	418.4	440.2	459.1	477.1	492.1	383	-
$C(10^5{}^\circ C)$	2.664	1.881	1.642	1.547	1.500	1.048	-
$Q_{11}(\mathrm{m^4/C^2})$	0.08116	0.07887	0.08142	0.08504	0.08900	0.110	-
$Q_{12}(\mathrm{m^4/C^2})$	-0.0295	-0.0248	-0.02446	-0.02507	-0.02600	-0.043	-0.0135
$Q_{44}(\mathrm{m^4/C^2})$	-	0.06356	0.06417	-	-	-	0.00957
$s_{11}(10^{-12}\,\mathrm{N/m^2})$	8.6	8.4	8.2	8.1	8	8.3×10^{-12}	3.729
$s_{12}(10^{-12}\,\mathrm{N/m^2})$	-2.8	-2.7	-2.6	-2.5	-2.5	-2.7×10^{-12}	-0.9088
$s_{44}(10^{-12}\,\mathrm{N/m^2})$	-	17.5	14.4	-	-	-	-
$\alpha_{11}(10^7\,\mathrm{N\,m^6/C^4})$	3.614	0.6458	-3.05	-5.845	-7.253	$3.6\times(T-448)\times10^9$	2.03×10^{9}
$\alpha_{111}(10^8\,\mathrm{N\,m^{10}/C^6})$	1.859	2.348	2.475	2.518	2.606	6.6×10^9	-
$\alpha_{12}(10^8\,\mathrm{N\,m^6/C^4})$	-	5.109	6.320	-	-	-	27.4
$\alpha_{112}(10^8\,\mathrm{N\,m^{10}/C^6})$	-	10.25	9.684	-	-	-	-
$\alpha_{123}(10^9\,\mathrm{N\,m^{10}/C^6})$	-	-5.003	-4.901	-	-	-	-
G (10^{-10} m^3/F)		5	5				

Table 3. CTE of FEs and substrates used in this thesis.

Film/Substrate	**TEC, $\times10^6$ ($^\circ C^{-1}$, T in $^\circ C$)**	**Ref.**
PZT 50/50	7.26	[186]
PZT 40/60	7.47	-
PZT 30/70	8.04	[187]
PZT 20/80	8.96	-
PZT 10/90	10.23	-
PZT 0/100 (PTO)	11.86	[188,189]
BST 60/40	$8.90+7.90\times10^{-3}\times T$	[183]
STO	$9.43+3.836\times10^{-3}\times T$	[190]
BTO	$8.545+1.0615\times10^{-2}\times T$	[191]
Si	$3.725\times\{1-\exp[-5.88\times10^{-3}(T+149)]\}+5.548\times10^{-4}\times(T+273)$	[192]
c-Sapphire	$8.026+8.17\times10^{-4}\times T-3.279\times\exp(-2.91\times10^{-3}\times T)$	[193]

Chapter III. Pyroelectric Properties of Polycrystalline Ferroelectrics

3.1 Background Information

Pyroelectric materials have long been employed as single or multi-element passive infrared (IR) devices for intrusion detectors, smoldering fire detectors, uncooled thermal imagers, radiometers, and gas/laser analyzers.[16,194] These detectors are fabricated from either bulk or thin film elements.[195] The pyroelectric response of such devices is commonly used in two different modes of operation. Firstly, for ferroelectric materials operated well below the FE phase transformation (Curie) temperature (T_C) a pyroelectric current is obtained solely due to the change in spontaneous polarization with temperature. Intrusion detectors, gas analyzers are most often used in this mode. Such devices frequently are put into a "sleep mode" when inactive, and waking up upon external stimulus, thereby minimizing power consumption.[196] Temperature variations and their control are not primary concerns in this mode of operation. Secondly, the so-called "dielectric bolometer" mode of operation involves using a FE material close to T_C, with an electric bias field applied, which has the effect of stabilizing a steep temperature dependence of the field induced dielectric displacement, and hence induced pyroelectric effect.[183,197] The applied field also reduces the dielectric loss in the region of T_C, which would otherwise be problematic. The bolometer mode can be advantageous for certain types of device, especially small element thermal imaging arrays, where the high dielectric constant in the region of T_C provides an element capacitance that matches the input amplifier. The need to operate close to T_C necessitates some degree of temperature control, although the range of this is determined by the magnitude of the applied field (higher applied fields broaden the temperature range of optimum operation). Nevertheless, the need for thermal stabilization for dielectric bolometers is disadvantageous in terms of system complexity

and power consumption and means that, for most IR sensing applications, the use of FEs well below T_C provides a wider spectrum of applications.

FE materials, when deposited in thin film form, can exhibit inferior piezoelectric properties compared to bulk and single crystals due internal stresses, the presence of defects, and microstructural/compositional inhomogeneities.[47,198–201] However, it has been shown that it is perfectly possible to obtain pyroelectric properties in FE thin films which compare very well with those of bulk pyroelectric ceramics[202], presumably because such properties are intrinsic to the lattice and less dependent upon extrinsic effects such as domain wall motion than piezoelectricity. Such thin films offer significant advantages in terms of mass producibility, integration with other microelectronic devices, and lower processing costs. The lower heat capacity of thin films compared to their bulk counterparts improves the time response and sensitivity of the pyroelectric devices because a larger temperature rise is achieved for given IR flux, thereby resulting in larger spontaneous voltage. Furthermore, it is possible to operate thin films (as dielectric bolometers) at high bias fields due to their relatively higher dielectric breakdown strengths and coercive fields.[203–206]

In order to integrate FE films into standard silicon-based integrated devices, the selected synthesis method through which the pyroelectric films are deposited should be compatible with conventional integrated circuitry (IC) as a post process, which means depositing the films below 500°C.[207,208] While there have been significant advances in industry-standard thin film growth techniques such as *rf*-sputtering, metal-organic chemical vapor deposition (MOCVD), and metal-organic solution deposition (MOSD); IC compatibility and cost considerations require that these films be deposited onto fully processed and metallized Si as end-of-line processes. This restriction may give rise to substantial material performance problems due to the relatively large CTE

mismatch between a typical perovskite pyroelectric and Si. For example, in-plane thermal strains from the CTE difference may lead to cracking or delamination. In addition, excessively high post-processing temperatures for too long a period of time may degrade the aluminum metallization, or result in doping migration in the active silicon layers. The choice of temperature-time budget for the PZT annealing step in the fabrication of fully-integrated pyroelectric arrays thus requires some care, but it is feasible and fully working sol-gel fabricated integrated pyroelectric arrays have been demonstrated.[203] The typical room temperature pyroelectric coefficients of polycrystalline PZT thin films on Si or metallized Si substrates for Ti-rich compositions are summarized in Table 4.[203,209–222] Specific details corresponding to the Ti composition, synthesis method, processing temperatures, film thickness, and texture are provided in this summary. Table 4 shows that PZT 30:70 films that have a predominantly (111) texture yield the highest pyroelectric coefficients corresponding to ~0.02 $\mu Ccm^{-2}°C^{-1}$.[202,203,217]

Table 4. Summary of pyroelectric properties of typical polycrystalline PZT thin films on Si substrates (Ti-rich compositions). Also included in the list are the deposition method, deposition parameters, texture, and film thickness.[223]

Compo-sition (Zr/Ti)	**Orientation / Texture**	**Substrate**	**Method**	**Processing Temperature (°C)**	**Pyroelectric coefficient ($\mu Ccm^{-2}°C^{-1}$)**	**Thick-ness (nm)**	**Ref.**
30/70	Highly (111)	Si/Ti/Pt	Sol-gel	510	0.030	1000	203
30/70				≈500-510	0.020-0.029		
25/75				510	0.022		
20/80				510	0.018		
15/85	(111) – 80%	Si/Ti/Pt	Sol-gel	580-650	0.022	1000	209
	(100) – 48%				0.019		
25/75	(111)	Si/Ti/Pt	Sputtering	450	0.020	400-1000	210,211
30/70	Highly (111)	Si/Ti/Pt	Sol-gel	530	0.021	700	212
30/70	Random	Si/Ti/Pt	Sol-gel	650	0.001 *@50°C*	500	213
30/70	Random	Si/Ti/Pt	Sol-gel	600	0.040	550	214

40/60	(110) – 93%	Si/LNO/Pt	Sputtering	650	0.078 (avg.) 0.109 (max.)	500	[215]
30/70	Random	Si/Ti/Pt	Sol-gel	600	0.025	550	[216]
30/70	Highly (111)	Si/Ti/Pt	Sol-gel	480	0.018	800	[217]
30/70	Random	Si/Ti/Pt	Sol-gel	640	0.029	450	[218]
30/70	(100)/(111)	Si/Ti/Pt	Sol-gel	530 or 560	0.032	1000	[219]
30/70	Random	Si/Ti/Pt	Sol-gel	560-700	0.010-0.017	450	[220]
30/70	N/A	Si/Ti/Pt	Sol-gel	650	0.018 @ *260°C*	N/A	[221]
25/75	(100)/(111)	Si/Ti/Pt	Sol-gel	750	0.021	N/A	[222]
	(111)		Sputtering	600	0.020		

The total polarization (spontaneous and induced) and its temperature dependence, defined through the pyroelectric coefficients, are intimately coupled with internal strains within the materials.[186,204] As such, the electrical and mechanical boundary conditions are determined by the choice of a particular pyroelectric material, the substrate, the electrode configuration (top and bottom electrodes in a planar configuration or interdigitated electrodes), and processing conditions. There have been numerous theoretical and experimental studies that demonstrate the impact of residual strains which may result in deleterious effects on the FE thin film properties.[56,198,199,224–227] Prior work also shows that the pyroelectric properties of FE thin films can be optimized through engineering misfit and thermal strains.[186,204,228,229] For example, theoretical studies of BST films on Si and sapphire substrates indicate that the pyroelectric response of these films may vary with film composition, the substrate material, and the processing temperature.[183,204]

3.2 Monodomain Single Layer Thin Films

In this section, the pyroelectric properties of PZT films on Si are investigated before discussing the properties of multilayers. The effect of thermal strains, film texture and film composition on the pyroelectric properties are discussed.

Figure 6 shows the temperature dependent out-of-plane polarization of polycrystalline bulk PZT. Bulk PZT is chosen as the reference for comparing the properties of PZT thin films. PZT 40/60 and 30/70 exhibit second order phase transitions as dictated by the positive signs of the quartic dielectric stiffness coefficients. Conversely, the order of the phase transition changes for high Ti compositions (PZT 20/80, PZT 10/90, PZT 0/100). It is also seen that increasing the Ti composition enhances the polarization and shifts the phase transition to higher temperatures, for the case of single domain state films. Strain-induced shifts in the phase transition temperature of FEs have been determined theoretically and experimentally.[19,183,199,230] The polarizations of (001)-textured PZT films on Si as a function of temperature are plotted in Figure 6(b) at a T_G of 550°C. From Figure 6(b), the phase transitions of PZT films shift to lower temperatures compared to their bulk counterparts and become second order for all compositions due to modification of the quadratic dielectric stiffness coefficient as given through Equation 17. Such shifts have also been predicted via phase field models.[168] The thermal strains are tensile in nature, since the CTE of PZT films are higher than Si for all compositions in the temperature range (25-800°C) investigated in this study. Thermally-induced tensile strains couple with polarization and suppress it by counteracting to some extent the electrical dipole separation in the PZT films.

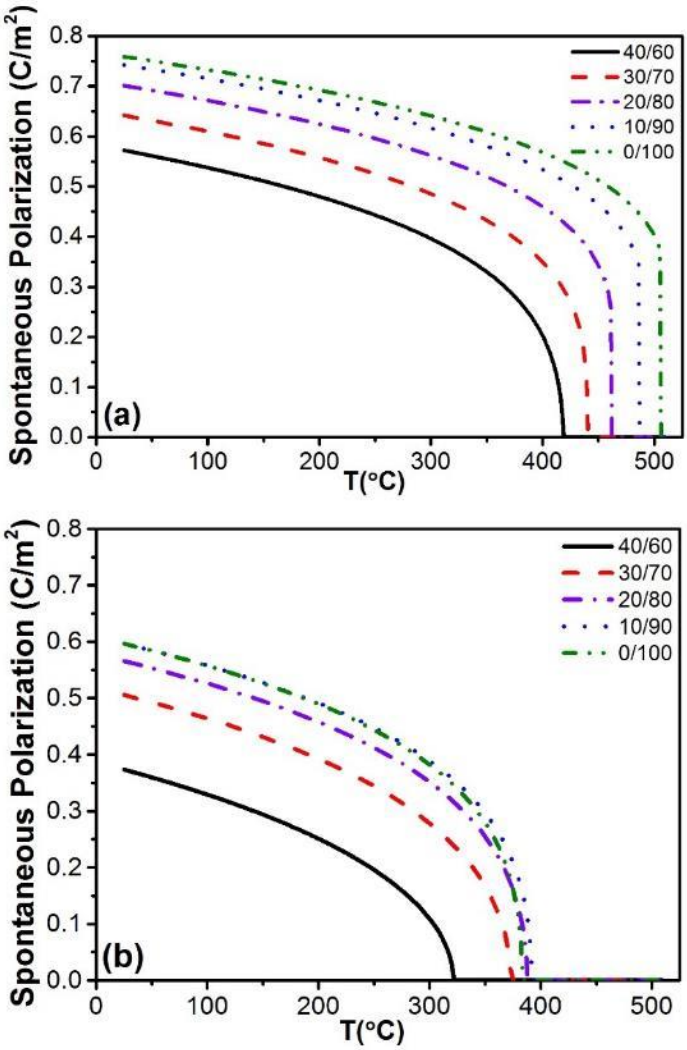

Figure 6. Temperature dependent polarization of (a) bulk, polycrystalline PZT and (b) (001)-textured PZT on Si (T_G=550°C) at various compositions.[185]

While the pyroelectric coefficient is the slope of the spontaneous polarization with temperature when operating significantly below the Curie temperature, a large absolute value of the polarization is also required to achieve good signal to noise in the readout IC of an IR focal plane array (FPA). As seen from Table 4, the processing temperature of PZT films on Si is reported to be roughly in the range between 500-750°C. Therefore, the behavior of the polarization must be investigated over a wider temperature range in order to fully elucidate the effects of thermal strain.

Figure 7 plots the [001] polarization of PZT films on Si as a function of T_G in 25-800°C range. As expected, the spontaneous polarization is greater for lead titanate (PZT 0:100, PT) films compared to other PZT compositions. The TEC mismatch between the film and the substrate is more pronounced as the Ti composition is increased and reaches a maximum for PT films. Accordingly, the polarization drops more drastically for PT with increasing T_G (i.e. the slope of P vs. T_G) due to a build-up of a larger amount of tensile strain. On the other hand, polarization of PZT 40/60 films is found to be even more sensitive to T_G although it has the lowest TEC among the films; a fact that can be attributed to the closer proximity of its T_C to RT [Figure 6(b)]. Consequently, it is important to note that the polarization of PZT films depends on the complex interplay between T_G and the film composition; both of which determine the magnitude of tensile strains and the phase transformation temperature.

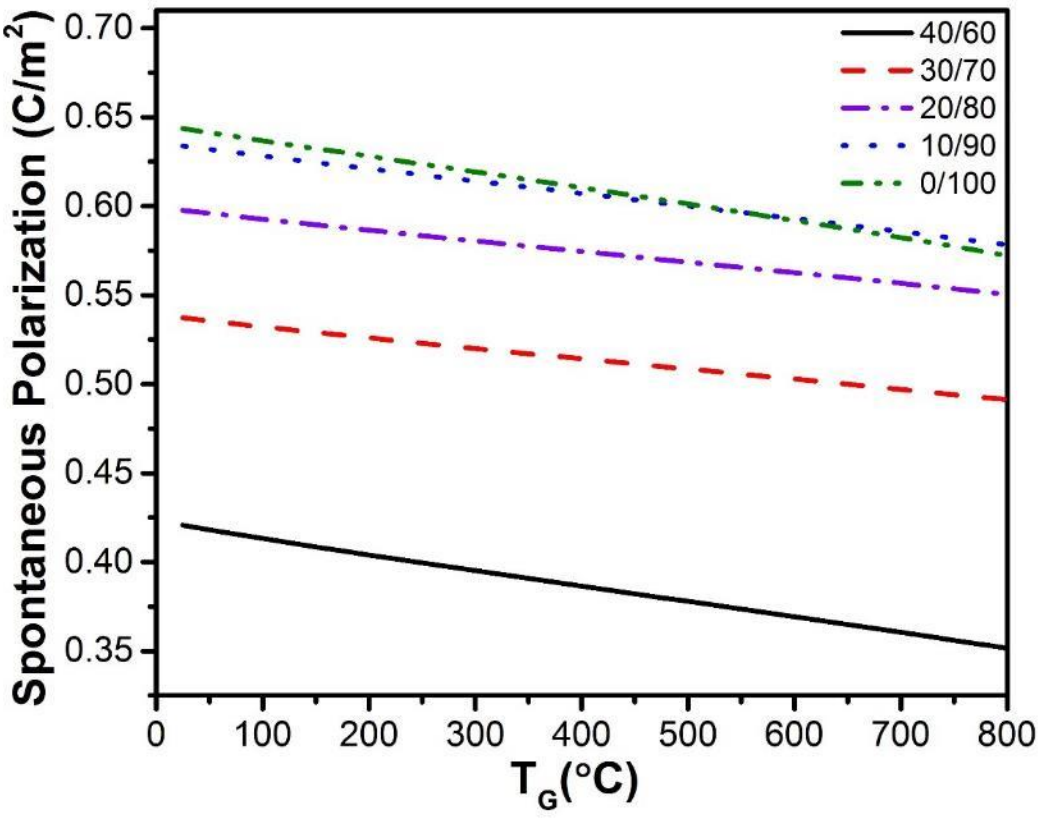

Figure 7. [001] polarization of PZT thin films with different Ti composition as a function of the processing temperature.[185]

The effects of thermal stresses on the RT pyroelectric properties of PZT thin films on Si as a function of T_G are illustrated in Figure 8. The bulk values of PZT for the same compositions under zero bias fields are also indicated for comparison. Bulk single-domain PZT 40/60 has the highest pyroelectric coefficient (0.042 μCcm^{-2}°C^{-1}); with an increase in Ti composition producing a deleterious effect on pyroelectric properties. On the other hand, for PZT thin films, there is also a composition (PZT 30/70) wherein a comparable pyroelectric response is observed. This latter composition is attractive in that it offers nearly a 20% larger spontaneous polarization compared to the 40/60 composition. Figure 8 also reveals that it is possible to improve upon the pyroelectric performance of bulk which has been reported for FE films and heterostructures in previous

studies.[183,231–233] The high pyroelectric response of the PZT 30/70 can be explained because the phase transformation temperature is sufficiently remote from RT to achieve a relatively large polarization, yet at the same time close enough to allow substantial polarization change with temperature. We note that experimentally PZT films on Si substrates contain polydomain microstructures that form so as to relax thermal stresses due to the TEC mismatch and the transformational stresses due to the FE-PE phase transformation at T_C.[23,234–240] Several studies have been reported which provide a rigorous analysis of polydomain heterostructures in epitaxial FEs taking into account these (volumetric) sources of internal stresses as well as localized strain fields near defects using thermodynamic models and phase-field approaches.[168,224,241,242] Therefore, to describe the experimental observations, more sophisticated models need to be developed to describe the effect of grain and domain boundaries, grain texture, and the extrinsic contribution to the pyroelectric coefficient resulting from reversible domain wall motion.

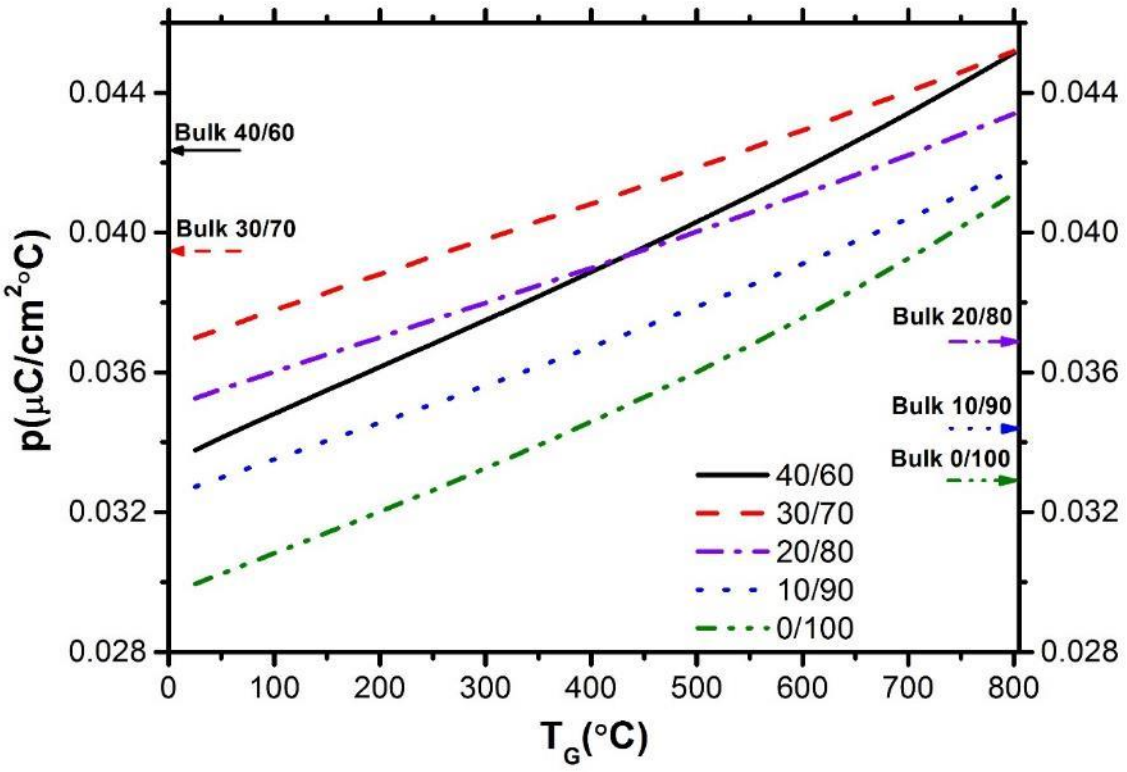

Figure 8. Pyroelectric coefficients of PZT thin films on Si for five compositions as a function of the processing temperature. The arrows indicate pyroelectric coefficients of bulk PZT under zero bias field.[185]

The effect of a biasing electric field on pyroelectric coefficient of PZT films grown on Si at 550°C is demonstrated in Figure 9. An externally applied electrical field normal to the film/ substrate interface changes the free energy density as defined through Equation 8. The applied electric field smears the phase transformation at T_C, thereby reducing the slope of the polarization vs. temperature curve and hence the pyroelectric response. A summary of our findings is illustrated in Figure 10 for PZT films on Si processed at 400, 550, and 700°C respectively. These temperatures were selected because they represent the typical minimum and typical maximum processing temperatures thus covering the whole processing temperature range reported in the literature (Table 4). Regardless of the electric field strength (50-200 kV/cm), PZT 30/70 films have

the highest $|p|$ with the pyroelectric properties of PZT films optimized by controlling both T_G and the Ti composition.

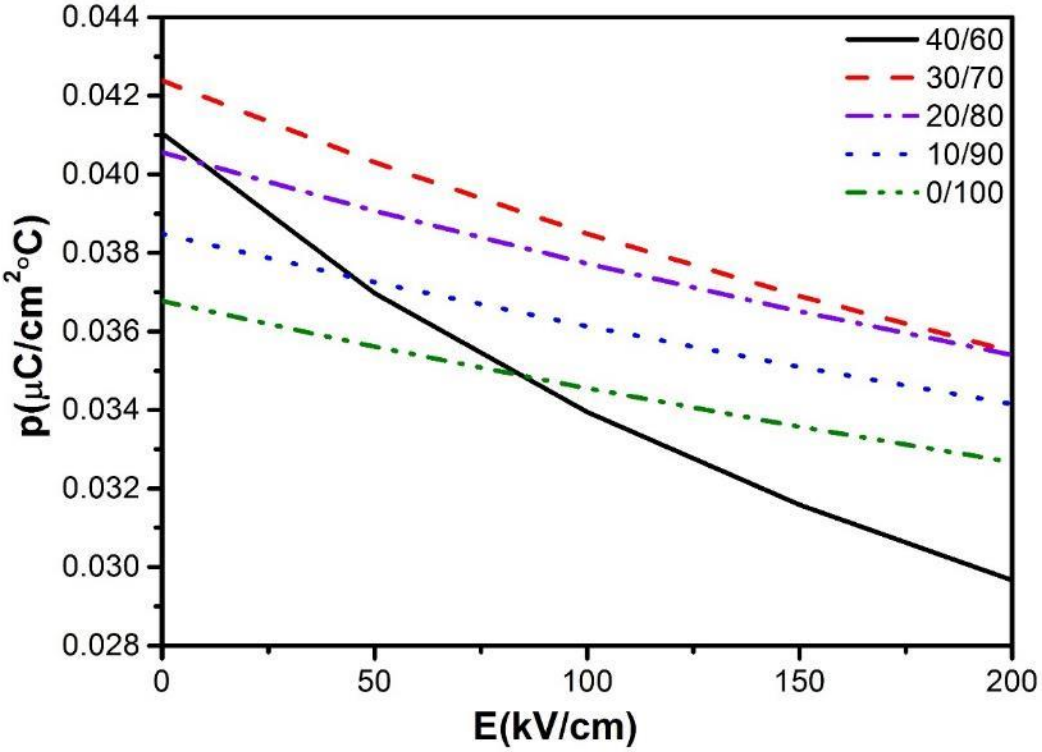

Figure 9. Pyroelectric coefficients of (001)-textured polycrystalline PZT films (T_G=550°C) for five compositions as a function of the applied bias field.[185]

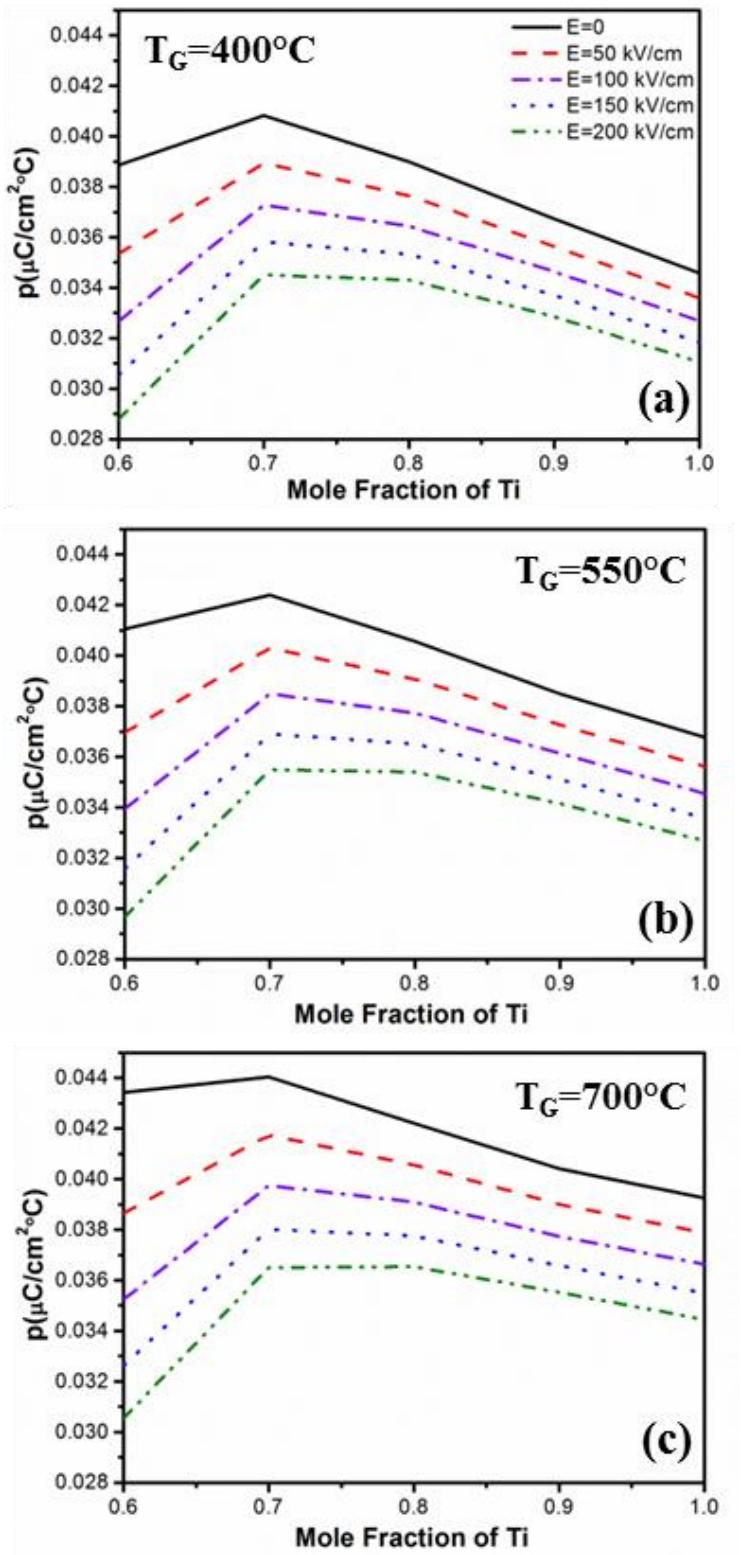

Figure 10. Pyroelectric coefficient of PZT thin films on Si grown/processed at (a) 400°C, (b) 550°C and (c) 700°C as functions of Ti composition and the applied electric fields.[185]

The calculated RT pyroelectric coefficient for PZT 30/70 grown at 550°C under zero electrical field is approximately 0.04 $\mu Ccm^{-2}{}^{\circ}C^{-1}$; almost two times larger than for PZT films of other composition processed around the same temperature. It should be emphasized that the result of the calculations presented herein is for the films which are assumed to be perfectly (001)-textured. In addition, many IR FPAs have partially released air bridge structures which partially diminish the effects of in-plane strains. Lastly, many films grown on platinized Si substrates with titanium adhesion layers adopt a highly textured (111) orientation.[203] In other words, the polarization and pyroelectric vector components are along [111] and therefore, lower than the maximum allowable values obtained from [001].[203,209,217,227,243–246] In order to assess the contribution of [111]-aligned dipoles in our analysis, as a first-order approximation, the calculated polarization values and pyroelectric coefficients can be normalized by $1/\sqrt{3}$ to account for geometrical considerations.[209,247] This simple assumption decreases the computed pyroelectric coefficient to ~0.02 $\mu C\ cm^{-2}{}^{\circ}\ C^{-1}$ in agreement with the experimental findings of (111)-textured films listed in Table 4. However, to fully describe the polarization along [111] with biaxial in-plane strain as defined in Section 2.3, a more complicated thermodynamic analysis taking into account the anisotropic nature of the mechanical boundary conditions has to be employed.[239,248] It is also obvious that it is necessary to find synthesis routes that will result in [001] oriented PZT films on Si to maximize the pyroelectric response.

3.3 Pyroelectric Properties of Ferroelectric-Dielectric Multilayers

It has been shown experimentally that adding a linear DE buffer layer will improve leakage and loss characteristics of ferroelectric devices under high field.[249–252] For example, $Ba_xSr_{1-x}TiO_3$ (BST) films grown on sapphire with a 9 nm $SrTiO_3$ (STO) buffer layer has a lower leakage current (~$1x10^{-8}$ A/cm^2 at 0 V) compared to a BST monolayer with no buffer layer (~$1x10^{-7}$ $A\ cm^{-2}$ at 0

V).[253] These and other reports motivate investigation of the consequences of interposing a high quality DE (e.g., Si_3N_4, or similar) between a material of lesser breakdown strength and the electrodes to make a multilayer.[254] However, the dielectric properties of such a multilayer will depend strongly upon the material with the smaller relative permittivity. Here, the pyroelectric properties of $PbZr_{0.2}Ti_{0.8}O_3$ [PZT(20/80)] as a prototypical FE and various DE buffer layers including alumina (Al_2O_3), silica (SiO_2), silicon nitride (Si_3N_4), hafnia (HfO_2), and titania (TiO_2) are investigated using the formalism laid out in Sec. 2.2. The dielectric stiffness coefficients, elastic compliances and CTEs of PZT and Si can be found in Ref.[255]

Figure 11(a) shows the schematic of the PZT-DE system considered in current analysis. Figure 11(b) shows the average out of plane polarization of PZT 20/80 films for T_G=550°C as a function of Al_2O_3 layer fraction on metallized Si. The net polarization decreases rapidly with increasing thickness Al_2O_3 due to the large polarization mismatch between the FE and DE layer. Specifically, at a critical DE thickness of only ~2% of the PZT, P_S vanishes in the absence of a bias field. Application of an electric field to compensate for the polarization decay shifts the critical thickness to a larger value. Conversely, ε_R and p of the composite structure gradually increases with increasing Al_2O_3 layer fraction as can be seen in Figures 11(c) and 8(d). This seemingly counterintuitive finding is due to the electrostatic coupling between layers and a shift in the Curie temperature to lower temperatures as a result of the thermal strain between the FE and the interposed DE layer. A detailed discussion of these two factors is provided in the later parts of the paper. In the example shown in Figure 11, an abrupt change of spontaneous polarization at the critical buffer layer fraction increases ε_R of bulk PZT from 85 to 310 for structures with 1% Al_2O_3 interposed between a platinum coated films clamped on Si substrate with a growth temperature T_G=550°C. Figure 11(d) plots the pyroelectric coefficient of PZT-Al_2O_3 bilayers as a function of the buffer layer fraction. Adding a DE layer to PZT films drastically improves the pyroelectric

properties such that a bilayer composed a PZT film with 1% Al_2O_3 is expected to have a pyroelectric coefficient of 0.070 $\mu Ccm^{-2}°C^{-1}$ which is 80% higher than the value computed for PZT 20/80 monolayer on Si. Calculations for Si_3N_4 as the buffer layer yield similar results. For PZT with T_G=550°C, the critical fraction of Si_3N_4 is 1.75%. This is because the bulk dielectric permittivity of Si_3N_4 and Al_2O_3 are similar (7 and 8, respectively). For a bilayer with Si_3N_4 fraction equal to 1%, ε_R and the pyroelectric coefficients are ~360 and 0.078 $\mu Ccm^{-2}°C^{-1}$. The above findings are consistent with the fact that active electrocaloric and pyroelectric thin film devices often have active FE layer thicknesses of ~1000 nm, whereas the thicknesses necessary to achieve high DE field breakdown strengths in interposed DE layers are often on the order of 1-10 nm, making these results encouraging for the next generation pyroelectric and electrocaloric devices.

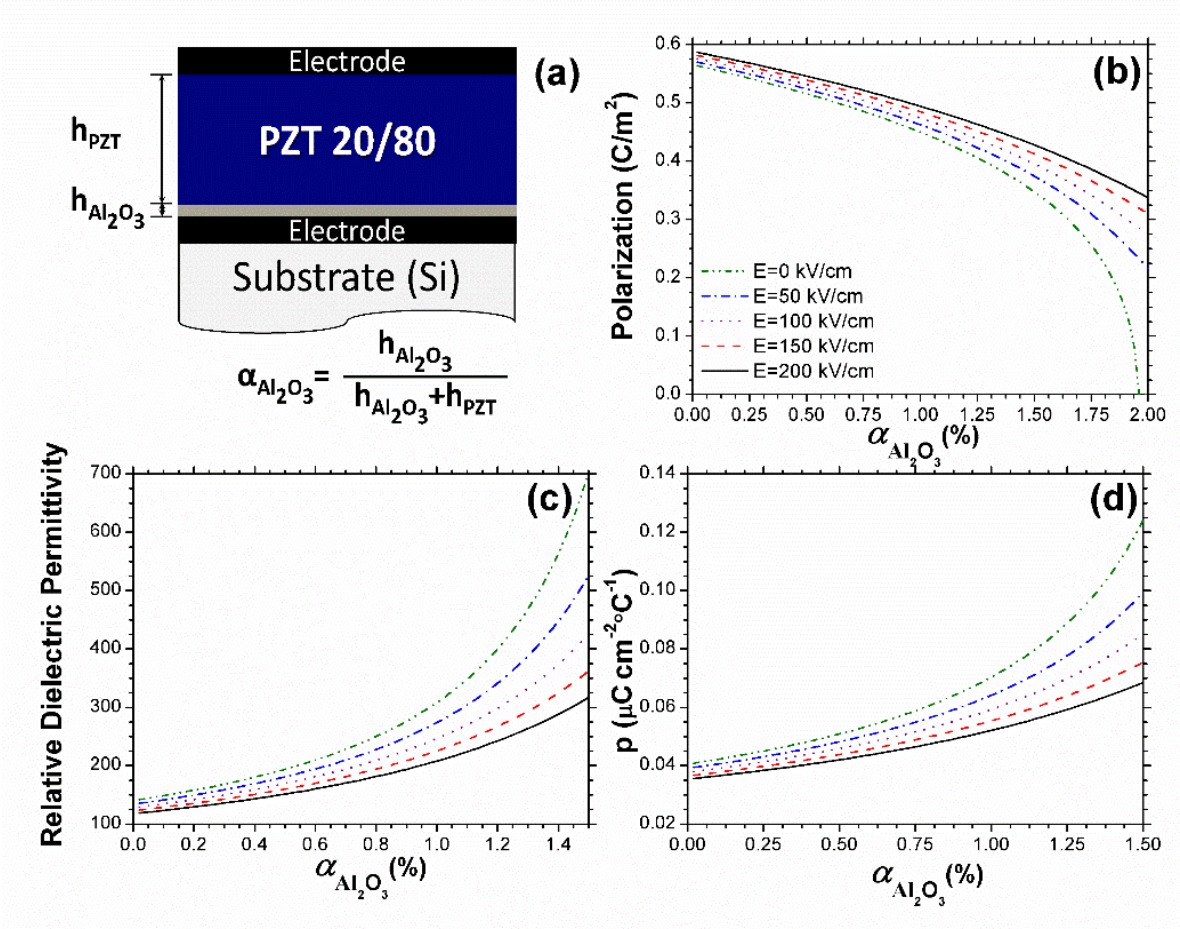

Figure 11. (a) Schematic of a PZT 20/80 film with an Al_2O_3 buffer layer on Si. Room temperature (b) polarization, (c) small signal relative dielectric permittivity, and (d) pyroelectric coefficient curves of PZT 20/80 as a function of Al_2O_3 layer fraction for T_G=550°C on Si for E=0, 50, 100, 150, and 200 kV/cm.[255]

The relationship between the dielectric and pyroelectric properties as a function of the buffer layer fraction for four different DEs is shown in Figure 12. The structure of bilayers with SiO_2, HfO_2 and TiO_2 is identical to the one shown in Figure 11(a). An electrical anomaly can be seen at a critical layer fraction with an increase in both the pyroelectric coefficient and ε_R. For alumina, this critical fraction is about 1.95%. For SiO_2, Si_3N_4, HfO_2 and TiO_2 these layer fractions

are approximately 1.10%, 1.75%, 5.00%, and 20.40%, respectively. As seen, the dielectric properties depend on the layer fraction.

Having a multilayer structure results in disappearance of ferroelectricity at a temperature lower than the bulk transition temperature. A concurrent increase in ε_R and p may not be necessarily desirable in applications that demands high-voltage responsivity. This is usually the case for most large area pyroelectric elements that are used in pyroelectric devices. In addition, the signal-to-noise ratio of the pyroelectric element depends on the dielectric losses.[256,257] However, materials with high pyroelectric coefficients may improve the performance of small pyroelectric detectors operating at relatively high frequencies where a high current responsivity (high-gain) is crucial.[16] The figure of merit depends on the specific application, for instance, whether it is used in solid-state heating/cooling or in IR sensing. Regardless of the application, however, low-loss, low leakage currents, and high breakdown strength are important materials parameters. These cannot be determined from the quasi-static theoretical methodology presented in this study.

The loss of stability of the FE phase originates from the internal fields given in Equations 22-24 that describes the electrostatic coupling between the layers. The presence of depoling fields as a result of a polarization mismatch between the FE and the dielectric layer works against the stability of the FE state in the heterostructure. This, however, should not mean the suppression of ferroelectricity beyond the critical fraction. It can be maintained by the formation of electrical domains or by the transport of charged defects to the interlayer interface to screen the internal electric field resulting from the polarization mismatch between layers.[56,200,258] We also note that the present model does not take into account trapped (bound) charges and interfacial dislocations which may relax internal stresses due to lattice mismatch in epitaxial heterostructures. Furthermore, the interfacial energy due to polarization gradients at the interlayer interface is

neglected in Equation 8 when computing the equilibrium properties of the bilayers. This is a valid assumption if the individual layers that make up the multilayer are thicker than the correlation length of ferroelectricity (~1-10 nm). For ultrathin superlattices the energy of polarization gradient near the interfaces should be included in the free energy function. Regardless of its limitations, the variations of this formalism employed here have been used to explain experimental observations that show anomalies in second-order properties and vanishing polarization at critical layer fractions in a wide variety of FE multilayers and superlattices.[116,119,126,127,253,259,260] As such, this relatively simple model can be utilized to guide experimental work on the design of multilayer heterostructures for pyroelectric applications. Prior investigations by the IC and MEMS community have shown that the dielectric strength of DE films may be increased nearly tenfold by interposing high breakdown strength DEs of 1-10 nm thickness.[254] Such studies, together with the findings of current study suggest that the performance of pyroelectric based energy conversion devices (thermal to electric and electric to thermal) could benefit from this approach as well.

Experimentally, dielectric barrier layers often act to reduce, rather than increase the dielectric permittivity, as might be expected based on simple dielectric mixing rules that do not take into account electrostatic coupling between layers. The FE may form domain structures that do not conform to the implicit assumptions utilized in the thermodynamic modeling described above. Consequently, in order to actively employ the advantages associated with the dielectric buffer layer, it would be necessary to ensure that the film remains polarized out-of-plane. This could be achieved, practically, for example, by utilizing films with large levels of imprint, or by deliberately trapping a large amount of charge at one of the dielectric/metal interfaces.

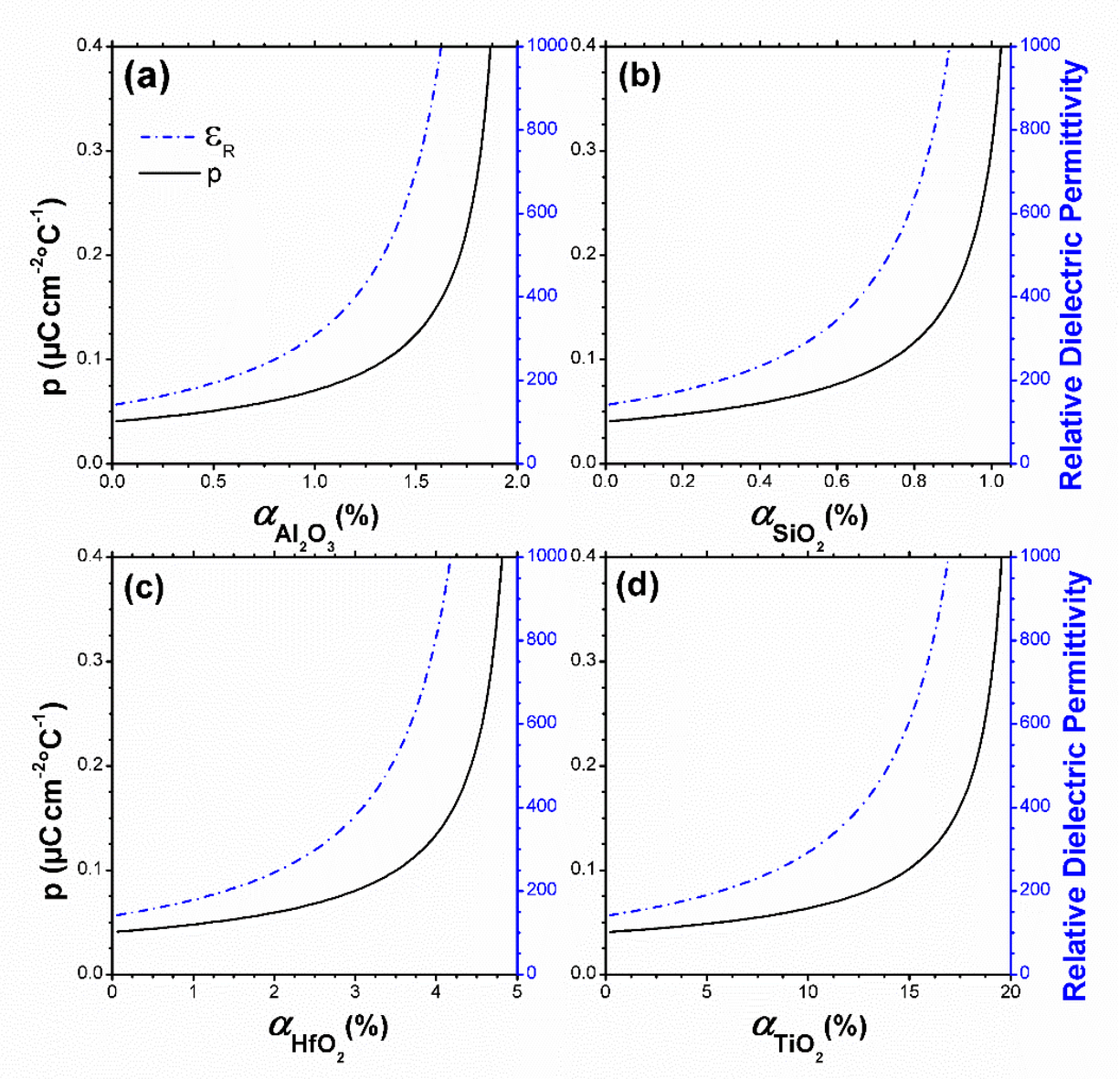

Figure 12. Pyroelectric coefficient and relative dielectric permittivity of PZT 20/80 as a function of (a) Al_2O_3, (b) SiO_2, (c) HfO_2, and (d) TiO_2 layer fractions for T_G=550°C on Si at E=0 kV/cm.[255]

3.4 Pyroelectric Properties of Ferroelectric-Ferroelectric and Ferroelectric-Paraelectric Multilayers

The schematic of the multilayer constructs considered in this section is shown in Figure 13. PZT/BTO and PZT/STO configurations are chosen to investigate the properties of FE-FE and FE-PE multilayers, respectively. Since the polarization values are different for a PE and a FE (polarizability), it is expected that the internal fields in both types of heterostructures is expected to be different and hence the resulting pyroelectric properties. The dielectric stiffness coefficients, elastic compliances and CTEs of BTO, STO, PZT and Si can be found in Ref.[261]

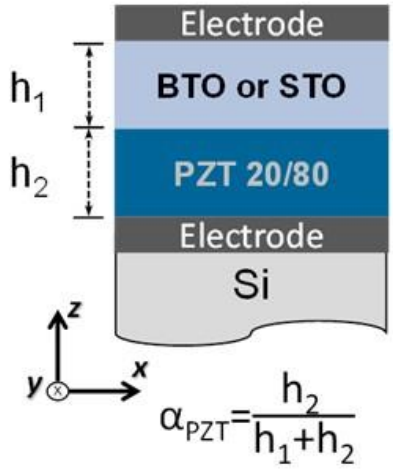

Figure 13. Schematic BTO- and STO-PZT 20/80 bilayers and on a relatively thick Si substrate sandwiched between top and bottom metallic electrodes.

The average out-of-plane polarizations and pyroelectric coefficients of BTO-PZT and STO-PZT multilayers on Si at RT are plotted in Figure 14. T_C of BTO monolayer films (α_{PZT}=0) for T_G=600°C on Si is –101°C, which is 219°C lower than the stress-free bulk value of 120°C. The shift of T_C to lower temperatures is related to in-plane tensile strains that develop during cooling from T_G to RT. Such variations in T_C due to tensile strains have been observed experimentally in

polycrystalline FE films.[19,262–264] Therefore, BTO is in a PE state for T_G=600°C as indicated in Figure 14(a) for α_{PZT}=0. With increasing fraction of PZT in the multilayer construct, electrostatic interactions become sufficiently large to induce FE in both layers. This occurs at a critical PZT layer fraction α_C such that for $\alpha_{PZT}>\alpha_C$, the heterostructure has a non-zero spontaneous polarization, $<P_S>$. On the other hand, the polarization profiles of multilayers made up of STO and PZT look slightly different [Figures 14(c)]. A higher critical PZT layer fraction (α_C=0.65) is required for STO-PZT multilayers compared to BTO-PZT since electrostatic coupling between PZT and STO is weaker. This is because the induced polarization in STO from the internal electrostatic field is smaller due to the relatively smaller dielectric constant of STO compared to BTO. The relative small signal dielectric constants of STO and BTO for thermal strains corresponding to T_G=600°C on Si are 241 and 1270 respectively; hence, $<P>$ of STO-PZT multilayers in the FE state vanishes at a much higher α_{PZT} than BTO-PZT multilayers. In order to obtain a substantial total polarization from STO-PZT heterostructures, PZT-rich multilayer constructs ($0.65<\alpha_{PZT}<1$) should be preferred. Electrostatic interactions also change the phase transition characteristics of the heterostructures by altering T_C of the layers; this is consistent with the discussion above.[265]

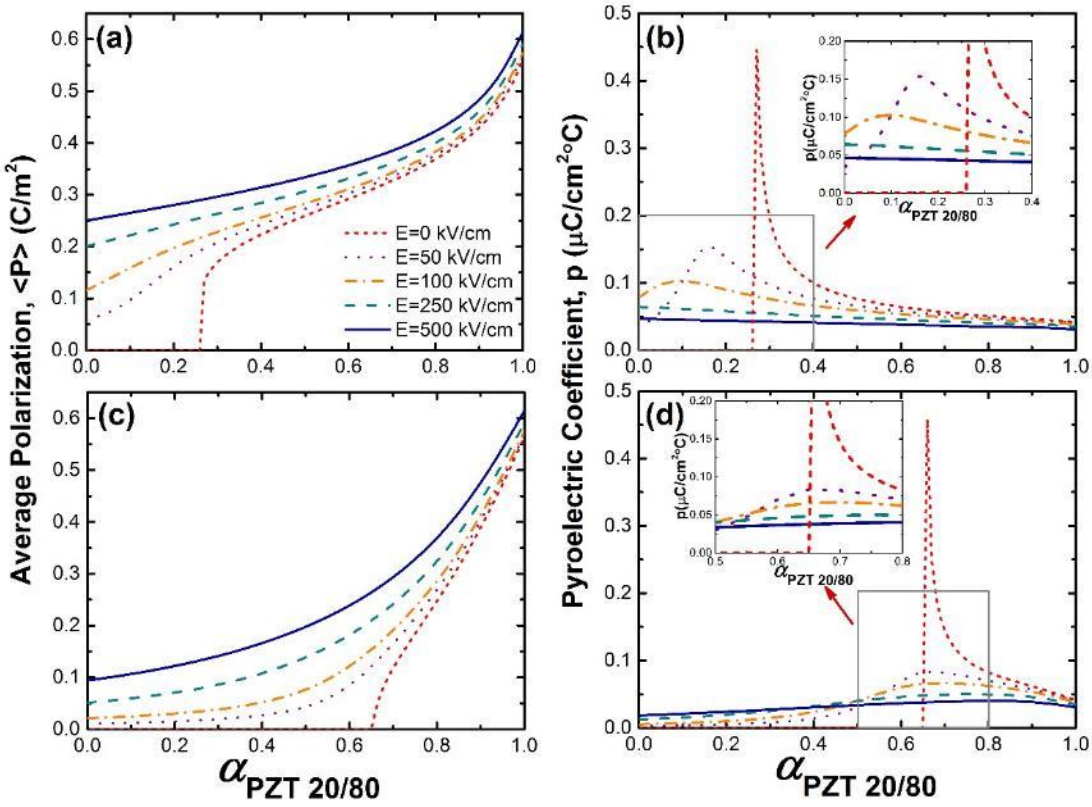

Figure 14. (a) and (c) display the average RT polarization of BTO-PZT 20/80 and STO-PZT 20/80 heterostructures as a function of α_{PZT} and its dependence on applied electric field parallel to the polarization (*z*-) direction. (b) and (d) show the total RT pyroelectric coefficient of heterostructures with polarizations given in (a) and (c). T_G was taken to be 600°C in these calculations. The insets to (b) and (d) illustrate the pyroelectric response in the vicinity of the polarization anomaly. There is a significant enhancement of the pyroelectric coefficient over monolithic PZT.

Electric field dependent RT pyroelectric coefficients of BTO-PZT and STO-PZT multilayers on Si as a function of PZT layer fraction are plotted in Figures 14(b) and 11(d), respectively. Zero field pyroelectric coefficient of both multilayers exhibits a jump near α_C. The pyroelectric coefficients of BTO-PZT and STO-PZT multilayers are ~0.45 μC cm^{-2} $°C^{-1}$ at

α_{PZT}=0.26 and α_{PZT}=0.65, respectively. This value, which is an order of magnitude larger than the pyroelectric response of PZT monolayers on Si (p_{PZT}=0.041 μC cm^{-2} °C^{-1}), clearly indicates a marked improvement in the pyroelectric properties. When multilayers are in a PE state, i.e., $\alpha_{PZT} < \alpha_C$, a pyroelectric response can only be realized under bias. For example, the pyroelectric coefficient of 0.84×BTO-0.16×PZT multilayers under 50 kV cm^{-1} bias is 0.15 μC cm^{-2} °C^{-1}, see inset in Figure 14(b). This value is significantly larger than the pyroelectric response of monolithic BTO and PZT on Si (at 50 kV/cm, p_{BTO}=0.035 μC cm^{-2} °C^{-1}and p_{PZT}=0.038 μC cm^{-2} °C^{-1}). Another interesting feature for BTO-PZT multilayers is that the anomaly at α_C is shifted to lower numbers with a broadened pyroelectric response under moderate fields (0-100 kV/cm). These calculations suggest that if the pyroelectric detector is designed to work in the bolometer mode, the layer fraction of PZT can be adjusted for a specific operating field in the low field regime (0-100 kV/cm) to optimize pyroelectric properties.

As shown, RT pyroelectric properties of PZT-based multilayers on Si can be tailored depending on the choice of the mating layer and the PZT layer fraction. The key observation of this is how the multilayer structure/geometry, in particular the role of electrostatic interactions between the FE and PE layers, can influence the phase transition characteristics driving enhanced thermal and electrical susceptibility of the composite structure. Based on this insight, the BTO-PZT system may be a good candidate material for IR applications, since the multilayers can operate with or without a bias depending on α_{PZT} with large pyroelectric coefficients.

CHAPTER IV. Dielectric Properties of Polycrystalline Ferroelectrics

4.1 Dielectric Properties: Background Information

Non-linear dielectric materials have been considered as voltage-controlled frequency-agile elements in tunable microwave and millimeter wave devices such as capacitors, phase shifters, resonators and oscillators.[12] FEs such as BST have emerged as leading candidates for such applications due to their highly non-linear dielectric response to an applied electric field, especially in the vicinity of the PE-to-FE phase transformation temperature T_C.[266–269] In BST, T_C can be controlled via the composition. For example, bulk T_C of BST 70/30 ($Ba_{0.70}Sr_{0.30}TiO_3$) is just below room temperature (~15ºC).[266] As such, FEs and, in particular, BST, have been investigated for over a decade as potential candidates in tunable components in telecommunications since the utilization of DC fields for tuning improves the response speed and the power consumption of the device.[270,271] The major challenge in designing materials systems for tunable devices is the simultaneous requirement of high tunability (>40%) over a large temperature interval (-20ºC to +85ºC), and low dielectric losses (between 3.0-4.0 dB in operational bandwidths ranging from several hundred MHz over 30 GHz).[14,272,273] It is usually desired in telecommunication applications that FEs are in a PE state to eliminate losses resulting from polarization switching-induced hysteresis, domain wall contributions, and piezoelectric transformations at microwave frequencies.[273,274] Nevertheless, there are reports of acceptable dielectric properties in the FE state as well.[273–276] Significant efforts have been devoted to maintain high dielectric tunability and to decrease dielectric losses through doping and by constructing a variety of composite structures consisting of FE-PE active materials and heterostructures, low-loss and low leakage oxides and

polymers.[115,265,277–280] The dielectric properties of such heterostructures are investigated in the following sections.

4.2 Dielectric Response of Ferroelectric-Paraelectric Multilayer Films

A FE-PE multilayer configuration is chosen for investigation of the dielectric properties of heterostructures. BST, BTO and PZT are considered as FE layers, whereas STO is assumed to be the mating layer. The structure of the multilayers is identical to the one illustrated in Figure 13. A freestanding multilayer (film without any substrate, bulk) configuration is chosen as the reference state to understand the role of two-dimensional clamping and thermal stresses on the dielectric properties more clearly.

Figures 15 and 16 plot the small signal ε_R of the multilayers with BTO and BST as the FE layers respectively on Si and *c*-sapphire. As shown in Figure 15, RT ε_R of unconstrained (bulk) BST is over 2400, whereas the dielectric response of films with α_{STO}=0.1 on Si and *c*-sapphire for T_G=550°C are 554 and 683, respectively. This is expected since thermally-induced in-plane tensile strains and the interlayer coupling both decrease T_C of the FE in such a multilayer configuration. Therefore, such electrical and mechanical boundary conditions are particularly detrimental for the dielectric response if the FE is already in the PE state as it is the case for BST 60/40 at RT, Figure 15. As T_C moves far below RT in the clamped, in-plane strained condition, an appreciable polarization change cannot be induced upon the application of a biasing field. This is especially critical for films processed at higher T_G's, since the dielectric maximum, corresponding to the FE-PE phase transition, is shifted to lower temperatures. This is clearly observed in Figure 15; a lower T_G results in higher ε_R values on both substrates. For example, if T_G could be decreased from 700°C to 550°C for BST on Si with α_{STO}=0.1, we expect that there will be approximately 24% enhancement in ε_R. Figure 15 also shows that employing STO buffer layers reduces ε_R of the

heterostructure with increasing α_{STO} since ε_R of STO is lower than BST. This decrease is non-linear, clearly highlighting the role of electrostatic coupling between BST 60/40 and STO. For the dielectric properties of BTO monolayers (α_{STO}=0), the choice of the substrate and T_G become more critical (Figure 16). This is entirely due to the shift of the bulk T_C (120°C[281]) to lower temperatures. As an example, changing T_G from 625°C to 475°C for BTO on *c*-sapphire results in a 51°C difference in their transition temperatures ($T_{C,625°C}$=-46°C and $T_{C,475°C}$=+5°C). Very high dielectric permittivity values can be obtained near the instability from BTO on *c*-sapphire at a critical T_G=475°C. Figure 16 also shows that the dielectric anomaly in unconstrained but electrostatically coupled heterostructures disappears if such bilayers are on *c*-sapphire and Si due to the in-plane tensile thermal strains and the clamping effect of the substrate. Even at a low T_G such as 400°C, the magnitude of the thermal strains are sufficient to promote a PE state at RT in the BTO layer on both Si and *c*-sapphire. Therefore, BTO-STO displays similar behavior to BST 60/40-STO multilayers in that overall ε_R deteriorates as with increasing α_{STO} as a result of the shift of T_C with respect to RT.

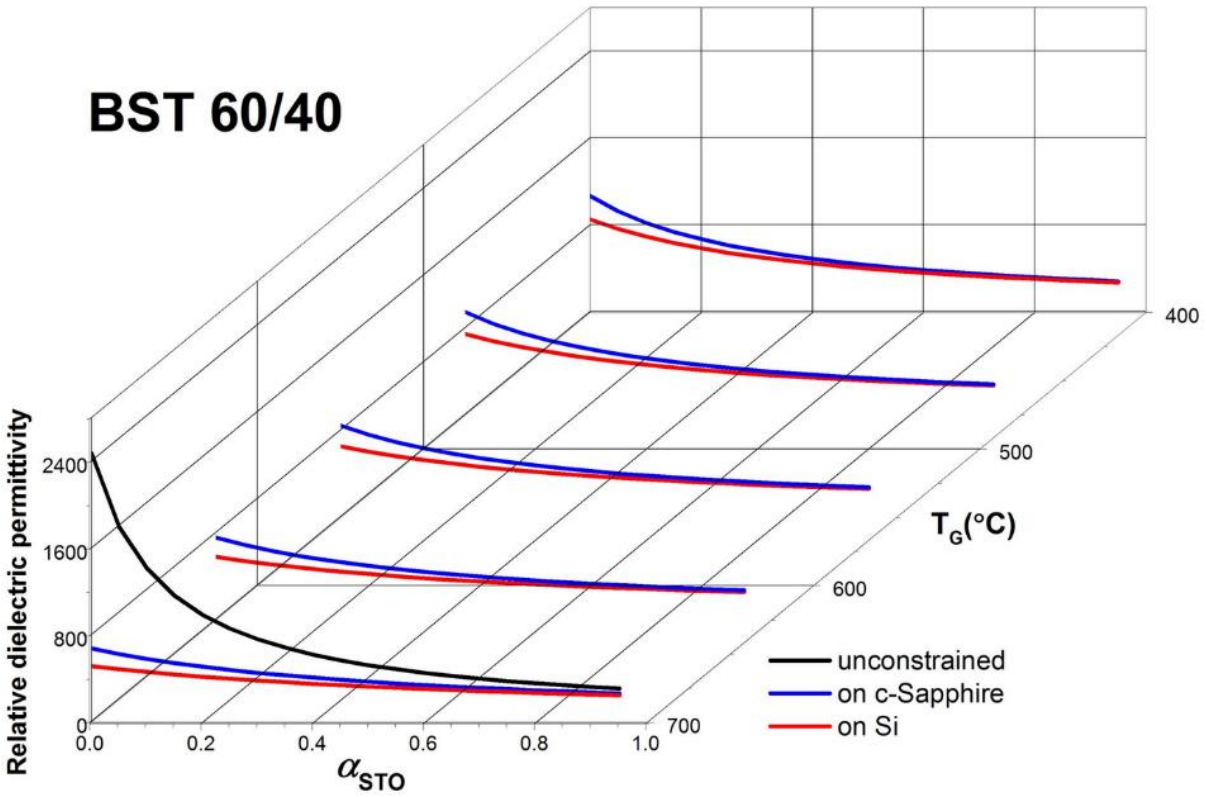

Figure 15. Small signal mean relative dielectric permittivity of polycrystalline BST 60/40-STO multilayer as functions of T_G and STO layer fraction on Si and *c*-sapphire substrates.

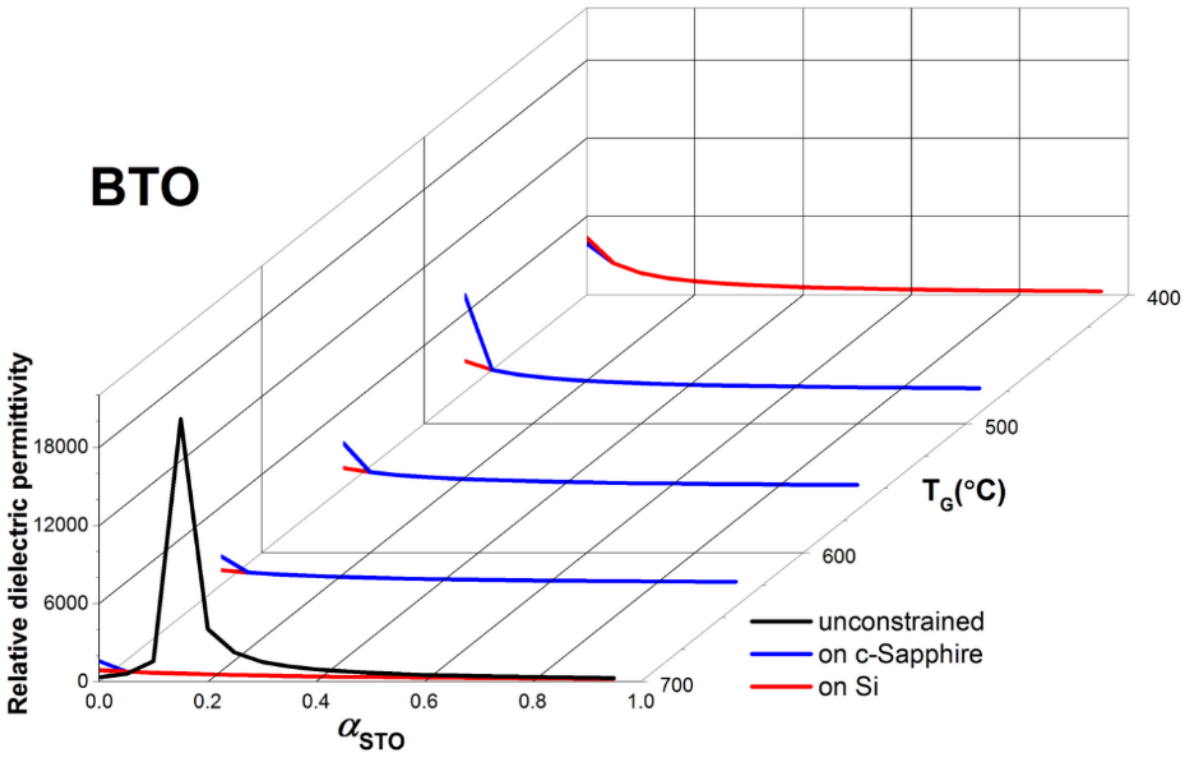

Figure 16. Small signal mean relative dielectric permittivity of polycrystalline BTO-STO multilayer as functions of T_G and STO layer fraction on Si and *c*-sapphire substrates.

Figure 17 plots RT small signal ε_R of PZT 20/80-STO multilayers on Si and *c*-sapphire as a function of T_G and the STO layer fraction. PZT was chosen as the last example in our analysis because its bulk, unconstrained T_C (459°C[187]) is substantially higher than that of BST 60/40 and BTO. The dielectric response of PZT 20/80 as a function of α_{STO} in both unconstrained and thin film configurations exhibits a similar trend for all T_G. The critical α_{STO} varies between 0.2-0.4 depending on T_G. The monotonic decrease in ε_R as a function of α_{STO} shown in Figures 15 and 16 for BST and BTO on Si and *c*-sapphire is not observed for PZT 20/80 on the same substrates. This means that it is feasible to obtain a very strong dielectric response in PZT-STO heterostructures near the instability at a critical α_{STO} that depends on the processing temperature, T_G.

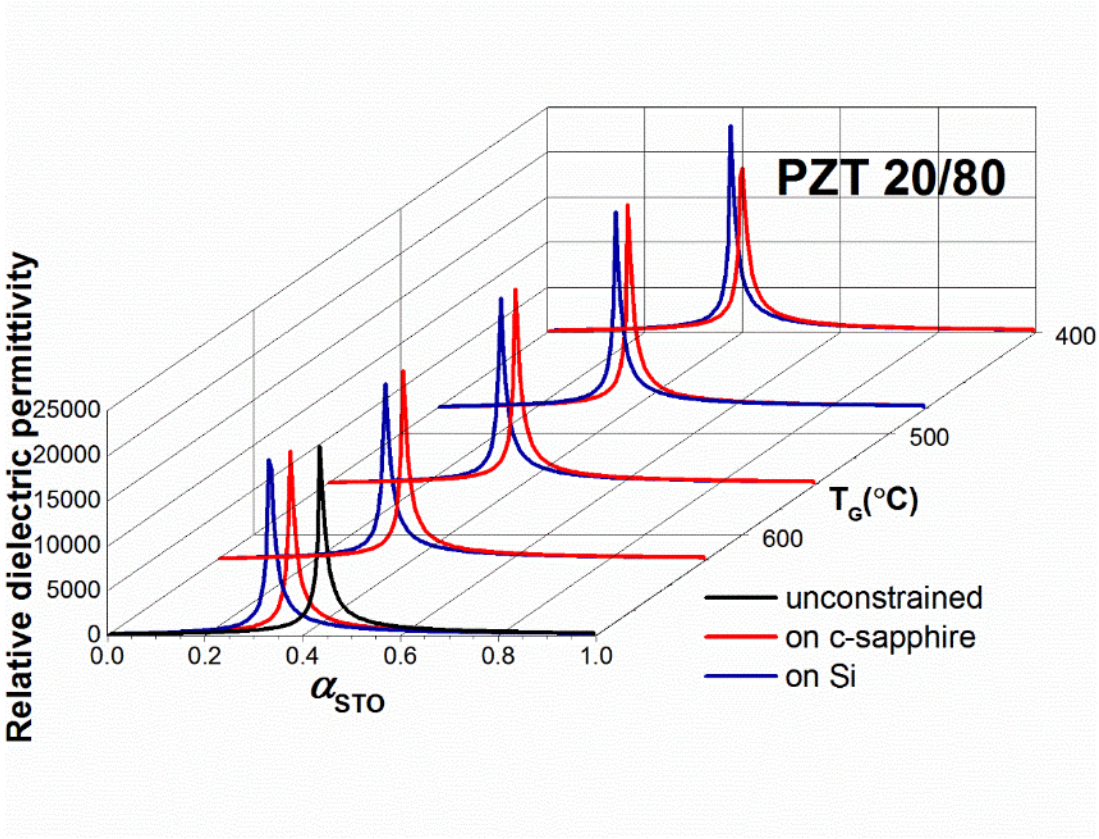

Figure 17. Small signal mean relative dielectric permittivity of polycrystalline PZT 20/80-STO multilayer as functions of T_G and STO layer fraction on Si and *c*-sapphire substrates.

The influence of an applied bias along the *z*-direction on the small signal ε_R and dielectric tunability (η=1-($\varepsilon_{R,E}/\varepsilon_{R,E=0}$)×100, at E=400 kV/cm) of BTO- (α_{STO}=0.1), BST 60/40- (α_{STO}=0.1), and PZT 20/80-STO (α_{STO}=0.35 and 0.40) multilayers on Si and *c*-sapphire for T_G=700°C is illustrated in Figures 18 and 19 respectively. The justification for the selection of α_{STO} follows from Figures 15 and 16. High tunabilities over 60 and 90 % at 400 kV/cm can be realized in BTO- (α_{STO}=0.1) and PZT-STO (α_{STO}=0.35 and 0.4) multilayers respectively at T_G=700°C which is a typical processing temperature for perovskites.

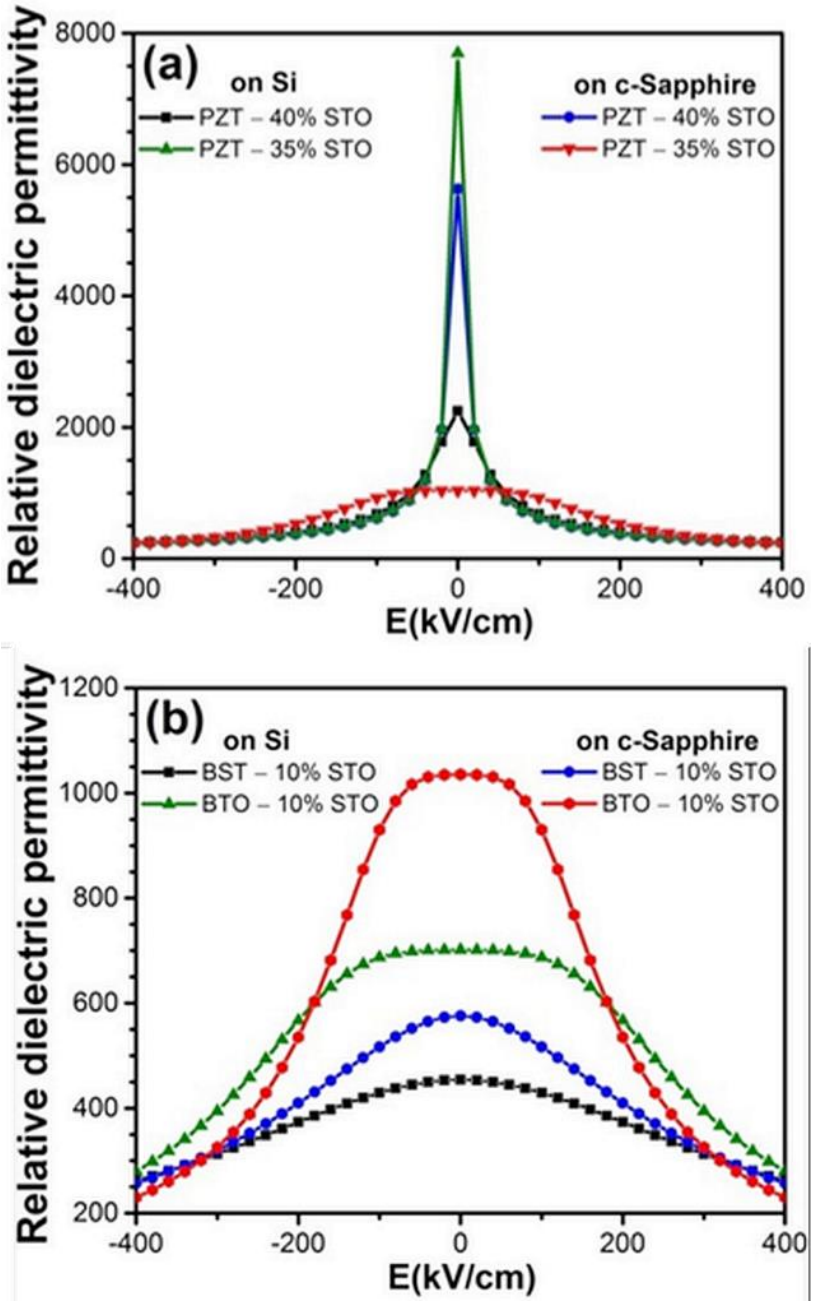

Figure 18. Small signal mean relative dielectric permittivity of (a) PZT 20/80 (for α_{STO}=0.35 and 0.4) and (b) BTO (for α_{STO}=0.1), BST 60/40 (for α_{STO}=0.1) on Si and *c*-sapphire for T_G=700°C.

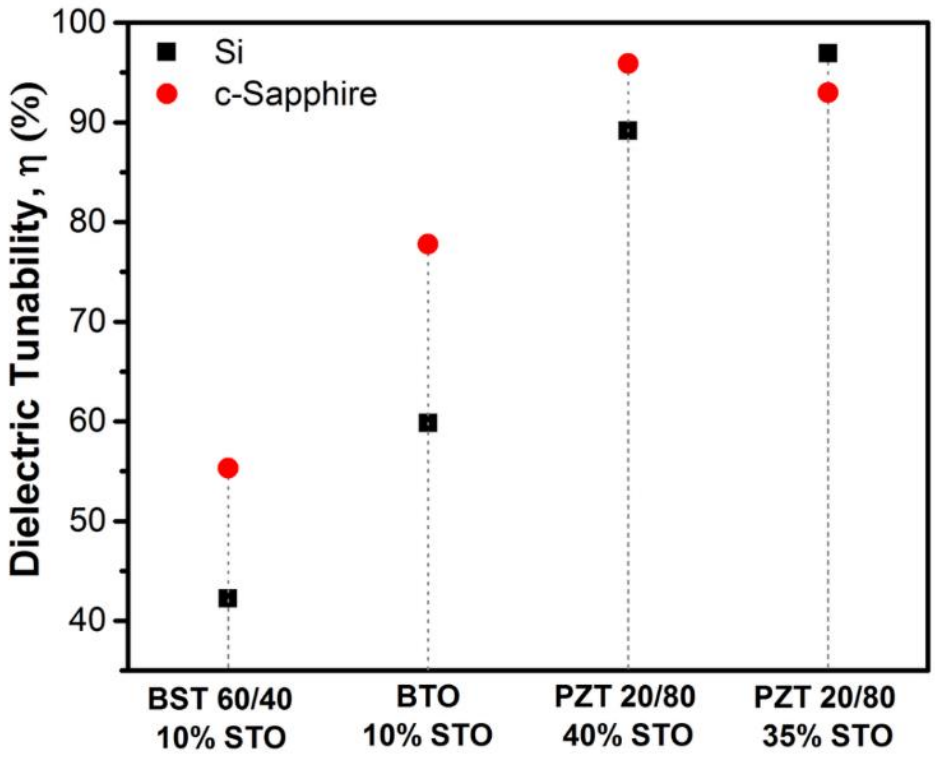

Figure 19. Dielectric tunability of BST 60/40 (for α_{STO}=0.1), BTO (for α_{STO}=0.1), and PZT 20/80 (for α_{STO}=0.35 and 0.4) on Si and *c*-sapphire at E=400 kV/cm for T_G=700°C.

It should be emphasized that introducing STO buffer layers to improve loss and leakage characteristics of BST films decrease their ε_R, as it has been observed experimentally.[260] Therefore, BST or BTO multilayer configurations with thin PE buffer layers on IC compatible substrates should be understood as a compromise between loss and leakage and dielectric permittivity and tunability. On the other hand, PZT-based FE-PE heterostructures offer an opportunity to tailor desired dielectric response near the instability by varying α_{STO} at a given T_G. Although such an enhanced dielectric response is extremely beneficial, as in the case of the BST and BTO multilayer configurations, to be useful in practical tunable device configurations the exceptionally high dielectric response of the PZT-based heterostructure must also be accompanied by low dielectric loss, low leakage current characteristics, and high breakdown field. Nevertheless, the fact the

ferroelectric instability can be tuned as a function of PE buffer layer thickness and process temperatures opens a new region of materials process parameter space to be explored and exploited for voltage-controlled frequency-agile elements in tunable microwave and millimeter wave devices.

CHAPTER V. Electrocaloric Properties of Polycrystalline Thin Films

5.1 Electrocaloric Properties: Background Information

The EC effect is the reversible adiabatic heating/cooling of a system by application/removal of an electric field. It is analogous to magnetocaloric and elastocaloric responses for which the external stimuli to induce a temperature change are magnetic and strain fields, respectively. All caloric properties of ferroic materials are attributed to a change in the entropy density through alignment of dipoles and/or structural alterations on the atomic, molecular, or microstructural level.[17,18,282–284] Electrocaloric materials (ECMs) have been investigated extensively as potential solid state cooling elements in devices with higher efficiency and offering more environmentally-friendly refrigeration compared to existing vapor compression/expansion technology.[282] The EC response and its converse effect pyroelectricity are described by the same property coefficient given in Equation 7. A number of ECMs have been proposed for electrothermal applications, including, but not limited to, FE and anti-ferroelectric ceramics, polymers, and copolymers, in bulk, single crystal, and thin film forms.[18,282,283,285]

Early attempts to investigate the EC effect were made for FE bulk ceramics. The observed adiabatic temperature change ΔT of a couple of degrees is not sufficient for these materials to be utilized in device applications.[285–287] The major obstacle in obtaining high ΔTs from bulk materials is related to the magnitude of electric fields that can be applied and their relatively low dielectric breakdown strength. In 2006, the observation of ΔT~12K at 776 kV/cm from a thin film FE propelled renewed interest in ECMs.[288] Since then, there have been many experimental[288–291] and theoretical[292–295] attempts to investigate the EC effect of thin films. ΔTs as high as 40K have been

reported at large fields exceeding the breakdown strength of bulk materials. Thin films not only permit high fields, but also they can be integrated with microelectronic devices which is promising for the realization of on-chip EC micro-cooling systems. The EC effect can be seen as the inverse pyroelectric effect which is described by the same property coefficient Equation 7. The improvement in pyroelectric properties of multilayers has already been shown in Chapter III. Therefore, it is interesting to see whether such improvements can also be realized for EC properties as well.

5.2 Electrocaloric Response of Ferroelectric-Ferroelectric and Ferroelectric-Paraelectric Multilayer Films

Two specific types of multilayers were investigated for this section; a FE layer (in bulk) is chosen as the mating layer for PZT, whereas a PE layer is coupled with PZT in the second example. Since the latter electrostatic interaction is stronger than the former, the resulting electrothermal response is expected to be quite different as shown in the pyroelectric properties of such heterostructures in Chapter III. Quantitative results are provided and electrothermal properties of multilayers are compared with each other and with respect to PZT monolayers.

The heat capacity of BTO-PZT and STO-PZT bilayers are shown in Figure 20. There is a jump in the heat capacity at the critical layer fraction without an applied field as expected; since the FE state becomes stable in the bilayer as can be seen from Figure 14(a) and 14(c) (Note that the same systems in these figures are also considered in this section). The heat capacity of the bilayers smears out upon applying electric field, hence making the heat capacity less sensitive to changes in the relative amounts of each individual layer. Nevertheless, the heat capacity values of both types of heterostructures are more or less comparable. Lower values of heat capacity are required to obtain a higher adiabatic temperature change from a pyroelectric element. This can

also be seen from the definition of ΔT from Equation 12. The heat capacity can be tailored, for instance by changing the porosity of the pyroelectric element. Reducing the porosity also decreases the heat capacity. However, this limits the maximum value of the driving field because of the reduced dielectric strength of the material.[296]

The RT adiabatic temperature change for BTO-PZT and STO-PZT is plotted in Figure 21 as a function of initial bias field E_a, electric field difference $\Delta E = E_{final} - E_a$, and α_{PZT}. EC effect is more pronounced at higher ΔE as expected, since dipoles are aligned more readily at stronger fields leading to a higher excess entropy density change. As an example, ΔT of 0.35×STO-0.65×PZT for E_a=0 kV/cm is increased almost six times from 0.63°C to 3.17°C with ΔE=500 kV/cm. Although the EC response near the dielectric anomaly slightly deteriorates with an initial bias [E_a=50 kV/cm, Figure 21(b) and 18(d)], it becomes less sensitive to α_{PZT}. Moreover, the peak at α_C is shifted to lower and higher PZT layer fractions for field-driven BTO-PZT and STO-PZT multilayers, respectively, compared to zero field EC response. Figure 21 shows clearly that it is possible to significantly enhance the RT EC properties of PZT by constructing multilayer FE heterostructures. For instance, 0.74×BTO-0.26×PZT and 0.35×STO-0.65×PZT bilayers show ~120% and 65% increase in the EC response, respectively, compared to PZT films on Si (α_{PZT}=1) for ΔE=500 kV/cm and E_a=50 kV/cm.

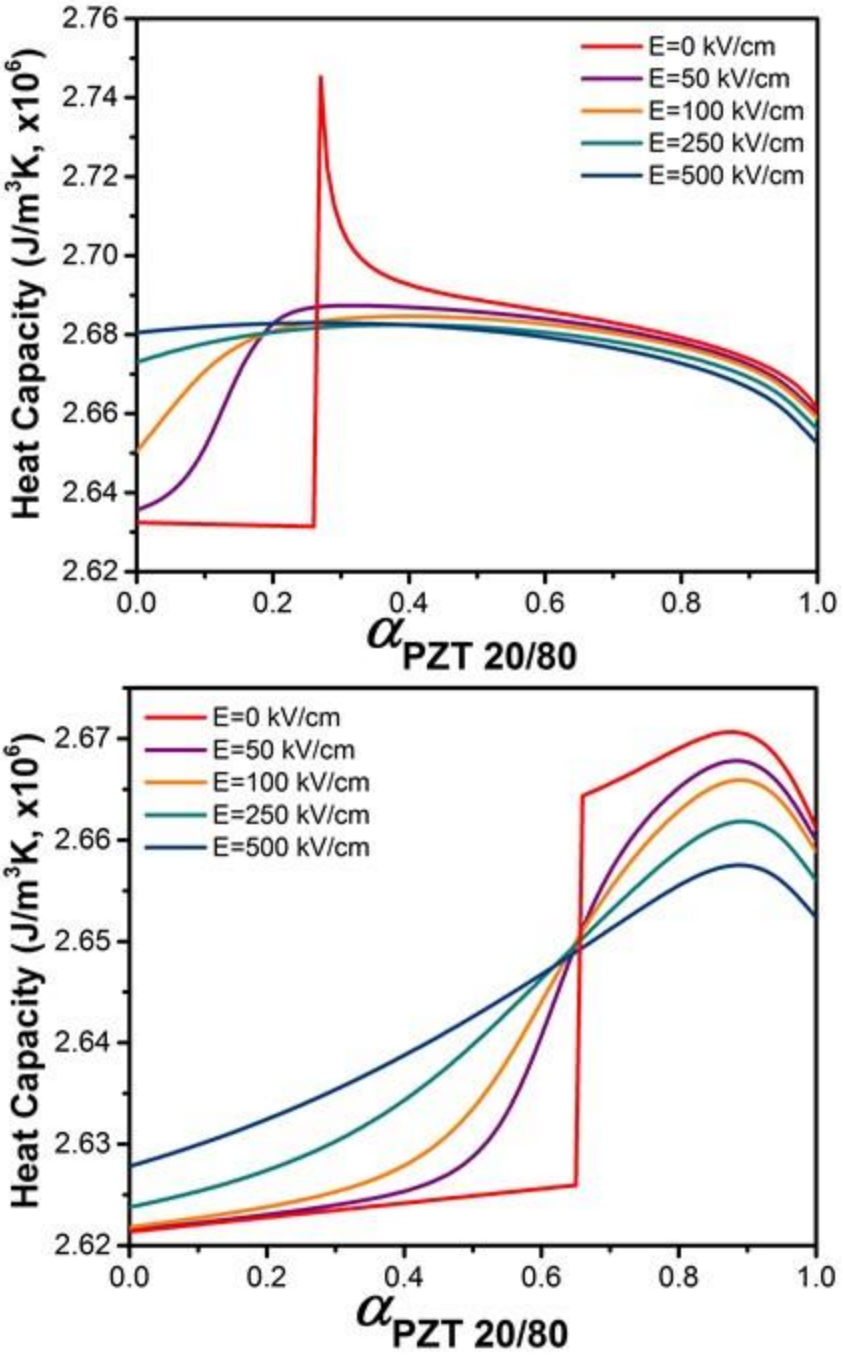

Figure 20. RT heat capacities of (a) BTO-PZT and (b) STO-PZT at different bias field as a function of PZT layer fraction.

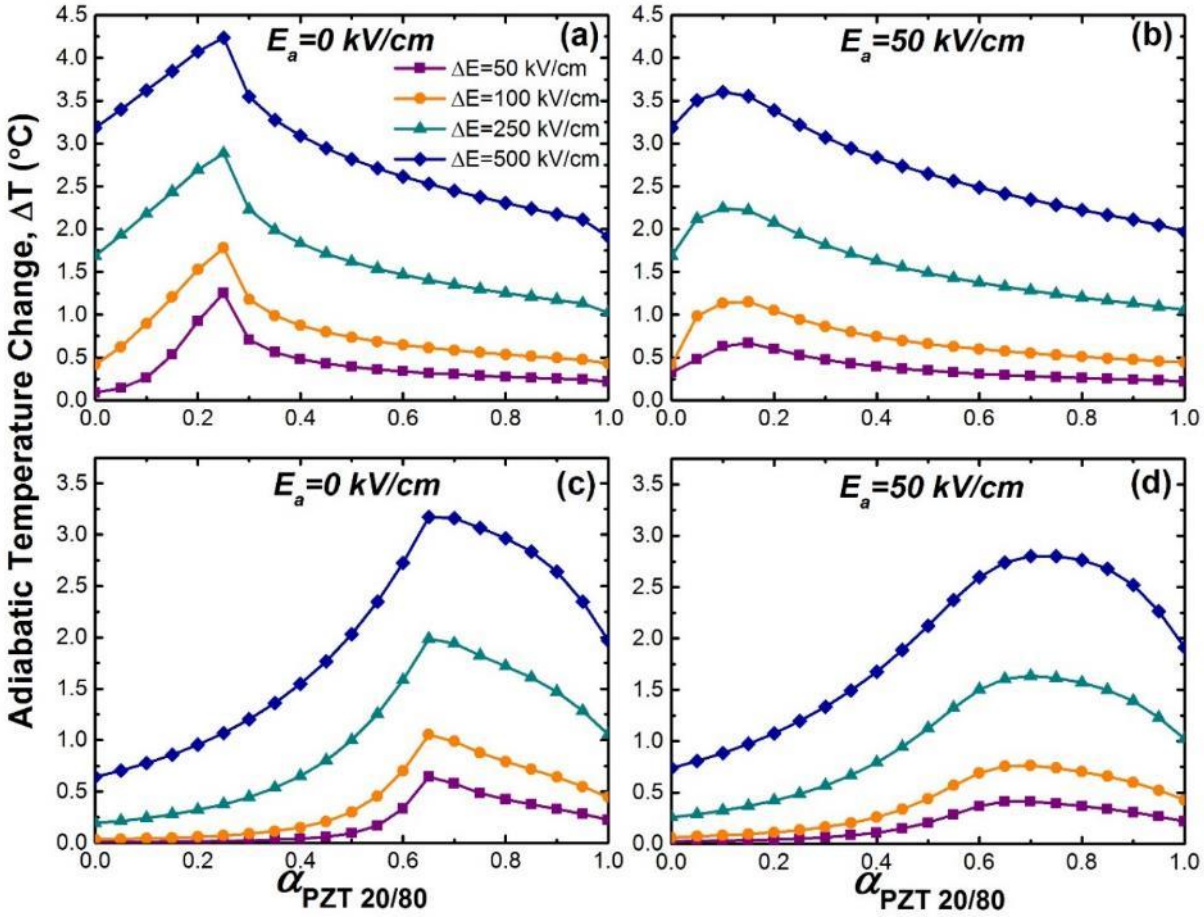

Figure 21. RT adiabatic temperature change of (a) BTO-PZT at E_a=0 kV/cm, (b) BTO-PZT at E_a=50 kV/cm, (c) STO-PZT at E_a=0 kV/cm, and (d) STO-PZT at E_a=50 kV/cm as functions of PZT layer fraction and driving field ΔE.

Chapter VI. Ferroelectricity in Epitaxial Thin film Heterostructures

6.1 Dielectric and Pyroelectric Properties of Ferroelectric Superlattices

The unique properties of FE-based heterostructures have already been discussed in Section 1.3.3. The domain structure and phase transition temperature for a FE-based SL has been shown, both experimentally and theoretically, to depend on total thickness, layer periodicity and layer thickness.[122,297–303] In this chapter, the effects of layer periodicity and thickness on the dielectric and pyroelectric properties of heteroepitaxial (001) PZT (30/70 and 20/80)-(001) STO heterostructures on a STO substrate are presented. The misfit strain for both PZT composition is taken as 1%.

Schematics of the SLs considered here are shown in Figure 22. The first type of heterostructure consist of a PZT-STO bilayer repeating unit [Figure22(a)], whereas the other SL has STO-PZT-STO trilayer repeating unit [Figure22(b)] which, from now on, is referred to as symmetrical unit. The total thickness, L and repeating unit thickness h is fixed for both types of films. $n=L/h$ is the number of repeating units. The LGD formalism presented in Section 2.3.3 is used for the computations on a square grid that has 0.4 nm nodes. λ is taken as infinite to isolate the surface effects. By adopting a finite difference approach, polarization and electrostatic potential is solved using Gauss-Seidel and successive-over-relaxation method, respectively. Electrodes are assumed to be ideal meaning perfect compensation of bound polarization charges. No initial preset domain structure is set so that the system is in a PE state. The epitaxial strain in the SL is assumed to be homogeneous. The effect of strain relaxation in epitaxial FE films through misfit dislocation formation can be investigated using a Landau-based analyses as reported previously.[304,305]

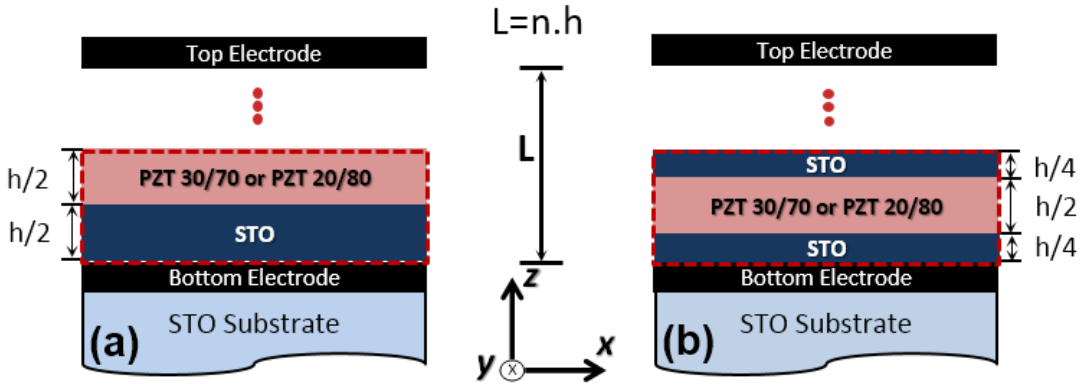

Figure 22. Schematics of heteroepitaxial PZT/STO heterostructures on STO with a (a) bilayer and (b) symmetrical repeating unit. A single unit thickness and total thin film thickness is given by h and L, respectively. Here, n denotes number of repeating units.

6.1.1 Pyroelectric Properties of PZT 20/80-STO Heterostructures

The number of repeating units (n) for the current example is set at 4 and 8 and the total thickness at 72 nm for both types of layers given in Figure 22. So, for the bilayer repeating unit example, each individual layer is 9 and 4.5 nm-thick for heterostructures with 4 and 8 repeating units, respectively. On the other hand, the individual STO layer thickness is halved for the heterostructures that consist of symmetrical units.

$<|P_z|>$ and $<|P_x|>$ (P_z and P_x hereafter) are the absolute average values of total polarization along the z- and x-axes respectively which are plotted in Figures 23 and 24. The absolute values are used since most films are in a multidomain state. The non-zero values of P_x below Tc indicate the generation of closure domains because of electrostatic considerations even if the FE is tetragonal. The starting temperature of strain stabilized P_x can be distinguished with sudden change in the slope of P_x. FE-PE phase transition under low bias (~0 kV/cm) occurs sharply around 700K and 500K for the 4 bilayer unit and the 4 symmetrical unit systems, respectively [Figs. 20(a) and (c)]. 8-unit structures have a lowered and smeared transition even under small bias regardless of

the SL configuration [Figures 23(b) and (d)]. In the 4-unit bilayer and symmetrical unit structures, the transition from the PE to FE state is always into the multidomain (MD) configuration at zero bias. The former develops closure domains right at the transition yielding a relatively small P_x that later suddenly changes slope with cooling as the "strain stabilized" P_x appears in a range of temperatures between 450K and 550K depending on bias [see Figures 24(a) and (c)]. If the SLs transform into a multidomain state, as in the case of 4-unit bilayer structures, external bias reduces the TC of the stacks. In the 4-unit SL consisting of symmetrical units, the MD formation coincides with the appearance of the strain stabilized P_x components. In 8-unit SLs, this point is where the entire film except the FE layer touching the electrode transforms into a closure domain state. Compared to the 4-unit structures, 8-unit structures have lower T_C overall as a result of the reduced layer thicknesses and 1 to 4 orders of lower P_x values suggesting a single domain state in SLs.

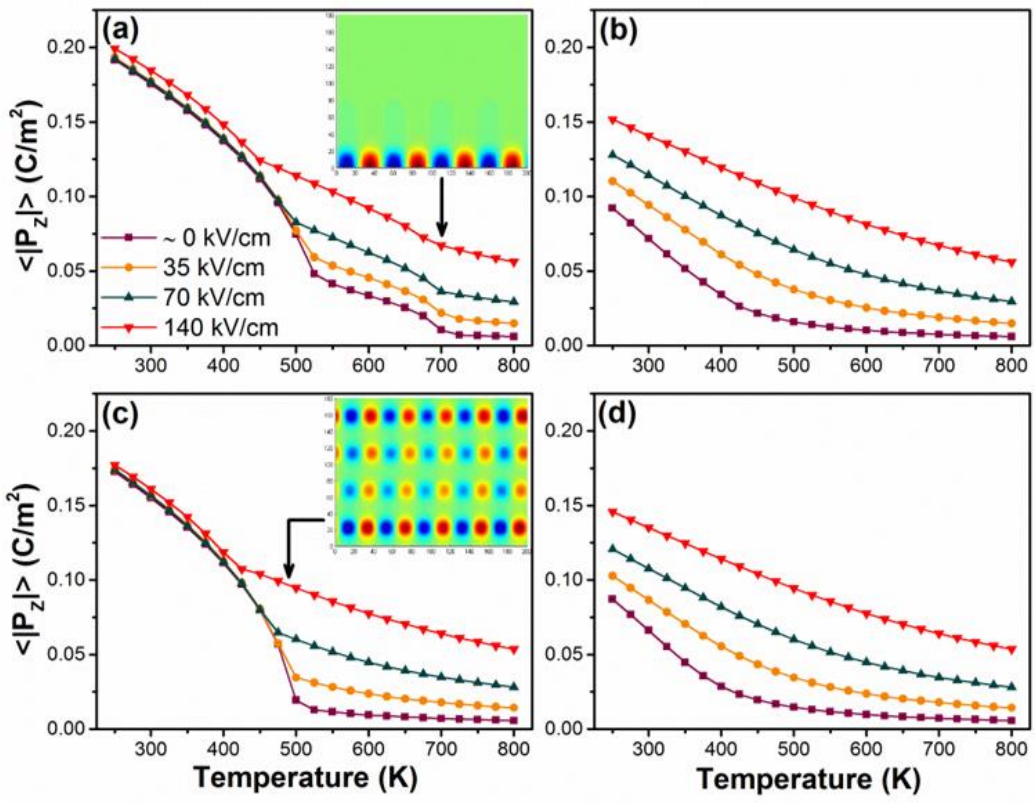

Figure 23. Field dependent average absolute out-of-plane plane polarizations of 72nm-thick epitaxial PZT/STO SLs on STO substrate as a function of temperature for a bilayer configuration with (a) 4 and (b) 8 repeating units. (c) and (d) show P_z of 4- and 8-unit symmetrical SLs, respectively. The insets in (a) and (c) are the position dependent polarization maps of the corresponding heterostructures near T_C (~700 K for bilayer and ~500 K for symmetrical). The maximum P_Z values on insets are 0.01 C/m^2.

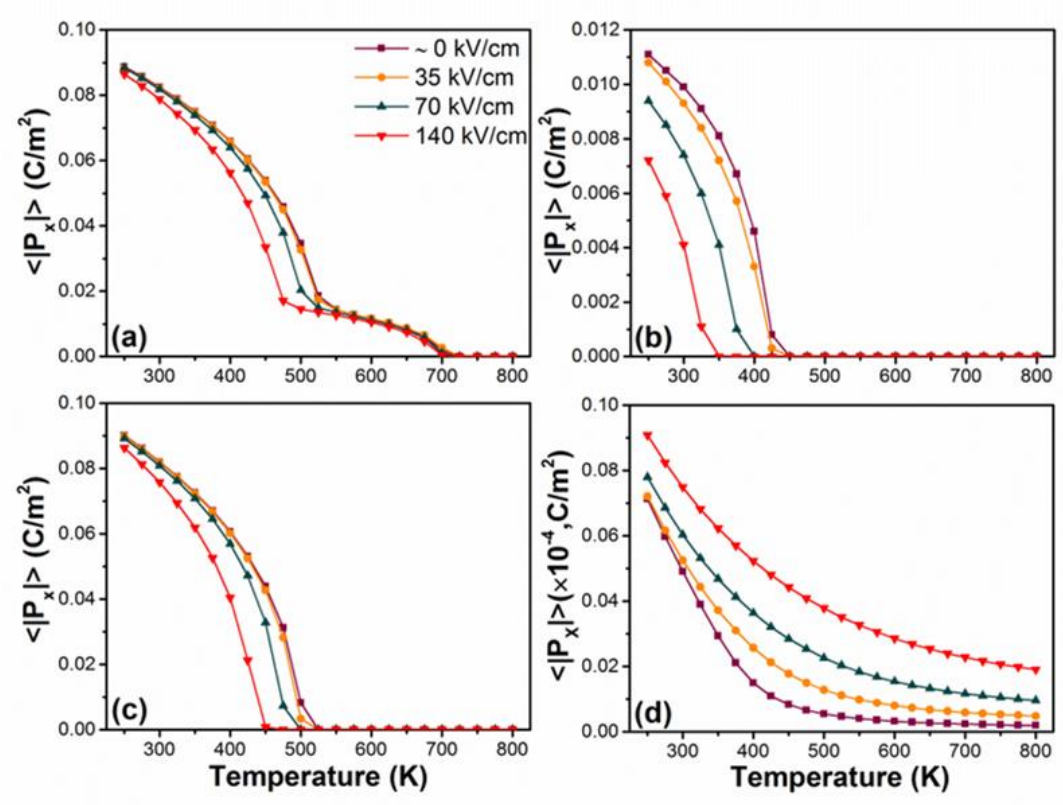

Figure 24. Field dependent average absolute in-plane polarizations of 72 nm-thick epitaxial PZT/STO SLs on STO substrate as a function of temperature for a bilayer configuration with (a) 4- and (b) 8 repeating units. (c) and (d) show P_x of 4 and 8-unit symmetrical SLs, respectively.

Pyroelectric coefficient of the 4 and 8-unit 72 nm-thick SLs is compared with that of a single domain (SD), monolayer PZT film at RT and 500K under various values of applied bias in Figure 25. The lack of interlayer interaction and the monodomain state of single layer PZT makes the pyroresponse insensitive to applied bias. Examining Figure 25(a), the RT response of the monolayer PZT is better than the 4-unit SLs overall but the 8-unit SL structures have an enhanced and significantly tunable pyroelectric response when the bias is not too high (<70 kV/cm). For instance, small bias pyroelectric coefficient of 8-unit symmetrical SLs is ~55% higher than that of a zero bias PZT monolayer reaching 0.045 μC cm^{-2} K^{-1}. Figure 25(b) shows that tunability of the

4-unit and 8-unit structures tend to increase with bias but this time the monolayer PZT has a higher response at 500K. In general, regardless of the magnitude of the pyroresponse, the SLs appear to have better tunability than the monolayer film.

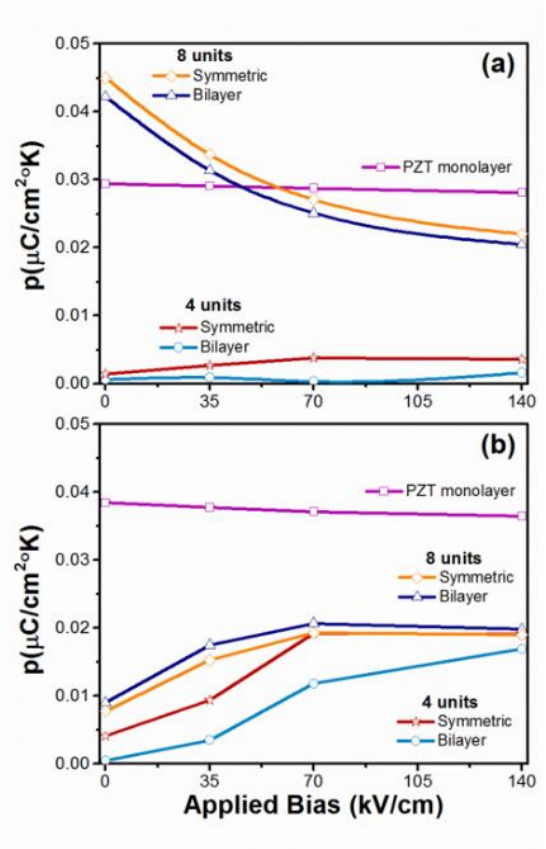

Figure 25. Field dependent average out-of-plane pyroelectric coefficients of 72 nm-thick epitaxial PZT/STO SLs on STO substrate at (a) room temperature (300K) and (b) 500K. Pyroresponse of a pseudomorphic, SD PZT monolayer on STO are also indicated in both figures for comparison.

Overall, the repeating unit thickness seems to have more substantial effect on the pyroelectric properties of PZT-STO superlattices than the unit periodicity. Moreover, the pyroelectric tunability of SLs are larger than that of a SD single layer PZT. Of course, a

multidomain SL without a bias would yield zero pyroresponse; however, one would still get half the pyroelectric coefficient of a single layer PZT by applying a moderate bias (70-140 kV cm^{-1}).

6.1.2 Dielectric Properties of PZT 30/70-STO Superlattices

In this section the phase transition characteristics and relative dielectric constant of 40 nm-thick epitaxial PZT-STO heterostructures with n=1, 2, and 4 is investigated. Similar to Section 6.1.1, the repeating unit symmetries are bilayer and symmetric. The transition temperatures (and the amplitude of polarization obtained in our study) in the system are reduced with increasing number of units (reduced layer thickness) for both bilayer and symmetrical units as shown in Figure 26 similar to what is shown in Figure 23. T_C for the symmetrical unit structures are lower than the bilayer structures since the FE layers are not in contact with the electrodes (See Ref.[265]). The transition starts from the FE in contact with one of the electrodes for the bilayer while it is homogeneous in the superlattice with symmetrical units for fixed total layer thickness. In fact, the transition is always homogeneous for superlattices consisting of symmetrical units regardless of thickness as theoretically demonstrated in Ref. [265]

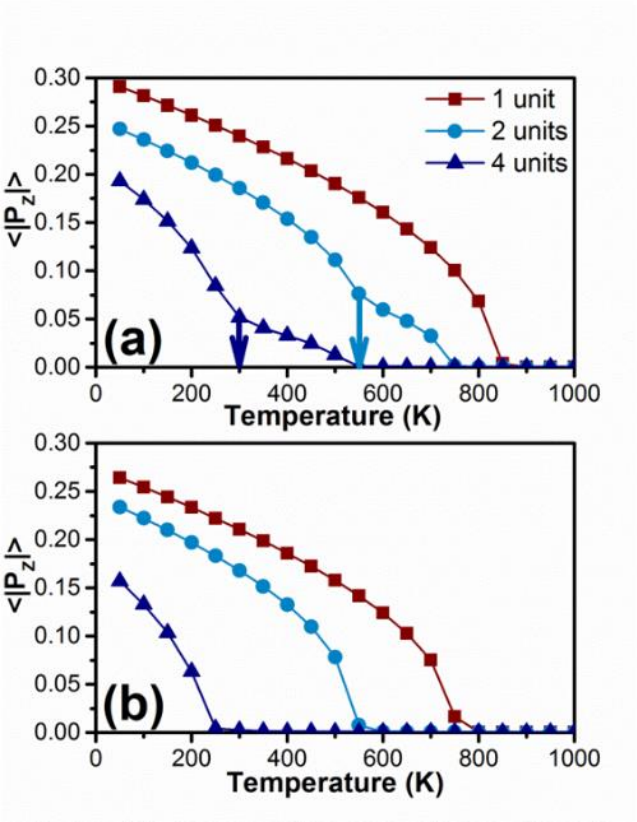

Figure 26. $<|P_z|>$ of 40 nm-thick PZT/STO heterostructures with *n*=1, 2, and 4 repeating unit(s) on STO for (a) bilayer and (b) symmetrical repeating unit systems.

The ε_R of STO-PZT heterostructures is shown in Figure 27. It is seen that the thick layers (1 unit and 2 unit ones) transforming into MD state at their respective T_C have no anomaly and the superlattices of both types (consisting of bilayers and symmetrical units) with 4 units have a reduced T_C, broad but finite dielectric curve with an anomaly-like behavior. This reveals the impact of interfaces on such structures along with reduced unit layer thickness. The peak observed in the superlattice consisting of 4 symmetrical units exactly corresponds to the transition [Compare Figures 26(b) and 27(b)]. For the 2 and 1 unit superlattices consisting of either symmetrical or bilayer units, domains are more stable against an applied field (compared to the 4 unit

superlattices), yielding no anomaly-like features at the transition into MD state but only a slope change at T_C is evident as shown here.

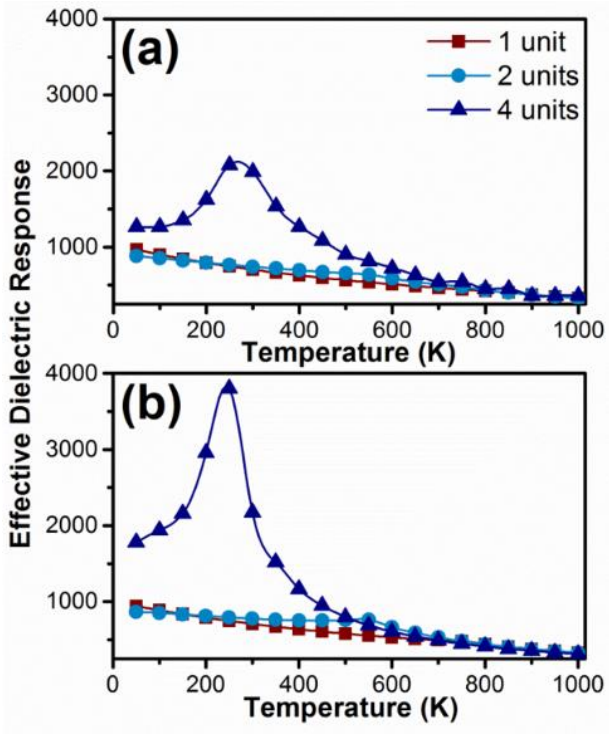

Figure 27. Temperature dependent ε_R of 40 nm-thick PZT/STO heterostructures on STO with n=1, 2, and 4 repeating unit(s) for (a) bilayer and (b) symmetrical systems.

Following the numerical data provided in Figure 26 from which the T_C can be found, we can compare our results to those obtainable from analytical theory reported in Ref.[265] that has yielded consistent results for the BTO/STO and KTO/KNO systems earlier.[265,300] Briefly, in that approach, the linear equation of state for a FE-PE superlattice with the FE layer in a uniaxial polar state is solved along with the appropriate equations of electrostatics in charge free media and we adapt the same method for our structures here. The comparative results are provided in Figure 28. Our simulation results here follow closely the curve obtained for PZT/STO bilayer and symmetrical unit derived from analytical theory wherein an approximate linear dielectric constant of STO was assumed. The deviation of our results from analytical theory is due to the fact that we

consider all polarization terms, and more importantly, the temperature dependent in-plane polarizability of both PZT and STO way reach high values leading to deviations from analytical theory.

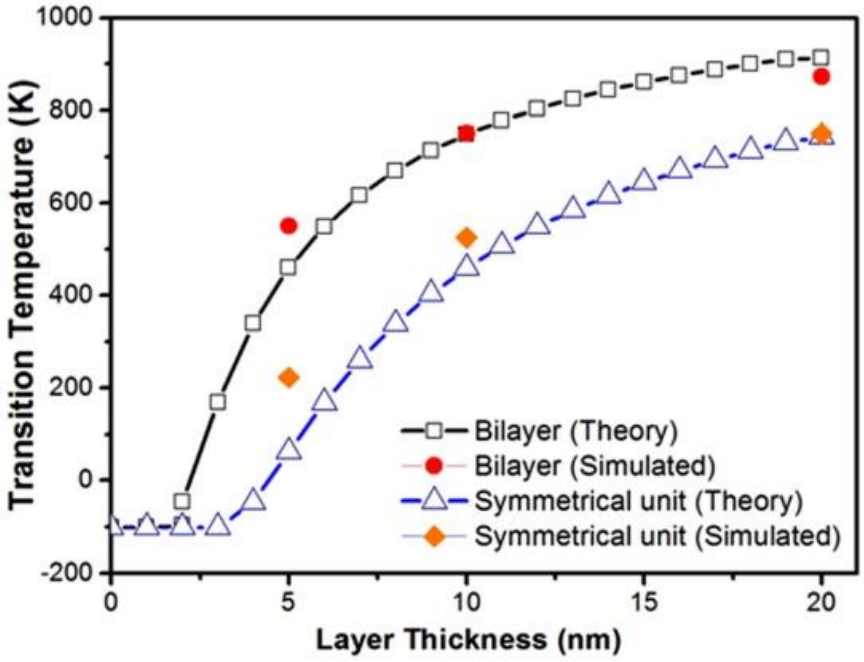

Figure 28. T_C of PZT/STO heterostructures on STO as a function of single layer thickness (h/2) in a repeating bilayer and symmetrical unit obtained numerically (simulated) and analytically (theory).

Chapter VII. Concluding Remarks

The dielectric, pyroelectric and electrocaloric properties of FE and FE-based multilayers are reported in this thesis. It is shown that by carefully designing multilayer structures, it is possible to obtain enhanced electrical properties from FE multilayers, even suppressing the performance of bulk/single layer FEs. This design features include but not limited to individual layer thickness and material, number of interfaces, total film thickness. For polycrystalline multilayers, thermal stresses that develop during cooling from the growth temperature intimately couples to the polarization in the heterostructure such that there exists a critical layer fraction of individual constituent layers for the enhanced electrical properties. This critical layer fraction is analogous to lambda-type transitions where at the critical point, second order properties such as pyroelectric coefficient and dielectric constant are enhanced. In addition to the aforementioned design features, one needs to consider repeating layer periodicity for a FE-based superlattice. It is shown that, depending on whether the repeating unit is in a symmetric or a bilayer configuration for a heteroepitaxial SL, the domain structure and the resulting dielectric and pyroelectric properties changes. The repeating unit thickness (number of units for a fixed total thickness) and periodicity determines how strongly each layer is (de)coupled together. It is found that, RT response of the monolayer PZT is better than the 4-unit PZT-STO SLs overall but the 8-unit SL structures have an enhanced and significantly tunable pyroelectric response when the bias is not too high (< 70 kV/cm). For example, small bias pyroelectric coefficient of 8-unit symmetrical SLs is ~55% higher than that of a zero bias PZT monolayer reaching 0.045 $\mu C\ cm^{-2}\ K^{-1}$. Moreover, since 4-unit SLs are in a multidomain state, there is no pyroresponse at zero bias overall.

APPENDIX

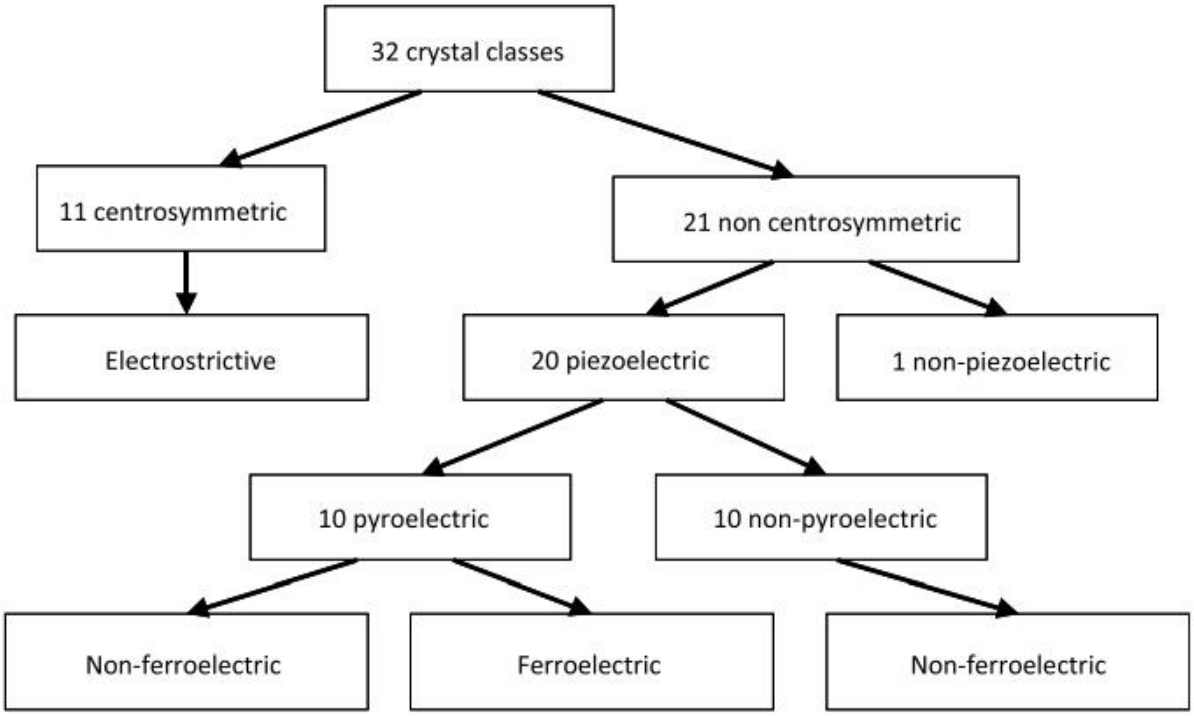

Figure 29. Categorizing crystal classes based on electrical properties.[306]

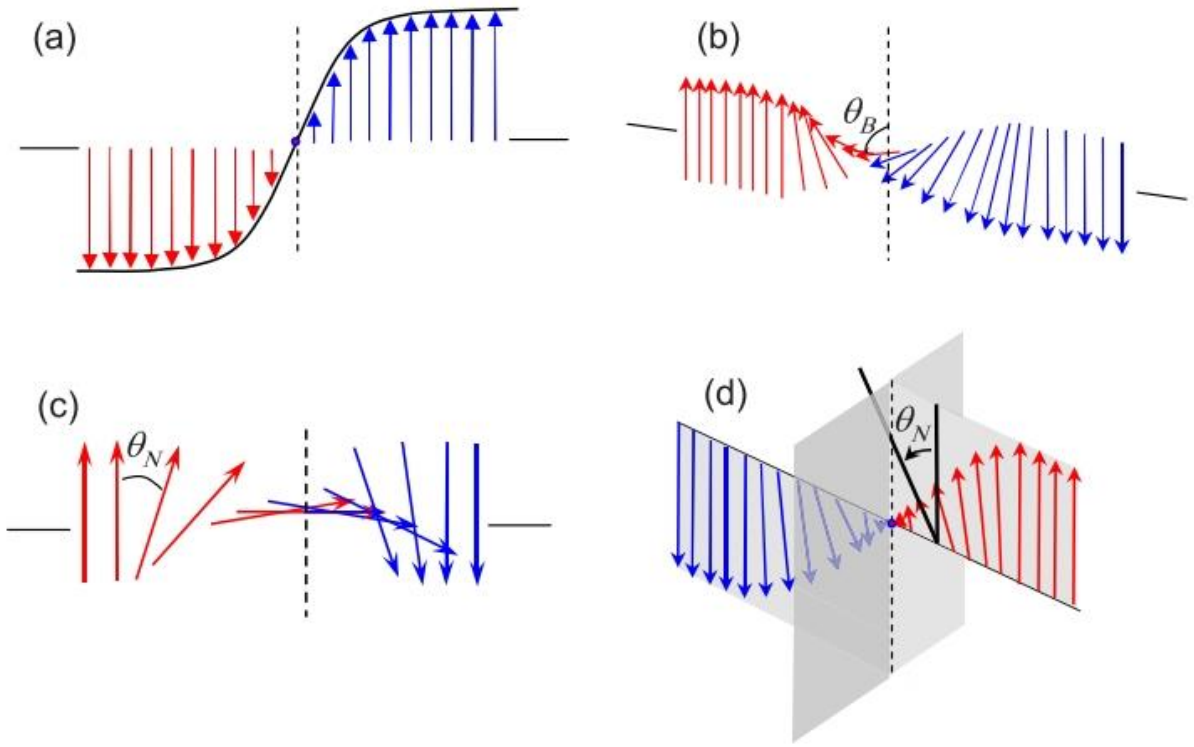

Figure 30. (a) Ising- (b) Bloch- (c) Néel- (d) mixed Ising-Bloch-type of walls in FEs. The angles represent in- and out-of-plane rotations of the polarization vector.[54]

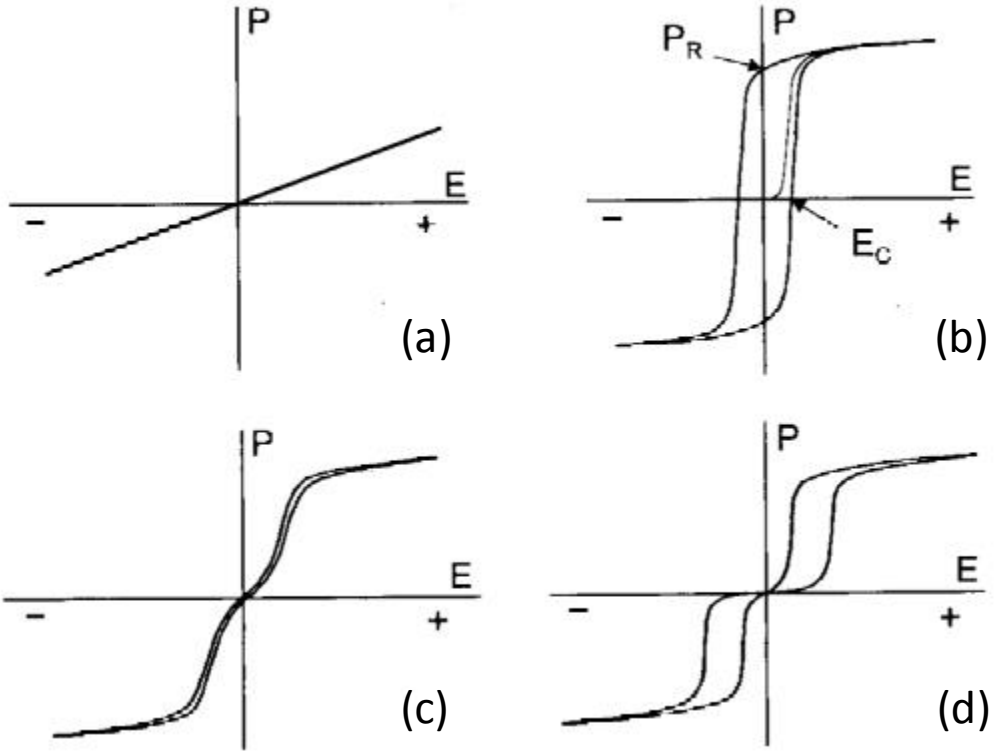

Figure 31. Hysteresis loops of some FE crystals. (a) a linear DE, (b) a FE (c) relaxor FE and (d) an AFE.

REFERENCES

[1] B. Fultz, *Phase Transitions in Materials* (2013).

[2] S.-K. Ma, *Modern Theory of Critical Phenomena* (2000).

[3] P. Papon, J. Leblond, and J.L. Meijer, *The Physics of Phase Transitions: Concepts and Applications*, Second (2006).

[4] B.A. Strukov and A.P. Levanyuk, *Ferroelectric Phenomena in Crystals* (1998).

[5] C. Domb and J.L. Lebowitz, *Phase Transitions and Critical Phenomena, Vol. 18*, First (2000).

[6] R.J. Braun, J.W. Cahn, G.B. McFadden, and A.A. Wheeler, Philos. Trans. R. Soc. A Math. Phys. Eng. Sci. **335**, 1337 (1997).

[7] K. Binder, Rep. Prog. Phys. **50**, 783 (1987).

[8] A.S. Sidorkin, *Domain Structure in Ferroelectrics and Related Materials* (CISP, 2006).

[9] S. Gevorgian, *Ferroelectrics in Microwave Devices Circuits and Systems: Physics, Modeling, Fabrication and Measurements* (Springer, 2009).

[10] M.E. Lines and A.M. Glass, *Principles and Applications of Ferroelectrics and Related Materials* (Clarendon Press, Oxford, 1977).

[11] K.M. Rabe, C.H. Ahn, and J.M. Triscone, *Physics of Ferroelectrics* (Springer-Verlag, Berlin, 2007).

[12] G. Subramanyam, M.W. Cole, N.X. Sun, T.S. Kalkur, N.M. Sbrockey, G.S. Tompa, X. Guo, C. Chen, S.P. Alpay, G.A. Rossetti, K. Dayal, L.-Q. Chen, and D.G. Schlom, J. Appl. Phys. **114**, 191301 (2013).

[13] M.J. Lancaster, J. Powell, and A. Porch, Supercond. Sci. Technol. **11**, 1323 (1998).

[14] A.K. Tagantsev, V.O. Sherman, K.F. Astafiev, J. Venkatesh, and N. Setter, J. Electroceram. **11**, 5 (2003).

[15] R.W. Whatmore, Rep. Prog. Phys. **49**, 1335 (1986).

[16] R.W. Whatmore, J. Electroceram. **13**, 139 (2004).

[17] M.M. Vopson, J. Phys. D. Appl. Phys. **46**, 345304 (2013).

[18] J.F. Scott, Annu. Rev. Mater. Res. **41**, 229 (2011).

[19] D.A. Tenne, A. Soukiassian, X.X. Xi, T.R. Taylor, P.J. Hansen, J.S. Speck, and R.A. York, Appl. Phys. Lett. **85**, 4124 (2004).

[20] N. Pertsev and H. Kohlstedt, Phys. Rev. Lett. **98**, 257603 (2007).

[21] G. Akcay, S.P. Alpay, G.A. Rossetti, and J.F. Scott, J. Appl. Phys. **103**, 24104 (2008).

[22] N. Balke, B. Winchester, W. Ren, Y.H. Chu, A.N. Morozovska, E.A. Eliseev, M. Huijben, R.K. Vasudevan, P. Maksymovych, J. Britson, S. Jesse, I. Kornev, R. Ramesh, L. Bellaiche, L.Q. Chen, and S. V. Kalinin, Nat. Phys. **8**, 81 (2011).

[23] H. Funakubo, M. Dekkers, A. Sambri, S. Gariglio, I. Shklyarevskiy, and G. Rijnders, MRS Bull. **37**, 1030 (2012).

[24] A. Rudiger, T. Schneller, A. Roelofs, S. Tiedke, T. Schmitz, and R. Waser, Appl. Phys. A **80**, 1247 (2005).

[25] M. Arredondo, M. Saunders, A. Petraru, H. Kohlstedt, I. Vrejoiu, M. Alexe, D. Hesse, N.D. Browning, P. Munroe, and V. Nagarajan, J. Mater. Sci. **44**, 5297 (2009).

[26] R.E. Newnham, *Properties of Materials: Anisotropy, Symmetry and Structure* (Oxford UP, 2005).

[27] G.H. Haertling, J. Am. Ceram. Soc. **82**, 797 (1999).

[28] N. Izyumskaya, Y.-I. Alivov, S.-J. Cho, H. Morkoç, H. Lee, and Y.-S. Kang, Crit. Rev. Solid State Mater. Sci. **32**, 111 (2007).

[29] D. Damjanovic, Rep. Prog. Phys. **61**, 1267 (1998).

[30] J. Fousek, J. Appl. Phys. **40**, 135 (1969).

[31] N. Nuraje and K. Su, Nanoscale **5**, 8752 (2013).

[32] C. Kittel, Phys. Rev. **82**, 729 (1951).

[33] L.E. Cross, J Phys. Soc. Jpn. **23**, 77 (1967).

[34] H. Liu and B. Dkhil, Zeitschrift Fur Krist. **226**, 163 (2011).

[35] E. Sawaguchi, G. Shirane, and Y. Takagi, J. Phys. Soc. Japan **6**, 333 (1951).

[36] K.M. Rabe, (2012).

[37] X. Hao, J. Zhai, L.B. Kong, and Z. Xu, Prog. Mater. Sci. **63**, 1 (2014).

[38] R.A. Cowley, S.N. Gvasaliya, S.G. Lushnikov, B. Roessli, and G.M. Rotaru, Adv. Phys. **60**, 229 (2011).

[39] A.A. Bokov and Z.-G. Ye, J. Mater. Sci. **41**, 31 (2006).

[40] Y. Yamashita, K. Harada, and S. Saitoh, Ferroelectrics **219**, 29 (1998).

[41] E. Sun and W. Cao, Prog. Mater. Sci. **65**, 124 (2014).

[42] Q. ZHANG, J. ZHAI, and L.B. KONG, J. Adv. Dielectr. **2**, 1230002 (2012).

[43] L.E. Cross and E. Pugh, Ferroelectr. Ferroebctrirs **76**, 241 (1987).

[44] J.H. Qiu, Solid State Commun. **150**, 1052 (2010).

[45] J. Karthik, J.C. Agar, A.R. Damodaran, and L.W. Martin, Phys. Rev. Lett. **109**, 257602 (2012).

[46] D.-J. Kim, J.-P. Maria, A.I. Kingon, and S.K. Streiffer, J. Appl. Phys. **93**, 5568 (2003).

[47] S. Trolier-McKinstry and P. Muralt, J. Electroceram. **12**, 7 (2004).

[48] G. Catalan, J. Seidel, R. Ramesh, and J.F. Scott, Rev. Mod. Phys. **84**, 119 (2012).

[49] P. Wurfel and I.P. Batra, Phys. Rev. B **8**, 5126 (1973).

[50] R.R. Mehta, B.D. Silverman, and J.T. Jacobs, J. Appl. Phys. **44**, 3379 (1973).

[51] M. Kohli, P. Muralt, and N. Setter, Appl. Phys. Lett. **72**, 3217 (1998).

[52] A. Roelofs, N.A. Pertsev, R. Waser, F. Schlaphof, L.M. Eng, C. Ganpule, V. Nagarajan, and R. Ramesh, Appl. Phys. Lett. **80**, 1424 (2002).

[53] A.S. Sidorkin, *Domain Structure in Ferroelectrics and Related Materials* (2006).

[54] D. Lee, R. Behera, P. Wu, H. Xu, Y. Li, S.B. Sinnott, S. Phillpot, L. Chen, and V. Gopalan, Phys. Rev. B **80**, 2 (2009).

[55] A.M. Bratkovsky and A.P. Levanyuk, Integr. Ferroelectr. **84**, 3 (2006).

[56] M. Dawber, K.M. Rabe, and J.F. Scott, Rev. Mod. Phys. **77**, 1083 (2005).

[57] C. Lichtensteiger, J.-M. Triscone, J. Junquera, and P. Ghosez, Phys. Rev. Lett. **94**, 47603 (2005).

[58] K. Lee and S. Baik, Annu. Rev. Mater. Res. **36**, 81 (2006).

[59] J.M. Gregg, Phys. Status Solidi A **206**, 577 (2009).

[60] T. Tsurumi, T. Hoshina, H. Takeda, Y. Mizuno, and H. Chazono, IEEE Trans. Ultrason. Ferroelectr. Freq. Control **56**, 1513 (2009).

[61] M.D. Glinchuk and A.N. Morozovskaya, Phys. Status Solidi **238**, 81 (2002).

[62] Z. Hong, A.R. Damodaran, F. Xue, S.-L. Hsu, J. Britson, A.K. Yadav, C.T. Nelson, J. Wang, J.F. Scott, L.W. Martin, R. Ramesh, and L.-Q. Chen, Nano Lett. **17**, (2017).

[63] A.K. Yadav, C.T. Nelson, S.L. Hsu, Z. Hong, J.D. Clarkson, C.M. Schlepütz, A.R. Damodaran, P. Shafer, E. Arenholz, L.R. Dedon, D. Chen, A. Vishwanath, A.M. Minor, L.Q. Chen, J.F. Scott, L.W. Martin, and R. Ramesh, Nature **530**, 198 (2016).

[64] R.G.P. McQuaid, L.J. McGilly, P. Sharma, A. Gruverman, and J.M. Gregg, Nat. Commun. **2**, 404 (2011).

[65] Y. Nahas, S. Prokhorenko, L. Louis, Z. Gui, I.A. Kornev, and L. Bellaiche, Nat. Commun. **6**, 8542 (2015).

[66] I. Naumov and A.M. Bratkovsky, Phys. Rev. Lett. **101**, 1 (2008).

[67] L.J. McGilly and J.M. Gregg, Nano Lett. **11**, 4490 (2011).

[68] L.W. Chang, V. Nagarajan, J.F. Scott, and J.M. Gregg, Nano Lett. **13**, 2553 (2013).

[69] J.M. Gregg, Ferroelectrics **433**, 74 (2012).

[70] B.J. Rodriguez, X.S. Gao, L.F. Liu, W. Lee, I.I. Naumov, A.M. Bratkovsky, D. Hesse, and M. Alexe, Nano Lett. **9**, 1127 (2009).

[71] A. Gruverman, D. Wu, H.-J. Fan, I. Vrejoiu, M. Alexe, R.J. Harrison, and J.F. Scott, J. Phys. Condens. Matter **342201**, 342201 (2008).

[72] Y.L. Tang, Y.L. Zhu, Z.J. Hong, E.A. Eliseev, A.N. Morozovska, Y.J. Wang, Y. Liu, Y.B. Xu, B. Wu, L.Q. Chen, S.J. Pennycook, and X.L. Ma, J. Mater. Res. **32**, 1 (2016).

[73] P. Aguado-Puente and J. Junquera, Phys. Rev. Lett. **100**, 1 (2008).

[74] R.G.P. McQuaid, A. Gruverman, J.F. Scott, and J.M. Gregg, Nano Lett. **14**, 4230 (2014).

[75] C. Coelho, C. Ferreira, and C.J. Ritsema, Science **348**, (2015).

[76] W.J. Chen, Y. Zheng, and B. Wang, Sci Rep **2**, (2012).

[77] C.T. Nelson, B. Winchester, Y. Zhang, S.J. Kim, A. Melville, C. Adamo, C.M. Folkman, S.H. Baek, C.B. Eom, D.G. Schlom, L.Q. Chen, and X. Pan, Nano Lett. **11**, 828 (2011).

[78] C.M. Wu, W.J. Chen, Y. Zheng, D.C. Ma, B. Wang, J.Y. Liu, and C.H. Woo, Sci Rep **4**, 3946 (2014).

[79] Z. Hong, A.R. Damodaran, F. Xue, S.-L. Hsu, J. Britson, A.K. Yadav, C.T. Nelson, J. Wang, J.F. Scott, L.W. Martin, R. Ramesh, and L.-Q. Chen, Nano Lett. acs. nanolett.6b04875 (2017).

[80] K. Uchino, E. Sadanaga, and T. Hirose, **90**, 1 (1989).

[81] K. Ishikawa, K. Yoshikawa, and N. Okada, Phys. Rev. B **37**, 5852 (1988).

[82] G. Arlt, D. Hennings, and G. de With, J. Appl. Phys. **58**, 1619 (1985).

[83] L. Mitoseriu, D. Ricinschi, C. Harnagea, M. Okuyama, T. Tsukamoto, and V. Tura, Jpn. J. Appl. Phys. **35**, 5210 (1996).

[84] S.B. Ren, C.J. Lu, J.S. Liu, H.M. Shen, and Y.N. Wang, Phys. Rev. B **54**, 337 (1996).

[85] H.Z. Jin and J. Zhu, J. Appl. Phys. **92**, 4594 (2002).

[86] M.H. Frey and D. a. Payne, Appl. Phys. Lett. **63**, 2753 (1993).

[87] Y. Luo, I. Szafraniak, V. Nagarajan, R.B. Wehrspohn, M. Steinhart, J.H. Wendorff, N.D. Zakharov, R. Ramesh, and M. Alexe, Integr. Ferroelectr. **59**, 1513 (2003).

[88] Z. Zhao, V. Buscaglia, M. Viviani, M.T. Buscaglia, L. Mitoseriu, A. Testino, M. Nygren, M. Johnsson, and P. Nanni, Phys. Rev. B - Condens. Matter Mater. Phys. **70**, 1 (2004).

[89] A. Rüdiger, T. Schneller, A. Roelofs, S. Tiedke, T. Schmitz, and R. Waser, Appl. Phys. A Mater. Sci. Process. **80**, 1247 (2005).

[90] L. Huang, Z. Chen, J.D. Wilson, S. Banerjee, R.D. Robinson, I.P. Herman, R. Laibowitz, and S. O'Brien, J. Appl. Phys. **100**, 34316 (2006).

[91] M.B. Smith, K. Page, T. Siegrist, P.L. Redmond, E.C. Walter, R. Seshadri, L.E. Brus, M.L. Steigerwald, S. Barbara, B. Laboratories, A. V Mountain, and M. Hill, 6955 (2008).

[92] D. Szwarcman, D. Vestler, and G. Markovich, ACS Nano **5**, 507 (2011).

[93] V.M. Fridkin, R. V Gaynutdinov, and S. Ducharme, Physics-Uspekhi **53**, 199 (2010).

[94] M. Frey and D. Payne, Phys. Rev. B. Condens. Matter **54**, 3158 (1996).

[95] W. Ma, M. Zhang, and Z. Lu, Phys. Status Solidi **166**, 811 (1998).

[96] M.H. Frey, Z. Xu, P. Han, and D. a. Payne, Ferroelectrics **206**, 337 (1998).

[97] J. Wang, Y. Li, L.-Q. Chen, and T.-Y. Zhang, Acta Mater. **53**, 2495 (2005).

[98] Y.Q. Chen, Y.F. En, Y. Huang, X.D. Kong, X.J. Zheng, and Y.D. Lu, Appl. Phys. Lett. **99**, 135 (2011).

[99] G.A. Samara, Phys. Rev. B **1**, 3777 (1970).

[100] W. Merz, Phys. Rev. **77**, 52 (1950).

[101] S.H. Oh and H.M. Jang, Appl. Phys. Lett. **72**, 1457 (1998).

[102] G. a. Rossetti, L.E. Cross, and K. Kushida, Appl. Phys. Lett. **59**, 2524 (1991).

[103] E.K. Akdogan and A. Safari, Jpn. J. Appl. Phys. **41**, 7170 (2002).

[104] E.K. Akdogan, C.J. Rawn, W.D. Porter, E.A. Payzant, and A. Safari, J. Appl. Phys. **97**, (2005).

[105] W. Ma, Appl. Phys. A **96**, 915 (2009).

[106] Y. Zheng, C.H. Woo, and B. Wang, J. Phys. Condens. Matter **20**, 135216 (2008).

[107] A. Morozovska, M. Glinchuk, and E. Eliseev, Phys. Rev. B **76**, 14102 (2007).

[108] B.A. Strukov and A.P. Levanyuk, *Ferroelectric Phenomena in Crystals: Physical Foundations* (Springer, 1998).

[109] J.M. Gregg, Phys. Status Solidi Appl. Mater. Sci. **206**, 577 (2009).

[110] D.D. Fong, G.B. Stephenson, S.K. Streiffer, J.A. Eastman, O. Auciello, P.H. Fuoss, and Thomps, Science **304**, 1650 (2004).

[111] N. Sai, A.M. Kolpak, and A.M. Rappe, Phys. Rev. B - Condens. Matter Mater. Phys. **72**, (2005).

[112] M.B. Okatan, J.V. Mantese, and S.P. Alpay, Acta Mater. **58**, 39 (2010).

[113] R.V.K. Mangalam, J.C. Agar, A.R. Damodaran, J. Karthik, and L.W. Martin, ACS Appl. Mater. Interfaces **5**, 13235 (2013).

[114] C.H. Woo and Y. Zheng, Appl. Phys. A **91**, 59 (2007).

[115] A.L. Roytburd, S. Zhong, and S.P. Alpay, Appl. Phys. Lett. **87**, 92902 (2005).

[116] P. Zubko, N. Stucki, C. Lichtensteiger, and J.M. Triscone, Phys. Rev. Lett. **104**, 187601 (2010).

[117] H. Khassaf, N. Khakpash, S. Vijayan, M. Aindow, and S.P. Alpay, Acta Mater. **105**, 68 (2016).

[118] Z. Wang and S. Oda, J. Electrochem. Soc. **147**, 4615 (2000).

[119] O. Nakagawara, T. Shimuta, T. Makino, S. Arai, H. Tabata, and T. Kawai, Appl. Phys. Lett. **77**, 3257 (2000).

[120] T. Choi and J. Lee, Ferroelectrics **328**, 41 (2005).

[121] T. Tsurumi, T. Harigai, D. Tanaka, H. Kakemoto, and S. Wada, Sci. Technol. Adv. Mater. **5**, 425 (2004).

[122] H. Tabata, H. Tanaka, and T. Kawai, Appl. Phys. Lett. **65**, 1970 (1994).

[123] A. Soukiassian, W. Tian, V. Vaithyanathan, J.H. Haeni, L.Q. Chen, X.X. Xi, D.G. Schlom, D.A. Tenne, H.P. Sun, X.Q. Pan, K.J. Choi, C.B. Eom, Y.L. Li, Q.X. Jia, C. Constantin, R.M. Feenstra, M. Bernhagen, P. Reiche, and R. Uecker, J. Mater. Res. **23**, 1417 (2008).

[124] M.H. Corbett, R.M. Bowman, J.M. Gregg, and D.T. Foord, Appl. Phys. Lett. **79**, 815 (2001).

[125] D. O'Neill, R.M. Bowman, and J.M. Gregg, J. Mater. Sci. Mater. Electron. **11**, 537 (2000).

[126] H. Christen, E. Specht, S. Silliman, and K. Harshavardhan, Phys. Rev. B **68**, 20101 (2003).

[127] T. Harigai, S.-M. Nam, H. Kakemoto, S. Wada, K. Saito, and T. Tsurumi, Thin Solid Films **509**, 13 (2006).

[128] H.-M. Christen, L.A. Knauss, and K.S. Harshavardhan, Mater. Sci. Eng. B **56**, 200 (1998).

[129] B. He and Z. Wang, ACS Appl. Mater. Interfaces **8**, 6736 (2016).

[130] J.B. Neaton and K.M. Rabe, Appl. Phys. Lett. **82**, 1586 (2003).

[131] V.A. Stephanovich, I.A. Luk'yanchuk, and M.G. Karkut, Phys. Rev. Lett. **94**, 47601 (2005).

[132] P. Zubko, N. Jecklin, A. Torres-Pardo, P. Aguado-Puente, A. Gloter, C. Lichtensteiger, J. Junquera, O. Stéphan, and J.-M. Triscone, Nano Lett. **12**, 2846 (2012).

[133] Y.L. Li, S.Y. Hu, D. Tenne, A. Soukiassian, D.G. Schlom, L.Q. Chen, X.X. Xi, K.J. Choi, C.B. Eom, A. Saxena, T. Lookman, and Q.X. Jia, Appl. Phys. Lett. **91**, 252904 (2007).

[134] X. Wu, M. Stengel, K.M. Rabe, and D. Vanderbilt, Phys. Rev. Lett. **101**, 87601 (2008).

[135] L. Kim, J. Kim, Y.S. Kim, D. Jung, N. Park, and J. Lee, Integr. Ferroelectr. **50**, 219 (2002).

[136] K. Johnston, X. Huang, J.B. Neaton, and K.M. Rabe, Phys. Rev. B - Condens. Matter Mater. Phys. **71**, 100103 (2005).

[137] M. Dawber, N. Stucki, C. Lichtensteiger, S. Ganglio, P. Ghosez, and J.M. Triscone, Adv. Mater. **19**, 4153 (2007).

[138] H.-M. Christen, E.D. Specht, D.P. Norton, M.F. Chisholm, and L.A. Boatner, Appl. Phys. Lett. **72**, 2535 (1998).

[139] P. Sharma, S. Ryu, J.D. Burton, T.R. Paudel, C.W. Bark, Z. Huang, Ariando, E.Y. Tsymbal,

G. Catalan, C.B. Eom, and A. Gruverman, Nano Lett. **15**, (2015).

[140] G. Singh-Bhalla, C. Bell, J. Ravichandran, W. Siemons, Y. Hikita, S. Salahuddin, A.F. Hebard, H.Y. Hwang, and R. Ramesh, Nat. Phys. **7**, 80 (2010).

[141] S. Parkin, X. Jiang, C. Kaiser, A. Panchula, K. Roche, and M. Samant, Proc. IEEE **91**, 661 (2003).

[142] S.D. Ha and S. Ramanathan, J. Appl. Phys. **110**, 71101 (2011).

[143] A.Q. Jiang, C. Wang, K.J. Jin, X.B. Liu, J.F. Scott, C.S. Hwang, T.A. Tang, H. Bin Lu, and G.Z. Yang, Adv. Mater. **23**, 1277 (2011).

[144] G.L. Yuan and J. Wang, Appl. Phys. Lett. **95**, (2009).

[145] D. Lee, S.H. Baek, T.H. Kim, J.G. Yoon, C.M. Folkman, C.B. Eom, and T.W. Noh, Phys. Rev. B - Condens. Matter Mater. Phys. **84**, 1 (2011).

[146] V.M. Voora, T. Hofmann, M. Schubert, M. Brandt, M. Lorenz, M. Grundmann, N. Ashkenov, and M. Schubert, Appl. Phys. Lett. **94**, 2009 (2009).

[147] J. Wu, X. Lou, Y. Wang, and J. Wang, Electrochem. Solid-State Lett. **13**, G9 (2010).

[148] H. Kohlstedt, N. Pertsev, J. Rodríguez Contreras, and R. Waser, Phys. Rev. B **72**, 125341 (2005).

[149] H. Lu, A. Lipatov, S. Ryu, D.J. Kim, H. Lee, M.Y. Zhuravlev, C.B. Eom, E.Y. Tsymbal, A. Sinitskii, and A. Gruverman, Nature **5**, 1 (2014).

[150] I.B. Misirlioglu and K. Sendur, IEEE Trans. Electron Devices **63**, 2374 (2016).

[151] E.Y. Tsymbal and A. Gruverman, Nat. Mater. **12**, 602 (2013).

[152] A. Gruverman, D. Wu, H. Lu, Y. Wang, H.W. Jang, C.M. Folkman, M.Y. Zhuravlev, D. Felker, M. Rzchowski, C.-B. Eom, and E.Y. Tsymbal, Nano Lett. **9**, 3539 (2009).

[153] V. Garcia, S. Fusil, K. Bouzehouane, S. Enouz-Vedrenne, N.D. Mathur, A. Barthélémy, and M. Bibes, Nature **460**, 81 (2009).

[154] P. Maksymovych, S. Jesse, P. Yu, R. Ramesh, A.P. Baddorf, and S. V. Kalinin, Science **324**, 1421 (2009).

[155] Z. Wen, C. Li, D. Wu, A. Li, and N. Ming, Nat. Mater. **12**, 617 (2013).

[156] L. Jiang, W.S. Choi, H. Jeen, S. Dong, Y. Kim, M.G. Han, Y. Zhu, S. V. Kalinin, E. Dagotto, T. Egami, and H.N. Lee, Nano Lett. **13**, 5837 (2013).

[157] S. Mathews, R. Ramesh, T. Venkatesan, and J. Benedetto, Science **276**, 238 (1997).

[158] T.P. Ma and J. Han, IEEE Electron Device Lett. **23**, 386 (2002).

[159] J. Hoffman, X. Pan, J.W. Reiner, F.J. Walker, J.P. Han, C.H. Ahn, and T.P. Ma, Adv. Mater. **22**, 2957 (2010).

[160] Y. Kaneko, Y. Nishitani, H. Tanaka, M. Ueda, Y. Kato, E. Tokumitsu, and E. Fujii, J. Appl.

Phys. **110**, (2011).

[161] H. Ishiwara, Curr. Appl. Phys. **9**, S2 (2009).

[162] G.A. Salvatore, L. Lattanzio, D. Bouvet, and A.M. Ionescu, IEEE Trans. Electron Devices **58**, 3162 (2011).

[163] G.A. Salvatore, L. Lattanzio, D. Bouvet, I. Stolichnov, N. Setter, and A.M. Ionescu, Appl. Phys. Lett. **97**, 53503 (2010).

[164] Y.C. Kong, F.S. Xue, J.J. Zhou, L. Li, C. Chen, and Y.R. Li, Appl. Phys. A **95**, 703 (2009).

[165] I.B. Misirlioglu, M. Yildiz, and K. Sendur, Sci. Rep. **5**, 14740 (2015).

[166] I.B. Misirlioglu, C. Sen, M.T. Kesim, and S.P. Alpay, J. Mater. Sci. **51**, 487 (2015).

[167] R. Meyer and R. Waser, J. Appl. Phys. **100**, 1 (2006).

[168] L.Q. Chen, J. Am. Ceram. Soc. **91**, 1835 (2008).

[169] J. Wang, S.Q. Shi, L.Q. Chen, Y. Li, and T.Y. Zhang, Acta Mater. **52**, 749 (2004).

[170] R.E. Cohen, J. Phys. Chem. Solids **61**, 139 (2000).

[171] W. Cochran, Adv. Phys **9**, 387 (1960).

[172] W. Cao, Ferroelectrics **375**, 28 (2008).

[173] L.D. Landau, Zh. Eks. Teor. Fiz. **7**, 19 (1937).

[174] A.F. Devonshire, Philos. Mag. **40**, 1040 (1949).

[175] A.F. Devonshire, Philos. Mag. **42**, 1065 (1951).

[176] Y. Liu, X. Lou, M. Bibes, and B. Dkhil, Phys. Rev. B - Condens. Matter Mater. Phys. **88**, 1 (2013).

[177] Y. Wang, M.K. Niranjan, K. Janicka, J.P. Velev, M.Y. Zhuravlev, S.S. Jaswal, and E.Y. Tsymbal, Phys. Rev. B - Condens. Matter Mater. Phys. **82**, 94114 (2010).

[178] M.Y. Gureev, A.K. Tagantsev, and N. Setter, **184104**, 1 (2011).

[179] A.M. Bratkovsky and A.P. Levanyuk, J. Comput. Theor. Nanos. **6**, 465 (2009).

[180] D. Damjanovic, Reports Prog. Phys. **61**, 1267 (1998).

[181] N.A. Pertsev, A.G. Zembilgotov, and A.K. Tagantsev, Phys. Rev. Lett. **80**, 1988 (1998).

[182] N.A. Pertsev, A.G. Zembilgotov, S. Hoffmann, R. Waser, and A.K. Tagantsev, J. Appl. Phys. **85**, 1698 (1999).

[183] J. Zhang, M.W. Cole, and S.P. Alpay, J. Appl. Phys. **108**, 54103 (2010).

[184] J. Zhang, A.A. Heitmann, S.P. Alpay, and G.A. Rossetti, J. Mater. Sci. **44**, 5263 (2009).

[185] M.T. Kesim, J. Zhang, S. Trolier-McKinstry, J. V. Mantese, R.W. Whatmore, and S.P. Alpay, J. Appl. Phys. **114**, 204101 (2013).

[186] A. Sharma, Z.G. Ban, S.P. Alpay, and J. V. Mantese, J. Appl. Phys. **95**, 3618 (2004).

[187] M.J. Haun, E. Furman, H.A. McKinstry, and L.E. Cross, Ferroelectrics **99**, 27 (1989).

[188] T. Ohno, H. Suzuki, D. Fu, M. Takahashi, T. Ota, and K. Ishikawa, Ceram. Int. **30**, 1487 (2004).

[189] R.S. Batzer, B.M. Yen, D. Liu, H. Chen, H. Kubo, and G.R. Bai, J. Appl. Phys. **80**, 6235 (1996).

[190] J. Zhang, C. V. Weiss, and S.P. Alpay, Appl. Phys. Lett. **99**, 42902 (2011).

[191] Y. He, Thermochim. Acta **419**, 135 (2004).

[192] Y. Okada and Y. Tokumaru, J. Appl. Phys. **56**, 314 (1984).

[193] R.G. Munro, J. Am. Ceram. Soc. **80**, 1919 (1997).

[194] R.W. Whatmore, Rep. Prog. Phys. **49**, 1335 (1986).

[195] P. Muralt, Rep. Prog. Phys. **64**, 1339 (2001).

[196] C.H. Tsai, Y.W. Bai, C.A. Chu, C.Y. Chung, and M.B. Lin, IEEE T. Consum. Electr. **57**, 1157 (2011).

[197] R.W. Whatmore, Ferroelectrics **118**, 241 (1991).

[198] S.P. Alpay, I.B. Misirlioglu, A. Sharma, and Z.G. Ban, J. Appl. Phys. **95**, 8118 (2004).

[199] D.G. Schlom, L.Q. Chen, C.B. Eom, K.M. Rabe, K.S. Streiffer, and J.M. Triscone, Annu. Rev. Mater. Res. **37**, 589 (2007).

[200] M.B. Okatan and S.P. Alpay, Appl. Phys. Lett. **95**, 92902 (2009).

[201] I.B. Misirlioglu, S.P. Alpay, M. Aindow, and V. Nagarajan, Appl. Phys. Lett. **88**, 102906 (2006).

[202] Q. Zhang and R.W. Whatmore, J. Appl. Phys. **94**, 5228 (2003).

[203] N.M. Shorrocks, A. Patel, M.J. Walker, and A.D. Parsons, Microelectron. Eng. **29**, 59 (1995).

[204] Z.G. Ban and S.P. Alpay, Appl. Phys. Lett. **82**, 3499 (2003).

[205] M.A. Todd, P.A. Manning, P.P. Donohue, A.G. Brown, and R. Watton, in *Proc. SPIE 4130, Infrared Technol. Appl. XXVI*, edited by B.F. Andersen, G.F. Fulop, and M. Strojnik (San Diego, 2000), pp. 128–139.

[206] M.H. Lee, R. Guo, and A.S. Bhalla, J. Electroceram. **2**, 229 (1998).

[207] N. Setter and R. Waser, Acta Mater. **48**, 151 (2000).

[208] R.W. Whatmore, P. Kirby, A. Patel, N.M. Shorrocks, T. Bland, and M. Walker, *Science and Technology of Electroceramic Thin Films* (Kluwer Academic Publishers, 1995).

[209] M. Kohli, A. Seifert, and P. Muralt, Integr. Ferroelectr. **22**, 453 (1998).

[210] R. Kohler, G. Suchaneck, P. Padmini, T. Sandner, G. Gerlach, and G. Hofmann,

Ferroelectrics **225**, 57 (1999).

[211] R. Kohler, P. Padmini, G. Gerlach, G. Hofmann, and R. Bruchhaus, Integr. Ferroelectr. **22**, 383 (1998).

[212] Q. Zhang and R.W. Whatmore, J. Phys. D Appl. Phys. **34**, 2296 (2001).

[213] Q. Tan, W. Zhang, C. Xue, J. Xiong, J. Liu, J. Li, and T. Liang, Microelectron. J. **40**, 58 (2009).

[214] W. Liu, J.S. Ko, and W. Zhu, Thin Solid Films **371**, 254 (2000).

[215] Y. Guo, D. Akai, K. Swada, and M. Ishida, Appl. Phys. Lett. **90**, 232908 (2007).

[216] J.S. Ko, W. Liu, W. Zhu, and B.M. Kwak, Solid State Electron. **46**, 1155 (2002).

[217] Z. Huang, Q. Zhang, and R.W. Whatmore, J. Appl. Phys. **85**, 7355 (1999).

[218] L.L. Sun, O.K. Tan, and W.G. Zhu, J. Appl. Phys. **99**, 94108 (2006).

[219] S. Corkovic and Q. Zhang, J. Appl. Phys. **105**, 61610 (2009).

[220] L.L. Sun, W.G. Liu, O.K. Tan, and W. Zhu, Mater. Sci. Eng. B **99**, 173 (2003).

[221] S.H. Kang, H.J. Lee, J.L. Kim, I.W. Kim, E.C. Park, J.S. Lee, and S.S. Yi, Ferroelectrics **328**, 47 (2005).

[222] G. Gerlach, G. Suchaneck, R. Kohler, T. Sandner, P. Padmini, R. Krawietz, W. Pompe, J. Frey, O. Jost, and A. Schonecker, Ferroelectrics **230**, 109 (1999).

[223] M.T. Kesim, J. Zhang, J. V Mantese, R.W. Whatmore, and S.P. Alpay, **204101**, 1 (2013).

[224] P.E. Janolin, J. Mater. Sci. **44**, 5025 (2009).

[225] M.B. Kelman, P.C. McIntyre, B.C. Hendrix, S.M. Bilodeau, and J.F. Roeder, J. Appl. Phys. **93**, 9231 (2003).

[226] N. Setter, D. Damjanovic, L. Eng, G. Fox, S. Gevorgian, S. Hong, A. Kingon, H. Kohlstedt, N.Y. Park, G.B. Stephenson, I. Stolitchnov, A.K. Taganstev, D. V. Taylor, T. Yamada, and S. Streiffer, J. Appl. Phys. **100**, 51606 (2006).

[227] R.J. Ong, D.A. Payne, and N.R. Sottos, J. Am. Ceram. Soc. **88**, 2839 (2005).

[228] H.-X. Cao, V.C. Lo, and Z.-Y. Li, J. Appl. Phys. **101**, 14113 (2007).

[229] Y. Zheng, B. Wang, and C.H. Woo, Appl. Phys. Lett. **89**, 62904 (2006).

[230] H.X. Cao, V.C. Lo, and W.W.Y. Chung, J. Appl. Phys. **99**, 24103 (2006).

[231] F. Jin, G.W. Auner, R. Naik, N.W. Schubring, J. V. Mantese, A.B. Catalan, and A.L. Micheli, Appl. Phys. Lett. **73**, 2838 (1998).

[232] N.W. Schubring, J. V Mantese, A.L. Micheli, A.B. Catalan, and R.J. Lopez, Phys. Rev. Lett. **68**, 1778 (1992).

[233] Y. Ivry, V. Lyahovitskaya, I. Zon, I. Lubomirsky, E. Wachtel, and A.L. Roytburd, Appl.

Phys. Lett. **90**, 172905 (2007).

[234] G.L. Brennecka, W. Huebner, B.A. Tuttle, and P.G. Clem, J. Am. Ceram. Soc. **87**, 1459 (2004).

[235] S. Utsugi, T. Fujisawa, Y. Ehara, T. Yamada, M. Matsushima, H. Morioka, and H. Funakubo, Appl. Phys. Lett. **96**, 102905 (2010).

[236] S. Trolier-Mckinstry, J.F. Shepard Jr, J.L. Lacey, T. Su, G. Zavala, and J. Fendler, Ferroelectrics **206**, 381 (1998).

[237] J.F. Shepard, S. Trolier-McKinstry, M. Hendrickson, and R. Zeto, in *Mater. Smart Syst. II Vol. 459 Mater. Res. Soc. Symp. Proc.*, edited by E.P. George, R. Gotthardt, K. Otsuka, S. Trolier-McKinstry, and M. WunFogle (Materials Research Society, Boston, 1997), pp. 47–51.

[238] Q.Y. Qiu, S.P. Alpay, and V. Nagarajan, J. Appl. Phys. **107**, 114105 (2010).

[239] G. Akcay, I.B. Misirlioglu, and S.P. Alpay, J. Appl. Phys. **101**, 104110 (2007).

[240] Q.Y. Qiu, V. Nagarajan, and S. Alpay, Phys. Rev. B **78**, 64117 (2008).

[241] N.A. Pertsev and V.G. Koukhar, Phys. Rev. B **16**, 3722 (2000).

[242] S.P. Alpay and A.L. Roytburd, J. Appl. Phys. **83**, 4714 (1998).

[243] J. Ricote, D. Chateigner, L. Pardo, M. Alguero, J. Mendiola, and M.L. Calzada, Ferroelectrics **241**, 167 (2000).

[244] R. Bruchhaus, D. Pitzer, R. Primig, M. Schreiter, W. Wersing, N. Neumann, N. Hess, J. Vollheim, R. Kohler, and M. Simon, Integr. Ferroelectr. **17**, 369 (1997).

[245] P. Muralt, IEEE T. Ultrason. Ferr. **47**, 903 (2000).

[246] D. Ambika, V. Kumar, K. Tomioka, and I. Kanno, Adv. Mat. Lett. **3**, 102 (2012).

[247] Q. Du, J. Li, W. Nothwang, and M.W. Cole, Acta Mater. **54**, 2577 (2006).

[248] A.G. Zembilgotov, N.A. Pertsev, U. Böttger, and R. Waser, Appl. Phys. Lett. **86**, 52903 (2005).

[249] A. Roy, A. Dhar, D. Bhattacharya, and S.K. Ray, J. Phys. D. Appl. Phys. **41**, 95408 (2008).

[250] V. Reymond, D. Michau, S. Payan, and M. Maglione, Ceram. Int. **30**, 1085 (2004).

[251] C.L. Sun, S.Y. Chen, M.Y. Yang, and A. Chin, J. Electrochem. Soc. **148**, F203 (2001).

[252] K.-J. Choi, W.-C. Shin, J.-H. Yang, and S.-G. Yoon, Appl. Phys. Lett. **75**, 722 (1999).

[253] M.W. Cole, E. Ngo, C. Hubbard, S.G. Hirsch, M. Ivill, W.L. Sarney, J. Zhang, and S.P. Alpay, J. Appl. Phys. **114**, 164107 (2013).

[254] S.S. Ahmed, J.P. Denton, and G.W. Neudeck, J. Vac. Sci. Technol. B **19**, 800 (2001).

[255] Y. Espinal, M.T. Kesim, I.B. Misirlioglu, S. Trolier-McKinstry, J. V. Mantese, and S.P. Alpay, Appl. Phys. Lett. **105**, 1 (2014).

[256] R.W. Whatmore, P.C. Osbond, and N.M. Shorrocks, Ferroelectrics **76**, 351 (1987).

[257] G. Sebald, E. Lefeuvre, and D. Guyomar, IEEE Trans. Ultrason. Ferroelectr. Freq. Control **55**, 538 (2008).

[258] N. Izyumskaya, Y.-I. Alivov, S.-J. Cho, H. Morkoç, H. Lee, and Y.-S. Kang, Crit. Rev. Solid State Mater. Sci. **32**, 111 (2007).

[259] M.H. Corbett, R.M. Bowman, J.M. Gregg, and D.T. Foord, Appl. Phys. Lett. **79**, 815 (2001).

[260] M. Dawber, N. Stucki, C. Lichtensteiger, S. Gariglio, P. Ghosez, and J.M. Triscone, Adv. Mater. **19**, 4153 (2007).

[261] M.T. Kesim, J. Zhang, S.P. Alpay, and L.W. Martin, Appl. Phys. Lett. **105**, (2014).

[262] T.R. Taylor, P.J. Hansen, B. Acikel, N. Pervez, R.A. York, S.K. Streiffer, and J.S. Speck, Appl. Phys. Lett. **80**, 1978 (2002).

[263] M.T. Kesim, M.W. Cole, J. Zhang, I.B. Misirlioglu, and S.P. Alpay, Appl. Phys. Lett. **104**, 22901 (2014).

[264] S. Song, J. Zhai, L. Gao, and X. Yao, Appl. Phys. Lett. **94**, 52902 (2009).

[265] A.P. Levanyuk and I.B. Misirlioglu, J. Appl. Phys. **110**, 114109 (2011).

[266] L. Davis and L.G. Rubin, J. Appl. Phys. **24**, 1194 (1953).

[267] J. Bellotti, E.K. Akdogan, A. Safari, W. Chang, and S. Kirchoefer, Integr. Ferroelectr. **49**, 113 (2002).

[268] Z. Yuan, Y. Lin, J. Weaver, X. Chen, C.L. Chen, G. Subramanyam, J.C. Jiang, and E.I. Meletis, Appl. Phys. Lett. **87**, 152901 (2005).

[269] N.K. Pervez, P.J. Hansen, and R.A. York, Appl. Phys. Lett. **85**, 4451 (2004).

[270] F.A. Miranda, F.W. Van Keuls, R.R. Romanofsky, C.H. Mueller, S. Alterovitz, and G. Subramanyam, Integr. Ferroelectr. **42**, 131 (2002).

[271] N.A. Pertsev, A.K. Tagantsev, and N. Setter, Phys. Rev. B **61**, R825 (2000).

[272] R.J. Cava, J. Mater. Chem. **11**, 54 (2001).

[273] S.S. Gevorgian and E.L. Kollberg, IEEE T. Microw. Theory **49**, 2117 (2001).

[274] L.B. Kong, S. Li, T.S. Zhang, J.W. Zhai, F.Y.C. Boey, and J. Ma, Prog. Mater. Sci. **55**, 840 (2010).

[275] D. Dimos and C.H. Mueller, Annu. Rev. Mater. Sci. **28**, 397 (1998).

[276] H.N. Al-Shareef, D. Dimos, M. V. Raymond, and R.W. Schwartz, J. Electroceram. **1**, 145 (1997).

[277] M.B. Okatan, A.L. Roytburd, J. V. Mantese, and S.P. Alpay, J. Appl. Phys. **105**, 114106 (2009).

[278] N.A. Pertsev, P.E. Janolin, J.-M. Kiat, and Y. Uesu, Phys. Rev. B **81**, 144118 (2010).

[279] M.W. Cole, P.C. Joshi, M. Ervin, M. Wood, and R.L. Pfeffer, J. Appl. Phys. **92**, 3967 (2002).

[280] A. Erbil, Y. Kim, and R.A. Gerhardt, Phys. Rev. Lett. **77**, 1628 (1996).

[281] M.G. Harwood, P. Popper, and D.F. Rushman, Nature **160**, 58 (1947).

[282] M. Valant, Prog. Mater. Sci. **57**, 980 (2012).

[283] M. Ožbolt, A. Kitanovski, J. Tušek, and A. Poredoš, Int. J. Refrig. **40**, 174 (2014).

[284] K.A. Gschneidner and V.K. Pecharsky, Int. J. Refrig. **31**, 945 (2008).

[285] S.-G. Lu and Q. Zhang, Adv. Mater. **21**, 1983 (2009).

[286] M. Valant, A.-K. Axelsson, F. Le Goupil, and N.M. Alford, Mater. Chem. Phys. **136**, 277 (2012).

[287] B.A. Tuttle and D.A. Payne, Ferroelectrics **37**, 603 (1981).

[288] A. Mischenko, Q. Zhang, J.F. Scott, R.W. Whatmore, and N.D. Mathur, Science **311**, 1270 (2006).

[289] R. Chukka, J.W. Cheah, Z. Chen, P. Yang, S. Shannigrahi, J. Wang, and L. Chen, Appl. Phys. Lett. **98**, 242902 (2011).

[290] X. Hao, Z. Yue, J. Xu, S. An, and C.-W. Nan, J. Appl. Phys. **110**, 64109 (2011).

[291] S.G. Lu, B. Rožič, Q.M. Zhang, Z. Kutnjak, X. Li, E. Furman, L.J. Gorny, M. Lin, B. Malič, M. Kosec, R. Blinc, and R. Pirc, Appl. Phys. Lett. **97**, 162904 (2010).

[292] B. Li, J.B. Wang, X.L. Zhong, F. Wang, and Y.C. Zhou, J. Appl. Phys. **107**, 14109 (2010).

[293] J.H. Qiu and Q. Jiang, J. Appl. Phys. **103**, 84105 (2008).

[294] J. Zhang, A.A. Heitmann, S.P. Alpay, and G.A. Rossetti, J. Mater. Sci. **44**, 5263 (2009).

[295] J. Karthik and L.W. Martin, Appl. Phys. Lett. **99**, 32904 (2011).

[296] A. Navid, D. Vanderpool, A. Bah, and L. Pilon, Int. J. Heat Mass Transf. **53**, 4060 (2010).

[297] A.P. Levanyuk and I.B. Misirlioglu, Appl. Phys. Lett. **103**, 192906 (2013).

[298] X. Wu, K.M. Rabe, and D. Vanderbilt, Phys. Rev. B - Condens. Matter Mater. Phys. **83**, 20104 (2011).

[299] D.A. Tenne, A. Bruchhausen, N.D. Lanzillotti-Kimura, A. Fainstein, R.S. Katiyar, A. Cantarero, A. Soukiassian, V. Vaithyanathan, J.H. Haeni, W. Tian, D.G. Schlom, K.J. Choi, D.M. Kim, C.B. Eom, H.P. Sun, X.Q. Pan, Y.L. Li, L.Q. Chen, Q.X. Jia, S.M. Nakhmanson, K.M. Rabe, and X.X. Xi, Science **313**, 1614 (2006).

[300] V.A. Stephanovich, I.A. Luk'yanchuk, and M.G. Karkut, Phys. Rev. Lett. **94**, 47601 (2005).

[301] E.D. Specht, H.-M. Christen, D.P. Norton, and L.A. Boatner, Phys. Rev. Lett. **80**, 4317 (1998).

[302] A. Soukiassian, W. Tian, V. Vaithyanathan, J.H. Haeni, L.Q. Chen, X.X. Xi, D.G. Schlom,

D.A. Tenne, H.P. Sun, X.Q. Pan, K.J. Choi, C.B. Eom, Y.L. Li, Q.X. Jia, C. Constantin, R.M. Feenstra, M. Bernhagen, P. Reiche, and R. Uecker, J. Mater. Res. **23**, 1417 (2008).

[303] Y.L. Li, S.Y. Hu, D. Tenne, A. Soukiassian, D.G. Schlom, L.Q. Chen, X.X. Xi, K.J. Choi, C.B. Eom, A. Saxena, T. Lookman, and Q.X. Jia, Appl. Phys. Lett. **91**, 3 (2007).

[304] I.B. Misirlioglu, A.L. Vasiliev, M. Aindow, S.P. Alpay, and R. Ramesh, Appl. Phys. Lett. **84**, 1742 (2004).

[305] S.P. Alpay, I.B. Misirlioglu, V. Nagarajan, and R. Ramesh, Appl. Phys. Lett. **85**, 2044 (2004).

[306] E. Defaÿ, *Integration of Ferroelectric and Piezoelectric Thin Films: Concepts and Applications for Microsystems* (2013).